POLYPUBLIE

Characterization of Specimens 3D Printed by Fused Filament Fabrication Using Advanced Thermoplastic Composites Developed for Aerospace Applications

Ferran Santonja Soto

Document en libre accès dans PolyPublie
Open Access document in PolyPublie

Date	2023
Type	Mémoire ou thèse / Dissertation or Thesis Mémoire de maîtrise/Master's thesis
URL de PolyPublie **PolyPublie URL**	https://publications.polymtl.ca/10850/
Conditions d'utilisation **Terms of use**	© Tous droits réservés / All rights reserved
Référence **Citation**	Santonja Soto, F. (2023). Characterization of Specimens 3D Printed by Fused Filament Fabrication Using Advanced Thermoplastic Composites Developed for Aerospace Applications [Mémoire de maîtrise, Polytechnique Montréal]. PolyPublie. https://publications.polymtl.ca/10850/

Détails de la thèse
Thesis details

Directeurs de recherche **Advisors**	Daniel Therriault, Martin Lévesque, & Mihaela Mihai
Programme **Program**	Génie aérospatial

Ce fichier a été téléchargé à partir de PolyPublie, le dépôt institutionnel de Polytechnique Montréal
This file has been downloaded from PolyPublie, the institutional repository of Polytechnique Montréal
https://publications.polymtl.ca

POLYTECHNIQUE MONTRÉAL
affiliée à l'Université de Montréal

Characterization of Specimens 3D Printed by Fused Filament Fabrication Using Advanced Thermoplastic Composites Developed for Aerospace Applications

FERRAN SANTONJA SOTO

Département de génie mécanique

Mémoire présenté en vue de l'obtention du diplôme de *Maîtrise ès sciences appliquées*

Génie aérospatial

Mars 2023

© Ferran Santonja Soto, 2023.

POLYTECHNIQUE MONTRÉAL
affiliée à l'Université de Montréal

Ce mémoire intitulé :

Characterization of Specimens 3D Printed by Fused Filament Fabrication Using Advanced Thermoplastic Composites Developed for Aerospace Applications

présenté par **Ferran SANTONJA SOTO**
en vue de l'obtention du diplôme de *Maîtrise ès sciences appliquées*
a été dûment accepté par le jury d'examen constitué de :

David VIDAL, président
Daniel THERRIAULT, membre et directeur de recherche
Martin LÉVESQUE, membre et codirecteur de recherche
Mihaela MIHAI, membre et codirectrice de recherche
Farbod KHAMENEIFAR, membre

ACKNOWLEDGEMENTS

I would first like to thank my research director Professor Daniel Therriault who not only has supported me financially during these years, but he has also been in direct contact with me to help me in my research in the best possible way. I also wanted to thank my co-directors Professor Martin Lévesque and Dr. Mihaela Mihai who also have helped me with their extensive knowledge of the subject as well as in the most stressful moments during my studies, such as the predoctoral exam. I also want to thank Dr. Rouhollah D. Farahani who has helped me with useful advice and support during my studies.

I am appreciative of the members of the Laboratory of Multiscale Mechanics (LM2) for their help in the research as well as their advices and support in the moments of blockage where one is a little lost with his research without knowing which way to go. Some of their names are Dogan Arslan, Yanik Landry, Paul Gregorio, Alessandra Lingua, Yahya Abderrafai, Jean François Chauvette, Juliette Pierre, Olivier Lampron, Facundo Sosa-Rey, Kambiz Chizari, Josue Costa, David Brzeski, Ana Maria Serbescu, and others who have shared this laboratory with me. I also would like to thank the magnificent team from National Research Council of Canada (NRC) led by Dr. Mihaela Mihai.

Of course, I would like to acknowledge the work, help and support of all the companies that are within the 3D Research Ecosystem for Additive Manufacturing (3DREAM).

Finally, I want to thank my family who have supported me in this research journey from the beginning. I wanted to thank my father and my mother for encouraging and supporting me in selecting my path and making my own decisions and my sister that although we have not seen each other much for years I am sure we will have the opportunity to share much more time together. Finally, I also wanted to thank all my friends in Spain and my new friends in Canada.

RÉSUMÉ

La fabrication additive, et en particulier la fabrication par filament fondu (FFF), est considérée comme une méthode courante de fabrication de pièces pour différentes applications. La variété de matériaux qu'offre la FFF rend cette technique très utile dans plusieurs domaines de l'industrie, comme par exemple le transport terrestre et aérien. Les polymères thermoplastiques performants à hautes températures de fusion, comme le polyétheréthercétone (PEEK) et le polyétherimide (PEI) offrent d'excellentes propriétés mécaniques et thermiques qui peuvent être améliorées davantage par l'ajout de renforts tels que des fibres de carbone pour créer des composites performants à hautes températures de fusion. Des matériaux commerciaux pour les applications à haute performance sont actuellement disponibles sur le marché, mais leur prix est considérablement élevé et les matériaux disponibles sont encore limités. Ce projet a utilisé une machine d'impression FFF en format ouvert avec une chambre thermique (AON-M2) pour imprimer des composites performants de hautes températures de fusion développés à base de PEI (nom commercial: ULTEM). Le PEI présente de meilleures propriétés mécaniques que les matériaux d'impression standard comme le polylactic acid (PLA) ou l'acrylonitrile butadiène styrène (ABS), mais les coûts des matériaux sont réduits de moitié par rapport au PEEK. Les matériaux développés par le Laboratoire de Mécanique Multi-échelles (LM2) et le Conseil National de Recherches du Canada (CNRC) ont été imprimés avec différents pourcentages de fibres de carbone et de noir de carbone thermique. Un renforcement maximal de 40 % en poids de fibres de carbone a été imprimé. Les propriétés mécaniques des échantillons imprimés avec des polymères thermoplastiques performants, de hautes températures de fusion commerciaux et avec les matériaux développés ont été évaluées en utilisant la norme d'essai de traction ASTM D638. Les valeurs maximales du module de rigidité et de la résistance ultime à la traction obtenues pour les échantillons imprimés en 3D avec les filaments développés renforcés étaient respectivement de 3,3 GPa et 47 MPa. En outre, les échantillons ont été analysés par microscopie électronique à balayage (MEB) et par microtomographie aux rayons X (micro-CT). Les images obtenues par MEB et micro-CT ont permis de comprendre la relation entre les propriétés mécaniques et les porosités à l'intérieur des échantillons, qui dans le cas des matériaux développés étaient de ∼16 %.

ABSTRACT

Additive Manufacturing (AM) and in particular Fused Filament Fabrication (FFF) is considered as a common method to manufacture parts for different applications. The variety of materials that FFF offers makes this technology very useful in different industrial fields, such as ground transportation and aerospace. High-Temperature Plastics (HTPs) like polyetheretherketone (PEEK) and polyetherimide (PEI) offer great mechanical and thermal properties that can be further improved with the addition of reinforcements such as carbon fibres (CF) to create High-Temperature Reinforced Plastics (HTRPs). Commercial materials for high-performance applications are currently available on the market, but the variety of these materials is limited and their price is considerably high. This project used an open-source FFF printing machine with heated chamber (AON-M2) to print newly developed HTRPs based on PEI (commercial name: ULTEM). PEI presents better mechanical properties than standard printing materials like polylactic acid (PLA) or the acrylonitrile butadiene styrene (ABS) but materials cost is reduced by half compared to PEEK. Developed materials by the Laboratory for Multiscale Mechanics (LM2) and the National Research Council (NRC) of Canada with different percentages of CF and Thermal Black (TB) reinforcements were printed. Composites containing up to 40 wt.% CF were printed. The mechanical properties of the samples 3D printed with commercial HTPs and HTRPs and with the developed advanced composites were evaluated using the tensile test standard ASTM D638 (Standard Test Method for Tensile Properties of Plastics). The maximum Young's modulus and Ultimate Tensile Strength (UTS) obtained for the samples 3D printed with the reinforced developed filaments was 3.3 GPa and 47 MPa, respectively. In addition, the samples were analyzed by Scanning Electron Microscopy (SEM) and micro Computed Tomography (micro-CT). The images obtained with SEM and micro-CT allowed to understand the relationship between the mechanical properties and the porosities inside the samples, which in the case of the developed materials were ∼16 %.

TABLE OF CONTENTS

ACKNOWLEDGEMENTS iii

RÉSUMÉ iv

ABSTRACT v

TABLE OF CONTENTS vi

LIST OF FIGURES viii

LIST OF TABLES xiii

LIST OF ACRONYMS AND ABBREVIATIONS xiv

CHAPTER 1 INTRODUCTION 1

CHAPTER 2 LITERATURE REVIEW 3

2.1 Introduction of the literature review 3

2.2 Additive Manufacturing (AM) 3

2.2.1 Additive Manufacturing in industry 4.0 3

2.2.2 AM technologies: Fused Filament Fabrication (FFF) 3

2.3 Additive manufacturing of HTP and HTRP 5

2.3.1 High Temperature Plastics (HTP) and High Temperature Reinforced Plastics (HTRP) 5

2.3.2 FFF printing parameters for HTPs 6

2.3.3 3D printing technology for HTP and HTRP 10

2.4 Improvement of the printing process and its productivity 11

2.4.1 High printing productivity 11

2.4.2 Nozzle shape modification 16

2.5 3D printing in the aerospace field 18

2.5.1 Printing of high performance polymers for aerospace applications 18

2.5.2 3D printing of sandwich panels for aerospace applications 19

2.6 Characterization methods for FFF printed parts 21

2.6.1 Characterization methods 21

2.6.2 Characterization of printed parts by offline OCT 23

2.7 Conclusions of the literature review 25

CHAPTER 3 APPROACH AND CONTEXT OF THE RESEARCH WORK 26
3.1 Approach to the research work 26
3.2 Context and coherence with the objectives of the 3DREAM project 27

CHAPTER 4 MATERIALS AND METHODS 28
4.1 Printing materials 28
4.1.1 Commercial materials 28
4.1.2 Developed materials 28
4.2 3D printing process 29
4.2.1 3D printing machines 29
4.2.2 3D printing parameters selection 33
4.3 Characterization methods 36
4.3.1 Mechanical tests 36
4.3.2 Optical microscopy 37
4.3.3 Scanning Electron Microscopy (SEM) 38
4.3.4 Micro Computed Tomography (micro-CT) 39

CHAPTER 5 EXPERIMENTAL RESULTS AND DISCUSSION 40
5.1 3D printing of commercial filaments 40
5.1.1 Characterization results for printed parts made of Com. Pure filaments 40
5.1.2 Characterization results for Com. Reinf. filaments 46
5.1.3 Discussion of results obtained with Com. Pure and Com. Reinf. filaments 50
5.2 3D printing of developed materials 51
5.2.1 3D printing of LM2 filaments 51
5.2.2 3D printing of NRC filaments 54
5.2.3 Discussion of results obtained with developed filaments 64

CHAPTER 6 CONCLUSIONS 66
6.1 Summary of works 66
6.2 Recommendations for future research 67

REFERENCES 68

APPENDIX A: STRESS-STRAIN CURVES FOR COM. PURE AND COM. REINF. FILAMENTS 72

LIST OF FIGURES

Figure 2.1: Schematic of FFF using 2 material spools: a printing and a support material [5]..... 4

Figure 2.2 : Three construction directions used to print the tensile test samples : on its edge, flat and upright [21] 9

Figure 2.3: Plots showing the relation between extruder force and building rate using a) different nozzle diameters (0.1/0.25/0.5/1 mm), b) different liquefier length (10/20/30 mm) [28]..... 12

Figure 2.4: SEM images from the fracture section of the tensile test samples printed with PEEK at a) 25 mm/s and c) 5 mm/s and CF reinforced PEEK printed at b) 25 mm/s and d) 5 mm/s [33]. 13

Figure 2.5: Effect of time on the temperature of consecutive layers printed with ABS for a) BAAM and b) FFF [38]..... 14

Figure 2.6: Examples of researched nozzles: a) Nozzle geometries with the respective deposited filament shape [40] b) Nozzle adapter with interchangeable custom-made nozzles [43]. 17

Figure 2.7: 3D printed parts for the aircraft cabin made with flame-retardant approved HTPs: a) air grill for a 747 cockpit ventilation duct and b) spacer panel for the Finnair's A320 [48]. 18

Figure 2.8: SEM images of FFF samples printed wih PEI at a 0° raster angle and nozzle temperatures : a) 350°C, b) 360°C, c) 370°C and d) 380°C [16]. 22

Figure 2.9: Micro-CT image of feedstock filament of carbon fibre reinforced PEEK: a) an homogeneous void distribution where the reinforced PEEK is in grey color and b) and an inhomogeneous distribution of the fibres in red color mainly located in the external part of the filament, PEEK is represented by blue in the internal cylinder and by green in the external part of the filament [55]. 23

Figure 2.10: Measurement comparison of an FFF printed part with PLA between OCT and SEM at different printing temperatures. a) shows the SEM and OCT images obtained the printed parts at

different printing temperatures. b) shows the plots for filament height, spacing and width of printed roads measured by both analysis techniques [61]..... 24

Figure 4.1: a) The LM2 customised 3D printer and b) the Rumba board used to control this 3D printer with the different connections for the axis movements, temperatures and powers. 30

Figure 4.2: a) AON-M2 and b) interior view of the heat chamber..... 30

Figure 4.3: Example of the selection of the printing parameters in Simplify3D..... 33

Figure 4.4: a) 3D Model of the ASTM D638 Type 1 dogbone in Simplify3D and b) zoom image of the 2 external layer (blue and green) and the top internal layer (orange) of the dogbone at 45° raster angle..... 36

Figure 4.5: Example of a tensile test of PEI reinforced ASTM D638 Type 1 dogbone with 20 wt.% CF with the MTS Insight, the load cell and extensometer measuring the force and the deformation applied on the sample. 37

Figure 4.6: Optical microscope system with the Olympus SZX-12, the Evolution VF CCD camera and the external light source. 37

Figure 4.7: SEM samples of 4 different blends from the developed materials by the NRC. The 4 samples on top show the top printed surface and the 4 samples at the bottom show the fracture surface. From left to right : 20 wt.% rCF, 15 wt.% rCF – 5 wt.% TB, 10 wt.% CF – 10 wt.% TB and 20 wt.% TB. 38

Figure 4.8: Interior of the micro-CT equipment Zeiss X-Radia Versa 520 used to study the printed samples 39

Figure 5.1: a) Plot of the calculated average speed (with logarithmic dotted trend line) and speed reduction percentage with respect to the theoretical printing speed for 1 printed layer of an ASTM D638 dogbone. b) Schematic of the zig-zag printhead movement during the printing process of a

dogbone divided by printing linear segments that were printed following the directions of the arrows. 41

Figure 5.2: Stress-strain graph (ASTM D638) for the lowest printing speed tested (20 mm/s) with Com. Pure filaments printed with a 0.4 mm nozzle and with a nozzle temperature of 370°C. 42

Figure 5.3: Young's modulus results of Com. Pure filaments from the TDS Ref [62] and for three different printing speeds (20, 40 and 60 mm/s) with 95% confidence interval. 42

Figure 5.4: UTS values of Com. Pure filaments from the TDS Ref. [62] and for three different printing speeds (20, 40 and 60 mm/s) with 95% confidence interval. 43

Figure 5.5: SEM images of the top surface of the Com. Pure printed dogbones at different printing speeds. a) example of broken sample showing the studied top region by a black square. SEM images for b)20mm/s, c) 40 mm/s and d) 60 mm/s using the AON-M2 printer. 44

Figure 5.6: SEM images of the fractured surfaces of the Com. Pure printed dogbones at different printing speeds a) 20 mm/s, b) 40 mm/s and c) 60 mm/s. The yellow circles show the periodicity of the holes. 44

Figure 5.7: Micro-CT images of the neck cross section of the Com. Pure dogbones printed at a) 20 mm/s and b) 60 mm/s. 45

Figure 5.8 : Stress-strain graph (ASTM D638) for the lowest printing speed tested (20 mm/s) with Com. Reinf. filaments printed with a 0.4 mm nozzle and with a nozzle temperature of 400°C. 46

Figure 5.9: a) Young's modulus and b) UTS results of commercial Com. Reinf. filaments for three different printing speeds (20, 40 and 60 mm/s) with 95% confidence interval and the TDS Ref. values [63]. 47

Figure 5.10: Tensile test (ASTM D638) results for Com. Reinf. Filaments with a nozzle temperature of 420°C and an extrusion multiplier of 1.1. 48

Figure 5.11: SEM image of the upper surface for the printed Com. Reinf. dogbones at a) 20 mm/s, b) 40mm/s and c) 60 mm/s. SEM images of the fractured surface of the of the printed Com. Reinf. dogbones at d) 20 mm/s, e) 40mm/s and f) 60 mm/s. 49

Figure 5.12: Micro-CT images showing the high degree of porosity for Com. Reinf. printed sample at 40 mm/s 50

Figure 5.13: Printed 15 x 15 x 15 mm^3 cubes (theoretical size values) with LM2 filaments made of ULTEM 1040 and their optical microscope image from the lateral face respectively with: a) and b) 10 wt.% CF, c) and d) 20 wt.% CF, e) and f) 30 wt.% CF and, g) and h) 40 wt.% CF. 53

Figure 5.14: Warping phenomenon occurring during the 3D printing of a dogbone using the NRC filament reinforced with 20 wt.% rCF. 55

Figure 5.15: Tensile tests specimens (before testing) printed in the AON-M2 with the NRC filaments made of ULTEM 1040 with 4 different formulations: a) 20 wt.% rCF, b) 15 wt.% rCF – 5 wt.% TB, c) 10 wt.% rCF – 10 wt.% TB and d) 20 wt.% TB. 56

Figure 5.16: Tensile tests specimens (after testing) printed in the AON-M2 with the NRC filaments made of ULTEM 1040 with 4 different formulations: a) 20 wt.% rCF, b) 15 wt.% rCF – 5 wt.% TB, c) 10 wt.% rCF – 10 wt.% TB and d) 20 wt.% TB. 57

Figure 5.17: Stress-strain graphs (ASTM D638) for the four NRC filaments printed with a 0.4 mm nozzle and with a nozzle temperature of 400°C: a) 20 wt.% rCF, b) 15 wt.% rCF - 5 wt.% TB, c) 10 wt.% rCF – 10 wt.% TB and d) 20 wt.% TB. 58

Figure 5.18: Young's modulus results for the samples 3D printed with the four formulations of NRC filaments: 20 wt.% rCF, 15 wt.% rCF – 5 wt.% TB, 10 wt.% rCF – 10 wt.% TB and 20 wt.% TB. 60

Figure 5.19: UTS results for the samples 3D printed with the four formulations of NRC filaments: 20 wt.% rCF, 15 wt.% rCF – 5 wt.% TB, 10 wt.% rCF – 10 wt.% TB and 20 wt.% TB. 60

Figure 5.20: Micro-CT images showing the internal porosity of specimens printed with NRC filaments before testing with a) 20 wt.% rCF and b) 20 wt.% TB. 61

Figure 5.21: SEM images done after tensile test for the 4 different formulations of NRC filaments for the top and fracture regions respectively: a) and b) 20 wt.% rCF, c) and d) 15 wt.% rCF - 5 wt.% TB, e) and f) 10 wt.% rCF - 10 wt.% TB, g) and h) 20 wt.% TB. 63

Figure 5.22: SEM image of the cross section of an NRC filament made of ULTEM 1040 with 20 wt.% rCF where porosities smaller than 100 µm are observed (yellow circles). 64

Figure A.1: Stress-strain graphs for ASTM D638 specimens printed with Com. Pure filaments with a 0.4 mm nozzle and with a nozzle temperature of 370°C at 2 printing speeds : a) 40 mm/s and b) 60 mm/s. 72

Figure A.2: Stress-strain graphs for ASTM D638 specimens printed with Com. Reinf. filaments with a 0.4 mm nozzle and with a nozzle temperature of 400°C at 2 printing speeds: a) 40 mm/s and b) 60 mm/s. 73

LIST OF TABLES

Table 2.1: Comparison of ULTEM 9085, ULTEM 1000 and CF reinforced ULTEM 1000 by injection molding and FFF [14]..... 8

Table 2.2: Summary of articles related to high speed and productivity enhancement for extrusion-based AM technology..... 16

Table 2.3: Types of core geometries of evenly spread and longitudinally oriented sandwich panels and geometric parameters for the pattern of the honeycomb sandwich structure [49]..... 19

Table 2.4: Summary of works related to OCT applied to AM 24

Table 4.1 : Commercial filaments and developed advanced composites with different wt.% of reinforcements and with their respective printing parameters: nozzle diameter, printing speed, nozzle temperature, bed temperature, chamber temperature and layer height. 34

Table 5.1 : Printing tests (15 x 15 x 15 mm3 cube) performed with the LM2 filaments made of different ULTEM grades and wt.% of CF on the LM2 customised 3D printer. (*unfinished printed cube due to blockage of the nozzle) 52

LIST OF ACRONYMS AND ABBREVIATIONS

3DREAM	3D Research Ecosystem for Additive Manufacturing
ABS	Acrylonitrile butadiene styrene
AM	Additive Manufacturing
BAAM	Big Area Additive Manufacturing
CF	Carbon Fibres
CNF	Carbon Nanofibres
Com. Pure	Commercial Pure 3D printing filaments made of Ultem 1010
Com. Reinf.	Commercial CF Reinforced 3D printing filaments made of Ultem 1010
DIW	Direct Ink Writing
DMA	Dynamic Mechanical Analysis
E	Young's modulus
E'	Storage modulus
E''	Loss modulus
FDM	Fused Deposition Modelling
FFF	Fused Filament Fabrication
HTP	High-Temperature Plastics
HTRP	High-Temperature Reinforced Plastic
IoT	Internet of Things
LAAM	Large Area Additive Manufacturing
LM2	Laboratory of Multiscale Mechanics
micro-CT	micro Computed Tomography
NRC	National Research Council of Canada
OCT	Optical Coherence Tomography
PAEK	Polyaryletherketone
PEEK	Polyetheretherketone
PEI	Polyetherimide
PEKK	Polyetherketoneketone
PLA	Polylactic acid
PLC	Programmable Logic Controller
PPS	Polyphenylene sulfide
rCF	Recycled Carbon Fibres

SEM	Scanning Electron Microscopy
TB	Thermal Black
TDS	Technical Data Sheet
T_g	Glass Transition Temperature
UTS	Ultimate Tensile Strength
δ_A	Absolute accuracy
δ_R	Relative accuracy

CHAPTER 1 INTRODUCTION

The use of additive manufacturing (AM) for high-performance applications, such as aerospace or medicine, has been increasingly investigated in recent years. The interest in 3D printing technologies, and in particular in Fused Filament Fabrication (FFF), is based on the flexibility that they offer when building a part. The 3DREAM (3D Research Ecosystem for Additive Manufacturing) project aims to encompass different fields of 3D printing such as the material used, process optimization as well as machine vision, modelling and simulation with the objective of printing parts for the transportation sector. The National Research Council (NRC) of Canada, with Dr. Mihaela Mihai and her team, initiated and put in place the 3DREAM project together with Polytechnique Montreal and the research team of the laboratory for multiscale mechanics (LM2) with the main supervisor of this master thesis, Professor Daniel Therriault and the co-supervisor Professor Martin Lévesque. The PhD student Dogan Arslan from the LM2 is working on the development of High Temperature Plastics (HTP) and High Temperature Reinforced Plastics (HTRP) for 3D printing. In this context, this master thesis is part of this important R&D project and industrial group that is aimed to contribute to the advancement of the FFF 3D printing technology for high temperature plastics for the future construction of sandwich panels for aerospace applications. In addition, 13 industrial partners chosen all along the AM value chain are directly involved in 3DREAM.

The increase in productivity for AM technologies is a main factor to consider them for the industrial utilisation, potentially replacing current manufacturing methods for high complexity shapes and prototyping. The important diversity of thermoplastic polymers and their composites that can be used together with the freedom offered by open-source 3D printers are the keys to achieve the full potential of the printing process at an industrial scale. In this project, commercial high temperature materials were initially tested to better understand the printing process and the mechanical properties of the printed parts. After that, developed reinforced high temperature advanced composites were used to study their printability. The mechanical performance of the obtained 3D printed samples was assessed following the ASTM D638

standard while their micro-structures and macro-structures were observed using techniques such as scanning electron microscopy (SEM) and micro computed tomography (micro-CT).

This research thesis contains a literature review (Chapter 2) that presents the state of the art in the field. The approach used to perform this research work is explained in Chapter 3. Chapter 4 shows the experimental methodology with details on materials and methods while Chapter 5 presents the obtained experimental results. Finally, Chapters 6 and 7 are the general discussion and conclusions with recommendations for future work, respectively.

CHAPTER 2 LITERATURE REVIEW

2.1 Introduction of the literature review

The objective of this chapter is to present the technology related to 3D printing of thermoplastics and in particular to high temperature plastics (HTP). First, the importance of Additive Manufacturing (AM) in industry 4.0 is explained together with one of the main 3D printing technologies, Fused Filament Fabrication. In addition, the state of the art of AM of HTPs, high-temperature reinforced plastics (HTRP) is presented and the 3D printing parameters are listed and explained. This literature review discloses the main factors to increase the productivity for Fused Filament Fabrication. Finally, the main characterization methods for analyzing printed samples are presented. The 3D printed samples studied using SEM, micro-CT and Optical Coherence Tomography (OCT) were selected from the published scientific literature and were given as examples of these characterization methods.

2.2 Additive Manufacturing (AM)

2.2.1 Additive Manufacturing in industry 4.0

Industry 4.0 is characterized by the increase in automation of the manufacturing process and other industrial practices by developing self-monitoring, communication between systems and use of smart machines able to self-diagnose [1]-[2]. There are several technologies that are being developed under these guidelines such as digital twins, internet of things (IoT), cloud computing and 3D printing or AM [3].

2.2.2 AM technologies: Fused Filament Fabrication (FFF)

3D printing offers many different techniques: Fused Filament Fabrication (FFF), powder bed fusion (PBF), Selective Laser Sintering (SLS), Selective Laser Melting (SLM), Stereolitography, Direct Energy Deposition (DED) or Laminated Object Manufacturing (LOM) [4].

Fused Filament Fabrication (FFF), also known as Fused Deposition Modelling (FDM), is one of the main 3D printing technologies used nowadays. A filament, made from an extruded thermoplastic

or composite, is extruded at high temperature and deposited while the desired shape is built. The process consists in heating the printing material until it reaches its melted state, extruding it through a nozzle onto a building platform and then let it cooling down until it solidifies [5]. Figure 2.1 shows a schematic of the FFF process using 2 material spools: one for the 3D printing of the part and another for the supports necessary for the correct construction of the desired shape.

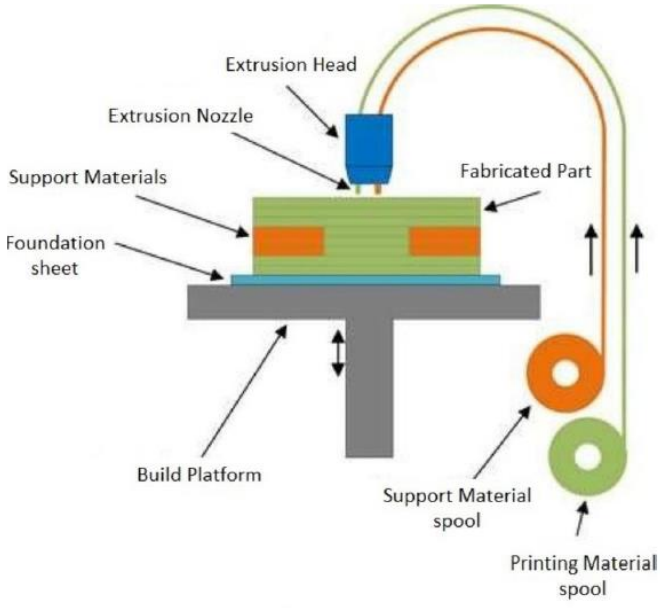

Figure 2.1: Schematic of FFF using 2 material spools: a printing and a support material [5]

FFF offers many benefits such as low costs, the simplicity of the process or its ability for rapid prototyping [4]. In addition, the advantages offered by FFF are common compared to other AM technologies. The flexibility and design freedom allows customised production and the ability to readapt the product. There is a simplification of the product development cycle shortening the time to market [6]. Moreover, 3D printing can contribute to an environmentally sustainable world [7]. When compared to other manufacturing technologies, it produces less waste material and it can produce complete parts without the need to transport the material to different assembly sites. The weakest points of FFF are mainly related to the control of the properties of the final product due to anisotropy of the printed parts. The mechanical properties reduction due to the inter-layer adhesion represents a challenge [8]. Another weakness is the limited build volume, which in many cases restricts the sizes of the printed parts. Other challenges for FFF technology are the printing speed, which considerably delays industrial manufacturing, when

compared to injection molding and the need for certification of the printed parts to assure certain mechanical properties [6]. FFF is not only the most widely used 3D printing technology today, but experts expect it to be the most widely used AM technology in the near future [9].

2.3 Additive manufacturing of HTP and HTRP

2.3.1 High Temperature Plastics (HTP) and High Temperature Reinforced Plastics (HTRP)

The FFF technology uses thermoplastic polymers as raw materials such as polylactic acid (PLA) or acrylonitrile butadiene styrene (ABS). However, AM is increasingly focusing on high performance applications. High Temperature Plastics (HTP) such as polyetherketoneketone (PEKK), polyetheretherketone (PEEK), polyphenylene sulfide (PPS), or polyetherimide (PEI), having high melting temperatures between, i.e. from 350 to 400°C, are being studied with the purpose to fulfill the new challenges for AM. Heated closed chambers, i.e. an environment having a temperature higher than 100°C, are required for those thermoplastics to be able to build parts. In addition, the build plate can potentially reach temperatures of almost 200°C. Before the aforementioned HTPs can be used in 3D printing, the advanced thermoplastic polymer is first compounded at high temperature by adding reinforcements and/or fillers, and, secondly, is extruded again at high temperature to transform the advanced composites in filaments of 1.75 or 2.85 mm diameter.

PEEK is a semi-crystalline polymer from the polyaryletherketone (PAEK) family of polymers and is one of the most explored high performance thermoplastic due to its relatively high properties. The tensile strength achieved by the printed parts of this material is 87.6 MPa and the printing temperature varies from 360°C to 450°C [10]. The main drawback of PEEK is its crystallinity that prevents the layers adhesion during the construction of the 3D printing part. Another drawback is the high cost of the commercial filaments for FFF that is around $600/kg. In the case of PEKK, the FFF market offers filaments at around $700/kg [11].

PEI (commercial name: ULTEM), an amorphous thermoplastic, is one promising high performance material used for FFF. Ding et al. performed a comparison study of mechanical properties between PEI and PEEK where they tried to optimize the nozzle temperature [12]. The results showed that the optimal flexural and tensile strengths were around 12 and 5 MPa higher for PEEK (Flexural: 135 MPa; Tensile: 84 MPa) than for PEI (Flexural: 123 MPa; Tensile: 79 MPa). They also studied how the density of the printed parts varied with the temperature of the nozzle, with PEEK and PEI attaining 0.925 and 0.900 as the maximum printing relative densities. In addition, PEI showed a much more brittle fracture behaviour than PEEK. Another main difference between these materials is the glass transition temperature (T_g). T_g is the temperature at which the polymers perform the transition in amorphous materials from the "glassy" state (hard and brittle) into a rubbery or viscous state [13]. Among the mentioned HTPs, PEI has the highest T_g (217°C), when compared to PEEK (143°C) or PEKK (162°C) [14]. PEI has slightly lower properties than PEEK but still PEI properties are sufficiently high to be used in demanding applications. The main advantage of PEI filaments is their price, which is less expensive, from $200/kg to $300/kg, depending on the manufacturer [15]-[16].

The addition of reinforcements such as carbon fibres (CF) to advanced thermoplastics of high-melting temperatures through compounding process results in High Temperature Reinforced Plastics (HTRP). HTRPs have improved mechanical properties in comparison with its respective HTPs. In addition, the viscosity of the melted HTRPs is also higher due to the shear stresses inside the material produced between the reinforcements and the polymer, what hinders the extrusion printing process [17].

2.3.2 FFF printing parameters for HTPs

For HTPs, the FFF-part performance is directly related to some intrinsic parameters specific to this technology, such as: nozzle diameter (0.2, 0.4, 0.8 mm, etc.) and type, layer thickness (0.1, 0.2, 0.3 mm, etc.), infill ratio (10, 25,...90, 100%), infill pattern (rectilinear, grid, triangular, etc.), raster orientation (0, 45, 90°, etc.), printing orientation (flat, upright, on-edge), extrusion flow

rate or air gap (positive, zero, negative). Other intrinsic parameters are linked to the post-processing such as: thermal post-processing methods (annealing) [18]. The common structure for these articles is the selection of two or three parameters to study their effects on the mechanical properties of the printed parts. Jiang et al. studied two parameters with ULTEM 1000: the raster angle (printing direction) and the nozzle temperature [19]. The parameters were optimized to maximize the tensile strength and toughness of the printed samples. The authors showed that the optimal raster angle and nozzle temperature for these tests were 0° (filaments have the same direction as the stresses applied) and 370°C, where the maximum values for tensile strength (104.1 MPa) and notched impact strength (5.5 kJ m^{-2}) were achieved. Ding et al. also studied the effect of the nozzle temperature on PEI 3D printed parts and they concluded that the highest flexural strength as obtained at 420°C for a flexural strength of 123 MPa [12]. When comparing the tensile results of the printed parts with the injection moulded parts, there is a clear reduction in the values obtained for the printed parts. The tensile strength of the printed parts reached 112 MPa, only 80% from the performance of injected parts. Similarly, the ultimate tensile strength (UTS) value of the parts printed by Jiang et al. [19] also achieved 80% of that obtained with injection molding. Printed ULTEM 9085 exhibited tensile strength and tensile modulus, respectively, 87% and 64% of the values obtained for injection molded specimens of the same material [19]. The printed CF (10 wt.%) reinforced ULTEM 1000 showed a lower tensile strength, when compared to printed ULTEM 9085, due to a high nozzle temperature (420°C) that degraded de polymer and caused a volume expansion (due to trapped moisture and air). The volume expansion created a high level of porosity (25%) in the samples [14]. Even so, the Young's modulus was found to be higher, when compared to the pure PEI specimens.

Table 2.1: Comparison of ULTEM 9085, ULTEM 1000 and CF reinforced ULTEM 1000 by injection molding and FFF [14].

Resin type Properties	Ultem 9085 Injection Molded (Sabic data)	Ultem 9085 FDM printed (Stratasys data) 0°	Ultem 9085 FDM rp+m (GRC tested) ±45°	Ultem 1000 Injection Molded (Sabic data)	Ultem 1000+10wt% AS4 chopped C-fiber FDM rp+m (GRC tested) 0°/±45°
Tensile Strength (MPa)	83	72	62 ± 0.1	110	50±0.9/44±0.3
Tensile Modulus (MPa)	3,432	2,200	2,230 ± 12	3,579	2,901±48/2248±46
Flexural Strength (MPa)	137	115	92 ± 2	165	tbd
Flexural Modulus (MPa)	2,913	2,500	1,901 ± 41	3,511	tbd
Compression Strength (MPa)	n/a	104	tbd	n/a	tbd
Compression Modulus (MPa)	n/a	1,930	1,890 ± 32	n/a	tbd

Table 2.1 shows the comparison with the mentioned properties for the different PEI grades investigated in [14], where rp+m stands for 'rapid prototyping plus manufacturing' and they represent the results obtained with Stratasys Fortus 400 mc, a closed-source 3D printer.

The building orientation is another parameter that was studied to understand its effect on the mechanical properties of the final 3D printed parts. Increasing the angle with respect the building surface produced printed structures with printed filaments that were not in the main direction of the load, which resulted in lower apparent mechanical properties. Tensile specimens of ULTEM 9085 were printed with different building orientations to study their effect on the apparent tensile properties of the 3D printed parts [20]. The optimal direction was observed to be 0º to the build plate while both main faces were printed vertically. Fischer et al. also studied the influence of the building direction of the ULTEM 9085 dogbones on the fatigue behavior with three construction directions. Figure 2.2 shows the three construction directions tested to print the ASTM tensile test samples: on its edge, flat and vertical (upright). The data showed that the edge printed dogbones presented the best tensile strength and elongation at break properties [21].

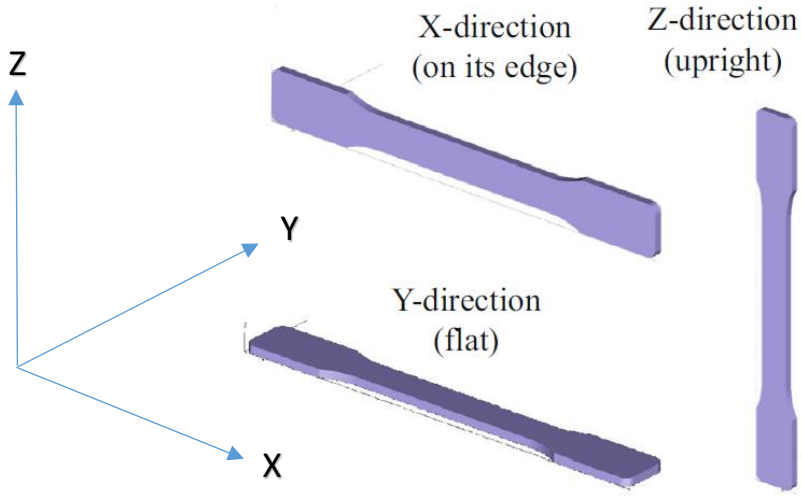

Figure 2.2 : Three construction directions used to print the tensile test samples : on its edge, flat and upright [21]

A common characterization method used to study the mechanical properties of the printed parts is the Dynamic Mechanical Analysis (DMA). DMA applies a sinusoidal load to measure strain in the studied material and then the complex modulus among other properties is determined. Jiang et al. performed DMA with the variation of ambient temperature. A clear reduction of the storage modulus (E') and a peak for the loss modulus (E") at almost 217°C, closely related to the T_g of PEI, were obtained [19]. The effects were observed most clearly for the specimens printed at 0°. The DMA results showed that the best results about the number of fatigue cycles to failure for flat and on the edge printed dogbones were 8272 ± 342 cycles on the edge and 8337 ± 1501 cycles for flat. Arivazhagan et al. printed ULTEM 9085 to study E' and E" with a 3 point bending DMA. The parameters considered were the raster width (0.406, 0.606 and 0.781 mm) and raster angle (0°, 30° and 45°). The E', E" and flexural modulus did not seem to be strongly influenced by these parameters. However, the complex viscosity increased a 10 % with the increase of the raster width and raster angle [22]. The tan delta and T_g behaved similarly to the increase of the raster angle and width. In conclusion, the existent studies about PEI were mainly dedicated to the optimization of FFF printing parameters for ULTEM 9085, and a few of them to ULTEM 1000. Only the effects of nozzle temperature, raster angle, building directions and filament width were observed on the mechanical performance of printed specimens. Therefore, many parameters of FFF technology remained unstudied for some PEI grades like ULTEM 1040. The relationship

between printing parameters like printing speed or printing temperatures and 3D printed part performance is not yet fully understood and solved.

2.3.3 3D printing technology for HTP and HTRP

Stratasys 3D printers like Fortus 450 or the Fortus 900 monopolize the printing of HTRP for industrial scale with high prices between $150000 and $250000 [23]. These printers work like a “black box” in the sense that they print the parts but the printing process is minimally modifiable by the user. The “black box” architecture blocks the development and improvement of the printing process for HTP and HTRPs. Furthermore, Stratasys printers demand the use of their own filament spools that are more expensive than standard spools and the range of available materials is limited to those offered by the company. New high temperature industrial printers like the AON-M2 present an opportunity for open-source printing development at a competitive starting price of $50000 [24]. The AON-M2 allows modifying the printing process and precisely adjusting a large number of parameters with a slicer software (Simplify3D). Among the modifiable parameters are the different printing temperatures, general and specific speeds for each printing zone as well as dimensions and volumes of the extruded filament. Open-source industrial printers together with high-quality components like Dyze Design nozzles represent strong support for the future of high performance 3D printing for aerospace and other industrial applications. Dyze Design has developed high-temperature nozzles and hot-ends that are optimal for printing polymers such as PEI, PEEK or their composites containing different types of reinforcements. Some of their designs include a double pinch drive system to increase the pushing force with a lower filament force to avoid filament damage. The increase of the pushing force help to print reinforced materials that have fibres inside and that tend to block the nozzle. In addition, the developed tungsten carbide nozzles improve the flow of the melted material by keeping the hot temperature at the tip, which allows higher printing speeds [25].

2.4 Improvement of the printing process and its productivity

2.4.1 High printing productivity

High throughput printing systems are one of the keys to industrialize AM technology and increase large-scale production. In the LM2 research group, extrusion based high speed 3D printing has been recently studied by our colleagues. Brzeski et al. achieved a printing speed of 175 mm/s for micro scaffolds by using Direct Ink Writing (DIW) printing technology [26]. Chauvette et al. used a multinozzle to extrude 26 filaments simultaneously, achieving speeds of 250 mm/s to print large networks of micro scaffolds with periodic features [27]. These research works use a material made of microcrystalline wax and petroleum jelly which allows higher extrusion rates compared to thermoplastics in FFF. In this context, the determining factors of high-speed FFF are related to the extrusion mechanism, the liquefier, the nozzle and the motion gantry system [28]:

- The extrusion mechanism: Dyze Design is one of the main producers of this mechanical system in Canada. In the case of the filament feeding, the power of the stepper motor that feeds the extruder needs to be able to push the filament at a high-flow rate to achieve high printing speeds. This system works together with a heating system that melts the printing material to make it flow through a nozzle. The usual melt flow for an extruder is between 0.05 kg/h and 0.1 kg/h of printing material [29]-[30]. Another type of extrusion mechanisms are the pellet extruders. Pellet-based extrusion systems permit higher melt flows (2.5 kg/h or more) and a reduction of the costs of printed parts due to the direct use of pellets with no need to transform them in filaments [31].

- The nozzle: a smaller diameter requires a higher force from the motor. In Figure 2.3 a), Go et al. tested the influence of different nozzle diameters (from 0.1 mm to 1 mm) with respect to the applied extrusion force and the build rate using filament feedstock. For the same build rate (75cm^3/h), nozzle diameters of 1 mm and 0.1 mm required a force of 14 N and 50 N respectively [28]. Furthermore, a larger diameter reduced the chances of blocking the nozzle and maintained a continuous flow at the polymer melt.

- The heater or liquefier: the length of the liquefier acts as a highway along which the filament travels as it melts. The longer it is, the easier and less force is required to push the material through the nozzle. In addition, if the molten polymer spends more time in the hot channel, the printing speed can be increased considerably. In Figure 2.3 b), three different lengths for the liquefier were studied. The longest liquefier (30 cm) achieved more than twice the flow rate of the original (10 cm) with the same applied force [28].

- The gantry system: It usually consists of a motor that transforms the movement in two perpendicular directions in space by means of belts. The limitation usually comes from the system's ability to keep pace when moving at high speeds, accelerating and braking to change direction. The printing speed (Vx) is computed with the mass conservation as per equation (1):

$$\frac{V_x}{V_A} = \left(\frac{D}{d}\right)^2, \tag{1}$$

where D is the extrusion filament diameter, d is the nozzle diameter and V_a the extrusion speed.

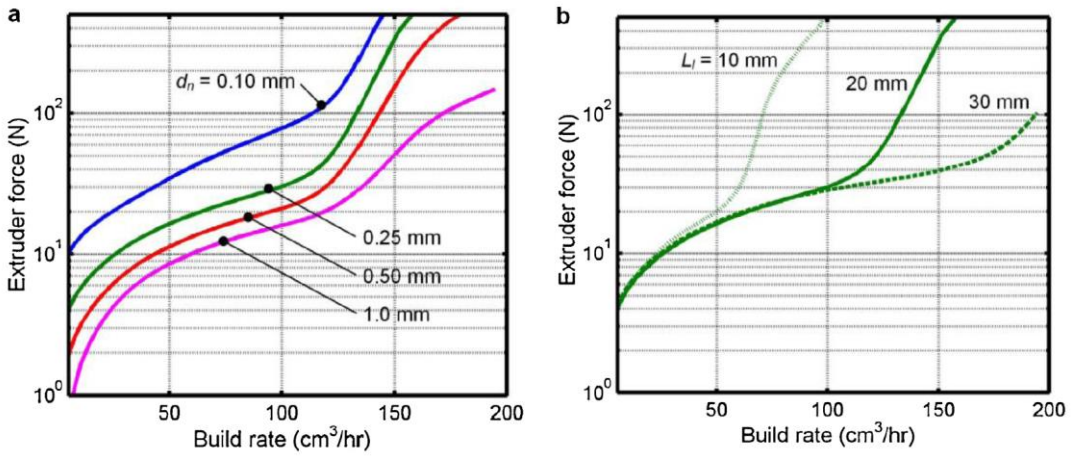

Figure 2.3: Plots showing the relation between extruder force and building rate using a) different nozzle diameters (0.1/0.25/0.5/1 mm), b) different liquefier length (10/20/30 mm) [28].

The printing speed together with the extrusion speed influences the microstructure and dimensions of the extruded HTPs. Increasing the printing speed for HTPs and HTRPs has a negative effect on the mechanical properties and density. Wang et al. showed that the difference

in quality of the printed parts due to the increase of the printing speed with PEEK was closely related to the nozzle diameter. Increasing the speed produced greater detrimental effects with surface roughness for thinner diameters (~0.4 mm) than for larger diameters (~0.8 mm) [32]. The reduction of the mechanical performance, such as for flexural and toughness, was also observed when the printing speed was increased. Peng et al. studied the influence of the printing speed with PEEK and PEEK reinforced with 10 wt.% CF [33]. The results stated that an increase in speed from 5 mm/s to 25 mm/s produced a reduction of around 10% for both, flexural and tensile strength (for both tested materials).

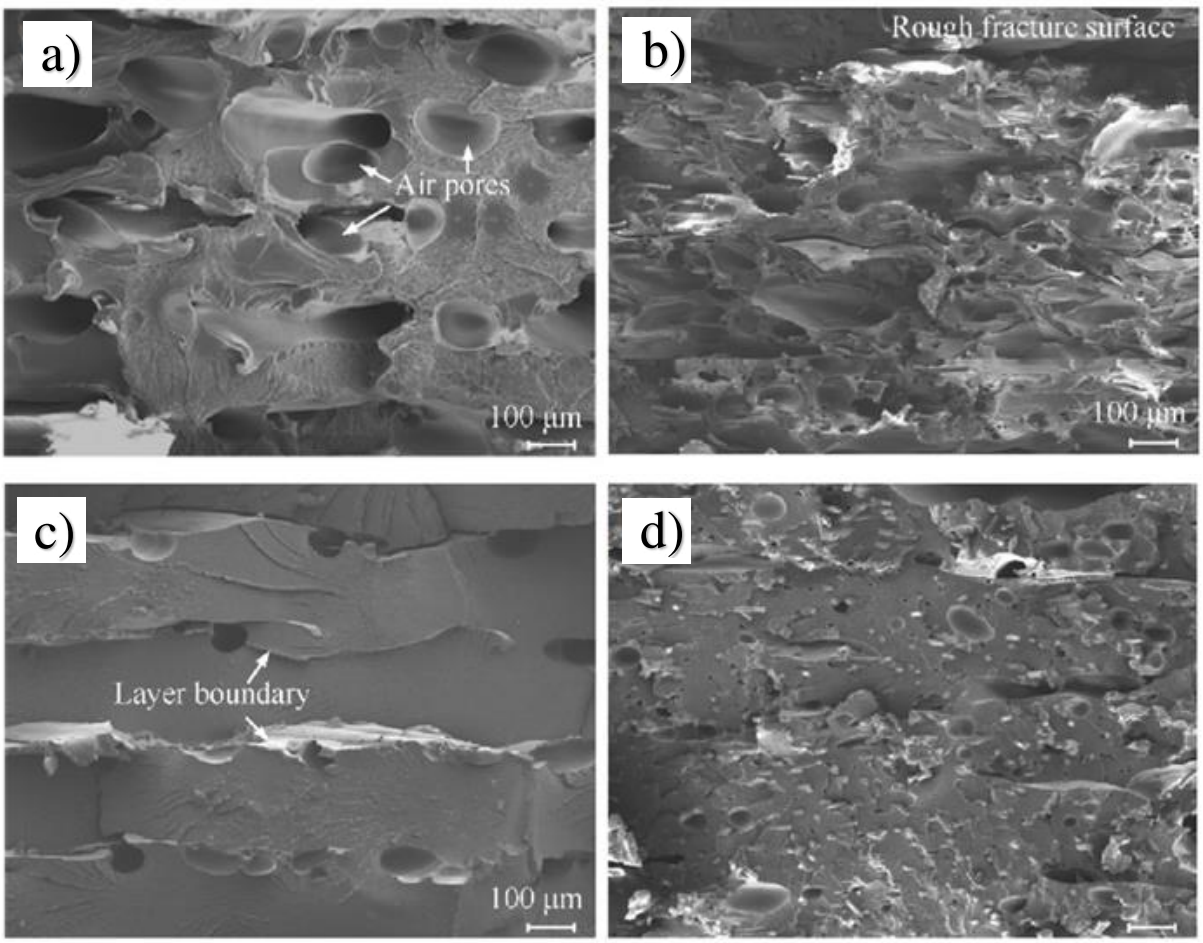

Figure 2.4: SEM images from the fracture section of the tensile test samples printed with PEEK at a) 25 mm/s and c) 5 mm/s and CF reinforced PEEK printed at b) 25 mm/s and d) 5 mm/s [33].

The reduction of the impact strength was 32% for pure PEEK and 55% reinforced PEEK. The SEM images of the fracture surface of the tensile test samples printed at high speed (25 mm/s) for pure PEEK in Figure 2.4 a), and for CF-PEEK in Figure 2.4 b) showed high porosity content and

voids larger than 100 µm. The SEM images at lower printing speed (5 mm/s) are shown in Figure 2.4 c) for pure PEEK and Figure 2.4 d) for CF-PEEK. They show a much lower content of porosities compared to the high printing speed. Therefore, increasing the printing speed in FFF is detrimental to the part structure and mechanical performance.

LAAM (Large Area Additive Manufacturing) also known as BAAM (Big Area Additive Manufacturing) systems have a typical printing volume of 6 m long × 2.4 m wide × 1.8 m high and are equipped with larger nozzle to increase the flow rate and the productivity of the printing process. The standard BAAM nozzle diameters range from 2.54 mm to 12.7 mm (or more) [34]. Ajinjeru et al. showed with ULTEM 1000 and CF (20 wt.%) reinforced PEI that longer processing times were required during the printing process with BAAM, since the printed filament had a larger diameter. However, the increase in viscosity (2.5x) with the addition of CF facilitated the processing of the printed part as it maintained the shape of the filament until solidification [35]. Another study with BAAM stated that with this technology, the polymer extrusion was 20 times less expensive and 200 times faster than standard extrusion filament-fed AM systems [36]. Since the printing flow rate with BAAM is high, the raw material is fed in a pellets shape instead of filaments, which reduce the cost of the material. A challenge of BAAM is the printing resolution due to the large diameters used in this technology. Chesser et al. developed a novel deposition nozzle that was able to print with two different diameters and to improve the geometric tolerances of the printed parts [37].

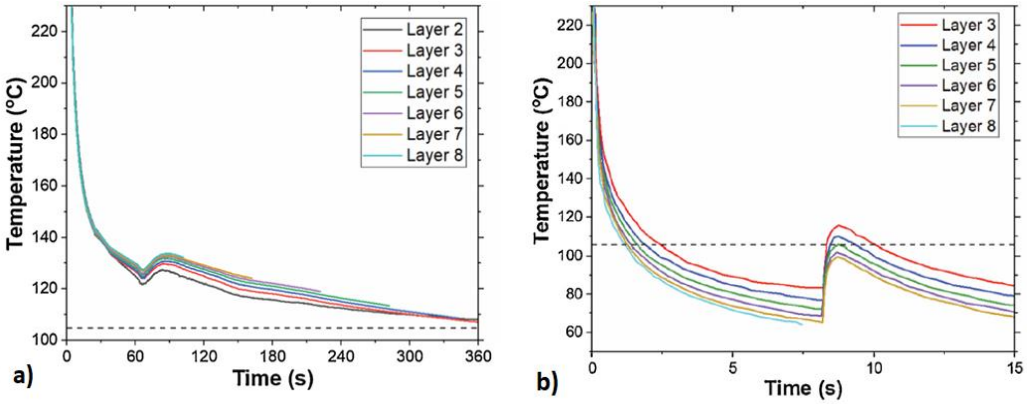

Figure 2.5: Effect of time on the temperature of consecutive layers printed with ABS for a) BAAM and b) FFF [38]

An important thermal effect that occurs with BAAM is the long cooling time that can last several minutes. Therefore, better inter-diffusion between the polymer layers might occur resulting in a better layer-to-layer adhesion. At the same time, a greater deformation of the lower layer can be produced due to the weight of the upper layers. Figure 2.5 a) shows that it took more than 6 minutes to reduce the temperature of ABS printed filament with BAAM under T_g [38]. However, the cooling time obtained by D'Amico et al. was much faster for FFF due to the smaller diameter of the printed filament. As seen in Figure 2.5 b), it took 2 seconds for ABS printed filaments to descend until T_g. Therefore, the short cooling period for FFF allows small nozzles to increase printing speed in FFF without causing thermal effects between consecutive layers due to high temperature of previous printed layers, which could deform the printed part [38]. Table 2.2 shows a summary of articles related to high speed and productivity enhancement for extrusion-based AM technologies. The articles mainly studied the influence of printing speed on the roughness and mechanical properties of the printed parts and some of them used HTPs or HTRPs as printing materials. BAAM articles studied different phenomena on the printed parts caused by the larger mass flows and nozzles used by this technology.

Table 2.2: Summary of articles related to high speed and productivity enhancement for extrusion-based AM technology.

Technology	Material	Study	Results	Ref.
DIW	Epoxy blend	Microscaffolds for acoustic applications	High speed printing at 175 mm/s	[26]
Extrusion	Organic paste like material (Wax/Petroleum)	Large scale microscaffold network printed with multinozzle	High speed printing at 250 mm/s with a multinozzle (26 filaments)	[27]
FFF	Thermoplastics (not specified)	Flow rate limits related to the extrusion motor, liquifier and gantry system	Recognise the limitant parameters for high-speed 3D printing	[28]
	PEEK	Effects of printing speed in tensile properties and density of parts	Surface roughness increases with printing speed. The smaller diameters are more sensitive to this effect	[32]
	PEEK/GF-PEEK/CF-PEEK	Influence of printing speed in mechanical properties	Reduction of tensile and bending (10%) and impact (55%) properties due to an increase of the printing speed	[33]
BAAM	CF-PEI	Material viscosity behaviour and effects of CF in the material	Addition of CF increases the shear thinning effect	[35]
	ABS/PPS/PEI/Reinforced	Interlaminar strength and process control	Voids (20 µm) between printed layer and microporosity	[36]
	ABS/CF-ABS	Problems related to print resolution and flow rate control	Improvement of geometric inaccuracy of printed parts by a novel developed nozzle	[38]
BAAM/FFF	ABS	Comparison of thermal behaviours and heat transfer between BAAM and FFF beads	Large difference in temperature in internal and external regions of a BAAM printed bead. Facilitates interlayer diffusion and weld formation	[37]

2.4.2 Nozzle shape modification

The shape of the nozzle is one of the printing features being investigated recently to improve the internal structure of the printed samples and therefore enhance the mechanical properties. Some researchers tried to adapt the shape of the nozzle to improve the alignment of the reinforced polymer fibres by changing some internal geometric parameters [39]. Heller et al. conducted a study by dividing the nozzle into several regions that were tested with different lengths and diameters. The melt flow and fibre orientation were then studied using a computational approach for each of the nozzles. Papon et al. studied the effect of the nozzle geometry on thermoplastics (PLA) with carbon nanofibres (CNF) [40]. Three different shapes for the nozzle outlet were tested: circular, square and star-shaped. Figure 2.6 a) shows the nozzle geometries and their respective deposited filament shapes. Due to the Barus effect (also known as die swell effect), when the melted polymer goes out the nozzle, it expands along the edge

changing its shape [41]. Thus, the star-shaped nozzle with four vertices extruded a square filament. The square filament shape partly avoid one of the challenges of 3D printing, which is interfacial voids between printed filaments due to the cylindrical shape of the filaments. Another study demonstrated how rectangular nozzles produced printed parts with better compactness and compressive strength than circular nozzles, in this case concrete was the printing material [42]. The compressive strength was tested in three different directions. In all tested directions, the compressive strength for the samples printed with the square nozzle was 10 N/mm^2 above the samples printed with the cylindrical nozzle due to an increased contact surface between layers. The nozzle geometry was also studied for CF reinforced PEEK [43]. Specifically, a custom-made nozzle shown in Figure 2.6 b) was developed to vary the outlet angle among 60º, 90º and 120º keeping constant the nozzle diameter at 0.4 mm. In this study, it was found that increasing the exit angle leads to increased fibre breakage during the extrusion process. Therefore, a lower exit angle (60°) decreased the added damage to the fibres and improved the fibre orientation in the extrusion direction, which at the same time improved the mechanical properties.

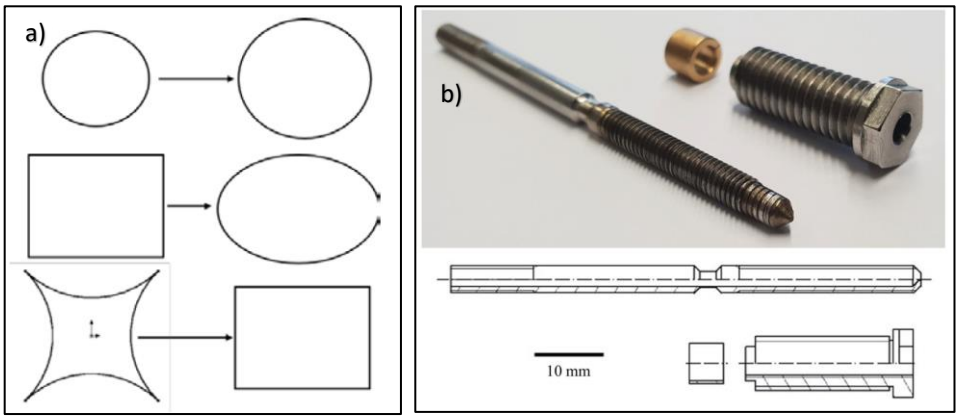

Figure 2.6: Examples of researched nozzles: a) Nozzle geometries with the respective deposited filament shape [40] b) Nozzle adapter with interchangeable custom-made nozzles [43].

2.5 3D printing in the aerospace field

2.5.1 Printing of high performance polymers for aerospace applications

The reduction of the fuel and energy consumption is one of the most researched challenges in the aerospace field. If the aviation sector was considered as fictitious country, it would take the 6th position in the most pollutant states by CO_2 emissions in 2015 [44]. AM appears to be a valid ally in dealing with the large amount of pollutant emissions. However, the aerospace industry is very demanding and all materials and technologies are subjected to high quality testing before they are used in production [6]. AM applications in the aerospace field are still very new and could be very diverse; they range from structural printed parts of satellites, fuel injector heads or even parts from rocket engines [45]. An example of a structural application is the CubeSat printed with ULTEM 9085 (80 g) which yielded a 50% weight reduction when compared to the original made with aluminium [46]. Structural and thermal simulations were performed successfully to verify the validity of PEI for this application. Another application was to use several HTPs for thermal protection systems [47]. PEEK, ULTEM 9085, ULTEM 1010 and PEKK were tested to study flammability and char yield. The flammability test results showed that PEKK had the highest char yield (64%) and ULTEM 9085 the lowest heat rate capacity (408 J/(g-K)), which means better flammability properties when compared to the other HTPs tested. Figure 2.7 shows real examples of 3D printed parts for the aircraft cabin. Figure 2.7 a) is an air grill printed for the 747 cockpit ventilation duct that presented a reduction in the manufacturing and maintenance costs. Figure 2.7 b) shows a 3D printed spacer panel for the Finnair's A320 that was optimised to have a weight reduction of 15 % [48].

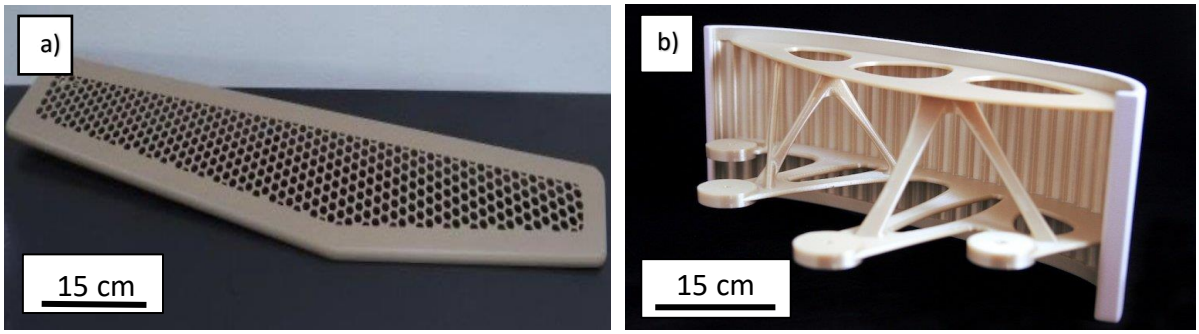

Figure 2.7: 3D printed parts for the aircraft cabin made with flame-retardant approved HTPs: a) air grill for a 747 cockpit ventilation duct and b) spacer panel for the Finnair's A320 [48].

2.5.2 3D printing of sandwich panels for aerospace applications

Sandwich panel structures are built with two skins, one on top and one on bottom and a low density/infill core for which several geometries exist. Table 2.3 shows the main core geometries used in sandwich panels. They are divided between evenly spread (honeycomb, tube or rectangular core) and longitudinally oriented (bulk, corrugated, tubular or frame core) [49]-[50]. Table 2.3 also shows the geometric parameters for the repetitive pattern of honeycomb structures that are crucial for the mechanical properties of the sandwich panels. Due to the core geometrical characteristics, these structures show a high strength to weight ratio, resistance to bending or stiffness and resistance to fracture [51].

Table 2.3: Types of core geometries of evenly spread and longitudinally oriented sandwich panels and geometric parameters for the pattern of the honeycomb sandwich structure [49].

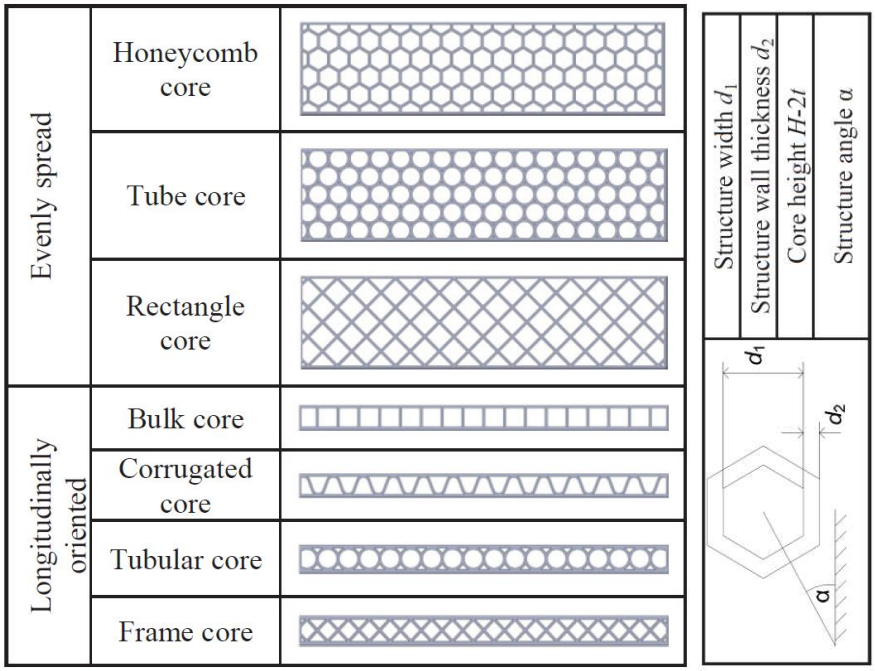

Several sandwich panels' parameters were studied with ULTEM 9085: the core geometry, building direction, structure width, structure wall thickness and top layer thickness [49]. The bending properties were evaluated using the ASTM C393 4-point bending test standard. The bending stress for each of the parameters was divided by the specimen mass to obtain the specific bending stress. The "frame geometry" was the best for the laterally printed specimens, but for the flat printed specimens, the "bulk core" had the best specific bending stress. In

addition, the lateral construction direction showed better absolute bending properties, but the flat printed specimens had slightly better properties for the specific bending values.

Furthermore, large structure widths and small structure wall thicknesses seemed to reduce the weight and they were the best choices for the specific properties. Large values of the top layer thickness also improved the strength properties.

In addition to the mechanical properties of the sandwich panels, dimensional accuracy was also studied. Zhai et al. published recently a work with ULTEM 1000 honeycomb sandwich panels [52]. In this study, the accuracy was measured by the relative accuracy (δ_R) and the absolute accuracy (δ_A) of the sandwich panels with the equations (2) and (3).

$$\delta_R = \left| \frac{Size\ of\ CAD\ model - Size\ of\ printed\ part}{Size\ of\ CAD\ model} * 100\ \% \right| \quad (2)$$

$$\delta_A = \left| \frac{Size\ of\ printed\ part - Average\ size\ of\ printed\ part}{Size\ of\ printed\ part} * 100\ \% \right| \quad (3)$$

The dimensional accuracy was measured with the mentioned equations in the height direction and in the thickness direction of each cell, to compare the external and the internal accuracy of the printed parts. The accuracy values for the external height of the printed samples were 2% and 0.5% for the δ_R and the δ_A , respectively. In the case of the cell thickness the values were 10.5% and 1.8%, respectively, which means that the external accuracy of the sandwich panels was more accurate compared to the internal.

2.6 Characterization methods for FFF printed parts

2.6.1 Characterization methods

There are several techniques to measure and assess the 3D printing process that can be sorted in two main categories. Indirect methods are those that study the manufacturing environment (for example the printing temperatures variation or the real printing speed at each step of the printing) and direct methods analyze the printed part by physical observations of it (surface roughness, accuracy, adhesion between deposited layers, quality of the printed parts, etc.). They can operate ex-situ, analyzing the printed object after printing or in-situ, performing the observations during the printing process [53].

Scanning Electron Microscopy (SEM) analysis is applied as characterization method to understand the microstructure of a 3D printed part. It can be used for the study of material blends when these have several components and the different phases can be observed [54]. Jiang et al. used SEM to analyze how the raster angle and the nozzle temperature affected the morphology of the fractured surface of printed PEI [19]. SEM images showed the spacing and gaps between deposited layers at the fracture surface. Figure 2.8 a) and Figure 2.8 b) shows the SEM images for the samples printed at the lowest tested nozzle temperatures 350°C and 360°C, respectively. The weak mechanical properties obtained with the lowest printing temperatures were closely related to the numerous holes that appear in the images. Figure 2.8 c) and Figure 2.8 d) show the SEM images for the nozzle temperatures 370°C and 380°C, respectively. The number and size of holes was clearly reduced for the sample printed at 370°C, showing a good coalescence between filaments, which is directly related to an improvement of the mechanical properties.

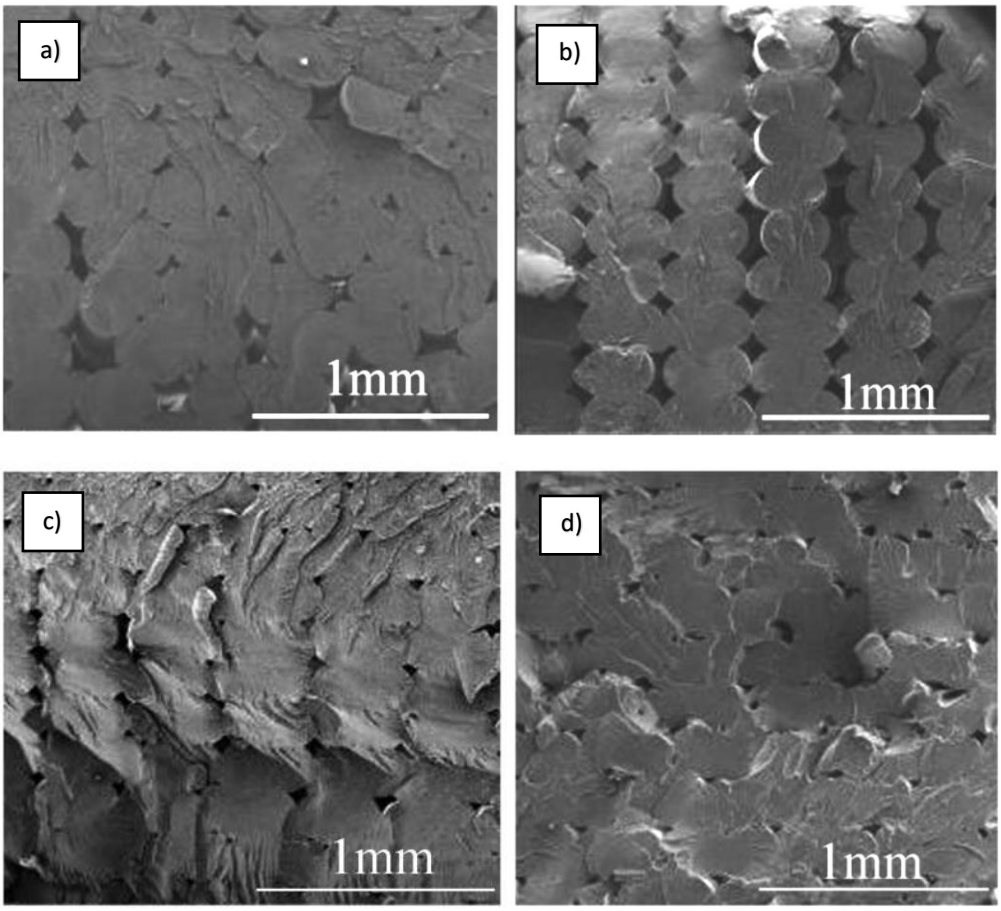

Figure 2.8: SEM images of FFF samples printed wih PEI at a 0° raster angle and nozzle temperatures : a) 350°C, b) 360°C, c) 370°C and d) 380°C [16].

X-Ray microtomography, also known as micro-CT is another method of micro-structure characterization for printed parts. The distribution of the carbon fibres in 3D printed PEEK was studied by micro-CT technology [55]. The results showed that the feedstock filament which contained 20 wt.% of CF presented an inner cylinder with lower content of fibres (represented by red) and higher content of PEEK (represented by blue), when compared to the outer part of the filament.

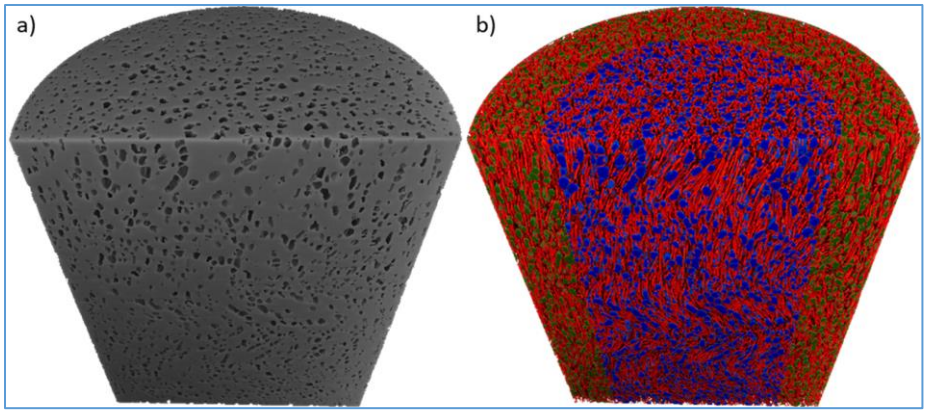

Figure 2.9: Micro-CT image of feedstock filament of carbon fibre reinforced PEEK: a) an homogeneous void distribution where the reinforced PEEK is in grey color and b) and an inhomogeneous distribution of the fibres in red color mainly located in the external part of the filament, PEEK is represented by blue in the internal cylinder and by green in the external part of the filament [55].

Figure 2.9 a) shows the homogeneous distribution of the voids in the filament. Figure 2.9 b) shows the different fibre distribution between the center of the filament (with less fibres) and the external part or it. When the reinforced PEEK was printed, the content of voids remained similar to the feedstock (between 16% and 22%). The minimum content of voids in the printed filaments appeared in the bottom half near to the printing build plate. Micro-CT can also be used as metrology tool like in the study performed by Gapiński et al. [56]. In this study, they used metrology CT to asses dimensions in part geometry and analyze the internal geometry.

2.6.2 Characterization of printed parts by offline OCT

Optical Coherence Tomography (OCT) is a non-destructive imaging technique mostly used in medical fields such as ophthalmology, cardiology or oncology. OCT performs cross-sectional and three-dimensional imaging with high resolution (1–15 mm) of internal geometries in biological tissues. This characterization method performs the measurements using the magnitude and the echoes time delay of backscattered light. In recent years, this new technology has been applied in engineering and, very recently, in 3D printing [57]-[58]. Hu et al. analyzed the 3D resolution of spectral domain OCT by 3D printing a test target and comparing the measurements with optical microscope for the lateral resolution and surface probe profiler for the axial resolution [59]. Lee et al. developed an algorithm to study the roughness of 3D printed dental crowns fabricated by SLM method [60]. The dental crown samples were printed with different build direction angles

(0°, 45°, and 90°) and different hatching methods (one-way, cross, and counter-clockwise). The optimal hatching method and construction direction could be determined by OCT.

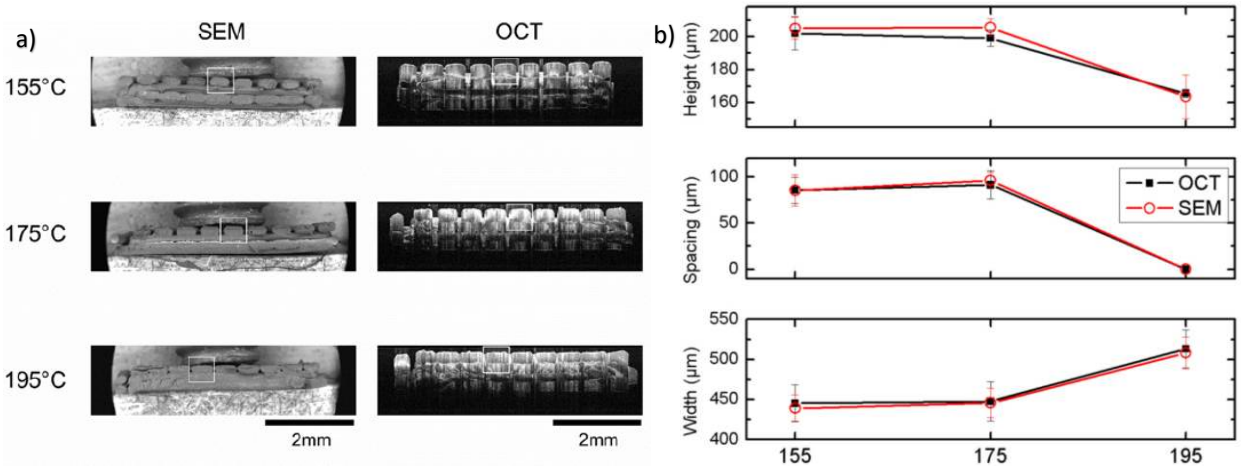

Figure 2.10: Measurement comparison of an FFF printed part with PLA between OCT and SEM at different printing temperatures. a) shows the SEM and OCT images obtained the printed parts at different printing temperatures. b) shows the plots for filament height, spacing and width of printed roads measured by both analysis techniques [61].

OCT images were compared to SEM morphologies of an FFF printed part [61]. The OCT images have shown the influence of the nozzle temperature on the layer deposition geometry. Figure 2.10 a) shows in a comparative way, images obtained from SEM and OCT of printed parts that were used to calculate the plots for filament height, spacing and width of the printed filaments at three different printing temperatures (155°C, 175°C and 195°C). Figure 2.10 b) shows that the deposited layer width measurements obtained by OCT and SEM were respectively 448 µm ± 24 µm and 446 µm ± 18 µm. Very similar results were obtained for filament height and spacing between filaments. Thus, OCT proved to be a valid technology to analyse the printed parts. Table 2.4 summarises the studies related to offline OCT applied to AM technologies. These works perform a surface evaluation of the printed parts with SD-OCT or SS-OCT.

Table 2.4: Summary of works related to OCT applied to AM

Resol. (µm)	Type	Inspection	3D printing	Material	Object of study	Ref.
6.5	SD-OCT	Offline (part)	SLA	Photopolymer	Surface profilometry and comparison with optical microscope and surface probe.	[59]
16	SS-OCT	Offline, (part)	SLM	Chrome-cobalt	Surface measurements and algorithm developed.	[60]
6	SD-OCT	Offline, (part)	FFF	PLA	Nozzle temperature on filaments measures and comparison with SEM.	[61]

2.7 Conclusions of the literature review

The literature review highlighted important research gaps related to FFF technology and its productivity to print HTRPs:

- Limited studies exist concerning the use of ULTEM 1000/1010/1040 in FFF process. There is a clear need of optimizing the printing parameters for these advanced thermoplastic polymers and their composites. A lack of information exists on ULTEM 1040 used for FFF, this advanced thermoplastic was not yet used in a filament shape nor applied in FFF 3D printing of parts for applications such for aerospace interiors.

- The use of 3D printing on an industrial scale is still very limited due to its lack of productivity. The high productivity of AM, and in particular of FFF, is still at an early stage of development. There are only a few studies investigating the increase of FFF printing productivity through increasing the printing speed. There is little diversity in the nozzles and extruders used to date. In addition, there are only a few research works using high-flow extrusion systems, such as BAAM technologies.

- The offline characterization of the 3D printed parts and online monitoring of the FFF system still need to be developed to fully rely on FFF technology for high-performance applications. Micro-CT, SEM and mechanical characterization methods are already used to a large extent in the study of the 3D printed parts structure and performance. Online control monitoring systems for 3D printing are practically non-existent. The use of quality control monitoring using OCT (a recently applied technology in AM) can pose several logistical problems, as well as problems in processing the large amount of data obtained during an OCT monitoring.

CHAPTER 3 APPROACH AND CONTEXT OF THE RESEARCH WORK

3.1 Approach to the research work

The main objective of the project was to characterize 3D printed specimens by an open-source FFF technology using novel high-melting temperature composites based on PEI with reinforcements. The studies performed with PEEK shown in the literature review are more abundant due to the high properties of this material, when compared to other high temperature materials. Nevertheless, the high price of PEEK 3D printing spools means a considerable cost increase that limits the use of this material for some applications. The use of PEI in this project represents a reduction in material costs by half compared to PEEK. In addition, the important innate mechanical performance of PEI advanced polymers and their thermal resistance make them excellent choices for 3D printing of parts designated for high-operating temperature applications. Therefore, in this project, the high-performance thermoplastic PEI ULTEM 1000/1010/1040 (mainly the ULTEM 1040) grades were studied in FFF process with the purpose to apply them in the 3D printing of performant sandwich panels for aerospace applications.

The use in this project of the AON-M2 open-source 3D printer allowed a flexibility in fine-tuning the 3D printing parameters selection and modification of the printing process together with the slicing software Simplify3D. The initial objective was to perform printing trials with commercial materials to better understand the printing process and to characterize the printed samples. Two different commercial materials made of ULTEM 1010 were printed using the AON-M2, one was made of pure PEI and the other with 10 wt.% CF-reinforcement. The specimens were printed at three different printing speeds and they were mechanically tested following the ASTM standard. Then, the samples were characterized by SEM and micro-CT to study the external and internal structure and to observe the porosity of defects that could have an influence in the mechanical performance.

The LM2 colleague and Polytechnique PhD student used a micro-twin extruder to produce small material volumes of several formulations as a preliminary study, to start printing non-commercial materials. The 3D printing filaments were made of three ULTEM grades and 10 wt.% to 40 wt.%

of CF reinforcement. These filaments were used to print 15 x 15 x 15 mm^3 cubes to study the printing feasibility of the ULTEM grades and different percentages of reinforcement.

Finally, four spools of 3D printing filaments made of novel developed advanced composites with different percentages of reinforcements using recycled Carbon Fibres (rCF) and Thermal Black (TB) particles produced at NRC laboratory for 3DREAM project were printed in the AON-M2. The 3D printed specimens with the four spools of developed material were mechanically tested and analyzed by SEM and micro-CT. Therefore, in this work, well proven characterization methods, such as SEM, micro-CT or mechanical characterization were the first time applied on 3D printed specimens obtained with the new advanced composites based on PEI.

The mechanical properties of the printed specimens were characterized following the ASTM D638 for tensile properties. The printed samples were tested applying an increasing load and measuring the displacement to obtain the relation for the stress-strain curves. The adhesion between printed layers and the existing porosity were also observed using SEM and micro-CT characterization. The characterization methods applied helped to better understand the differences in the mechanical properties between different materials.

3.2 Context and coherence with the objectives of the 3DREAM project

The collaboration with the National Research Council of Canada allowed this project to be carried out as a part of the 3DREAM project. In the 3DREAM project the different collaborators share the same objective of advancing the FFF AM technology for the transportation sector. 3DREAM team from NRC assisted with their 3D printing expertise in the selection of 3D printing parameters for AON-M2 printer, with the slicing and preparation of stl files and by developing novel PEI advanced composites that were 3D printed and characterized as part of this master thesis.

The direct contact with some of the 3DREAM industrial partners involved in the project like AON3D helped to better understand the printing process and to apply their knowledge during the experimental process. In addition, some partners like AON3D provided assistance by repairing broken components on the AON-M2 3D printer.

CHAPTER 4 MATERIALS AND METHODS

4.1 Printing materials

4.1.1 Commercial materials

The commercial high temperature thermoplastic polymers printed in the AON-M2 were the ULTEM 1010 (PEI2010500NAT) called as “Com. Pure” in this project, and the reinforced ULTEM 1010 with 10 wt.% Carbon Fibres (PEI6010500BK0) called as “Com. Reinf.”, both from 3DXtech. All the filament spools used in this project came in the standard diameters of 1.75 mm.

4.1.2 Developed materials

On one hand, my colleague on this project produced HTRPs with different percentages of CF reinforcement using the DSM Xplore micro twin-screw extruder. Then, the filaments were extruded using a Filabot EX2 extruder in the LM2 lab. These “LM2 filaments” of CF reinforced PEI were printed in the LM2 customised 3D printer. Different grades of PEI (ULTEM 1000, 1010 and 1040) with different percentages of CF were used to produce these materials: 10 wt.%, 20 wt.%, 30 wt.% and 40 wt.%. In addition, custom-made filaments with 10 wt.% of polycarbonate and 30 wt.% of CF were also 3D printed to study if the addition of PC could improve the printability.

Advanced HTRPs, having high performance and low cost, were developed and fabricated by NRC team in 3DREAM project for performant applications. These “NRC filaments” made of ULTEM 1040 contained different combinations of rCF and TB particles (an eco-filler) and were printed in our lab using the AON-M2 printer. Four ULTEM 1040 formulations with 20 wt.% of reinforcements were used: 20 wt.% of rCF, 15-5 wt.% of rCF-TB, 10-10 wt.% of rCF-TB, 20 wt.% of TB. All the filaments were dried in a vacuum oven for 24h at 140°C before printing to remove any kind of moisture and improve the printing process.

4.2 3D printing process

4.2.1 3D printing machines

The first 3D printer used in this project was the LM2 customised 3D printer manufactured with the help of 3DBranches. The lab customised 3D printer, shown in Figure 4.1 a), was used to print custom-made LM2 filaments. The printing volume is 150 x 150 x 150 mm^3 and the motherboard used to control the printer was a Rumba model shown in Figure 4.1 b). The Rumba Board was set up to control the X/Y/Z axis movement and the heaters for the bed and extruder. The Rumba board had a USB connection to visualize the information during the printing in a computer through Simplify3D. In addition, the sensors to obtain the printing temperatures and movements were properly connected. The FFF printing head used in this printer was a Dyze Design extruder DyzeXtruder GT that was connected to a hot end able to reach 500°C to print high temperature materials. Two different nozzle diameters were used to print the custom-made materials: 0.4 and 0.6 mm. The printing bed had a maximum temperature of 70°C while printing. The customised 3D printer worked with an air-cooling system and did not have heat chamber. The lack of heat chamber could have a major influence in the mechanical properties of the printed parts. Thus, this 3D printer was used to study the printability by printing 15 mm side cubes of several PEI grades with different percentages of reinforcement and no mechanical tests were performed on the parts printed with it.

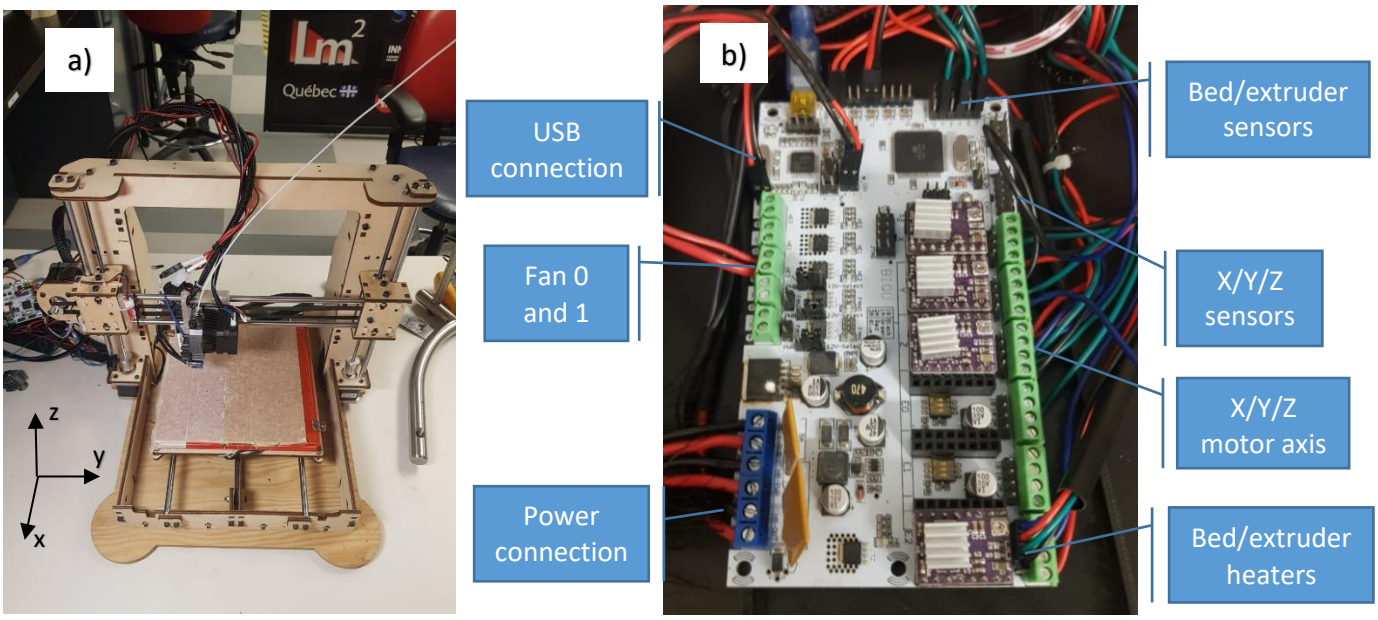

Figure 4.1: a) The LM2 customised 3D printer and b) the Rumba board used to control this 3D printer with the different connections for the axis movements, temperatures and powers.

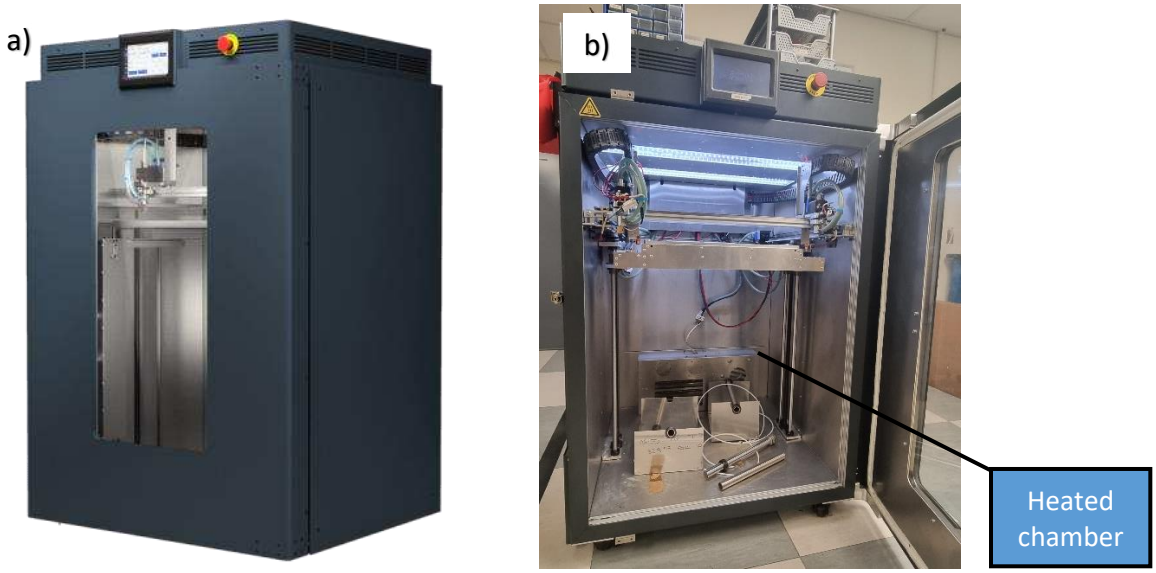

Figure 4.2: a) AON-M2 and b) interior view of the heat chamber

AON-M2, shown in Figure 4.2 a) from AON3D was also used to print the samples made of high temperature materials. First, Com. Pure and Com. Reinf. filaments were printed in the AON-M2. Then, the developed NRC filaments were printed in this 3D printer. The AON-M2 is an open-

source 3D printer that allowed the printing of high temperature material thanks to its heated chamber shown in Figure 4.2 b). The maximum printing temperature for the nozzle is 500°C. The maximum bed temperature is 200°C and the maximum heated chamber temperature is 130°C. The printing head contains a filament extruder manufactured by DyzeDesign, the DyzeXtruder GT (the used in the LM2 customised 3D printer). In addition, due to the high temperatures of the heating chamber, the printer has a liquid cooling system that uses Koolance LIQ-702 high performance liquid coolant. The nozzles used with this printer are the tungsten carbide nozzles from DyzeDesign (0.4 and 0.6 mm). The printing of composites with fibres produced from time to time an accumulation of material that reduced the outlet hole to the point of blocking it. Moreover, the passage at very high temperatures of composites containing up to 40 wt.% CF through this nozzle also had as effect the abrasion on the interior of the nozzle. In this way, the internal diameter of 0.4 mm became larger turning into one a 1-mm hole. To avoid these issues, a continuous check of the nozzles has to be done to assure a correct 3D printing of specimens. This common blockage phenomenon occurs mostly with small nozzles like the ones used in the project (0.4 mm). When the flow of material through the nozzle was not continuous, it was change by a new one with the same characteristics.

The AON-M2 has a printing bed made of PEI, which improves the adhesion of the printing part with high temperature materials like PEEK, or PEI. The dimensions of the printing volume are: 450 x 450 x 565 mm^3. The use of the glue Nano Polymer Adhesive from Vision Minner helped to improve the printing process with the AON-M2. The glue was used to increase adhesion to the printing surface. High temperature materials tend to warp when the parts are long and narrow. A thin layer of glue was spread with a brush on the printing bed already heated at the corresponding printing temperature. The glue manufacturer recommends waiting one minute for the glue to dry before starting the print.

Troubleshooting the AON-M2

The fact that AON-M2 is an open-source 3D printer designed for printing HTPs and HTRPs makes this printer very interesting for research. The level of modification and adjustment of the printing process is very detailed with tenths of printing parameters available to modify the building

process. This not only allows to achieve a high precision and quality by adjusting it to the shapes of the parts to be printed, but also an ability to adapt the printing process to different types of industrial or developed materials. However, the open-source technology hinders the printing process to some extent to the point that printing with machines like the AON-M2 can be a challenge. The high level of precision of this printer means that the slightest hardware or software error can stop the printing process or even produce a major problem that may require the hand of a specialist technician. The number of bugs, both software and hardware, encountered during the development of this project was considerable. This led to delays in fabrication of the samples.

Some of the encountered problems were related to the hardware of the printing head. For example, the high temperatures in the chamber erode and worsen the properties of crucial parts over time. The different sensors for the motion and for the temperatures like the thermistor of the printing head of the AON-M2 had to be replaced periodically to assure the proper functioning of the printer. One of the major problems encountered in this project was the malfunction of the Programmable Logic Controller (PLC), which produced an erroneous sending of signal to the heater cartridge of the heat end. In a similar way as with other 3D printers, periodic maintenance was required to verify the good condition of the 2 shafts that raise and lower the printing surface as well as the belts that connect the motors to the shafts.

AON-M2 3D printer, made by the Montreal company AON3D, still remains one of the best 3D printer worldwide from its category, a very innovative one, with the highest printing volume, having a unique heated chamber up to 135°C, and, the most important, it is functioning in an open-source mode for the software and the composites filaments. AON-M2 printer is the most appropriate, and the sole one, to be used in this project for high-melting temperature composites filaments for aerospace applications. Industrial R&D project such as 3DREAM from NRC is in place also to advance the 3D printing process for AON-M2 printer. Moreover, AON3D company being a partner in the 3DREAM project is already working for the upgrade of their printer. 3DREAM project it is a 3-years project that will finish by the end-2024 when a new generation of AON3D printer will be launched.

4.2.2 3D printing parameters selection

The software Simplify 3D was used to slice and set the main printing parameters for each printed part. Some of the most common parameters to adapt for each material are the following: extrusion multiplier (rate at which the printer extrudes material), printing speed, printing temperatures, layer height and raster angle. Figure 4.3 shows an example of the printing parameters that can be modified in Simplify3D for the AON-M2, where the nozzle diameter is selected to 0.4 mm, the extrusion multiplier is 0.9 and the extrusion width is 0.4.

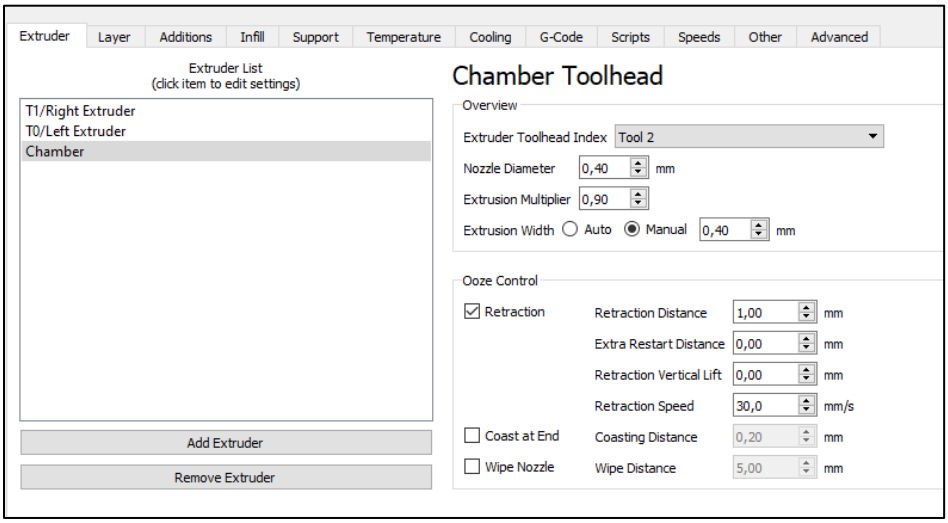

Figure 4.3: Example of the selection of the printing parameters in Simplify3D

Measurements of the printing speed in the AON-M2

A study of the printing speed in the AON-M2 was performed to analyze the actual printing speed with respect to theoretical speed selected in the slicer Simplify3D. A Python code was developed for this project to read the coordinates of a '.gcode' file and to record the distance travelled by the printhead for each printed segment to calculate the total length of printed filament. The equation (5) was used to calculate the average printing speed *V:*

$$V = \frac{\sum_{i=1}^{n} \sqrt[2]{(x_i - x_{i-1})^2 + (y_i - y_{i-1})^2}}{\Delta t} \quad (4)$$

where the total printed length for one layer was obtained using the coordinates *x* and *y* in space considering *n* different printed linear segments, and then the time *t* was measured.

3D Printing parameters

In summary, Table 4.1 shows the different commercial and advanced composites used in this project with different percentages of reinforcements with CF (or rCF) and TB. The printing parameters (nozzle diameter, printing speed, printing temperatures, layer height) used for each material are shown in the table. In addition, Table 4.1 shows the sample type and the characterization method used to study the samples.

Table 4.1 : Commercial filaments and developed advanced composites with different wt.% of reinforcements and with their respective printing parameters: nozzle diameter, printing speed, nozzle temperature, bed temperature, chamber temperature and layer height.

		Commercial filaments		Custom developed filaments		
Name		Com. Pure	Com. Reinf.	LM2 filaments		NRC filaments
Producer		3DXtech	3DXtech	LM2		NRC
ULTEM grade		ULTEM 1010	ULTEM 1010	ULTEM 1000, 1010 and 1040		ULTEM 1040
Reinforcement		-	10%CF	10%CF, 20%CF	30%CF, 40%CF	20%rCF, 20%TB, 15%rCF-5%TB, 10%rCF-10%TB
Printer used		AON-M2	AON-M2	LM2 Printer	LM2 Printer	AON-M2
Nozzle (mm)		0.6	0.6	0.4	0.6	0.4
Printing Speed (mm/s)		20, 40, 60	20, 40, 60	20		20
Nozzle *T* (°C)		370	400	400		400
Bed *T* (°C)		130	130	70		170
Chamber *T* (°C)		120	120	-		120
Layer height (mm)		0.2	0.2	0.2		0.3
Sample type		dogbone	dogbone	cube	cube	dogbone
Character.	SEM	✓	✓	-	-	✓
	Micro-CT	✓	✓	-	-	✓
	Tensile	✓ type 1	✓ type 1	-	-	✓ type 1

The first commercial filament 3D printed in this work was the Com. Pure made of Ultem 1010. Dogbones were printed with the raster angle +45/-45°. The use of this raster angle is explained by the fact that the stresses applied to the sample were not aligned with the filaments. Therefore,

the mechanical results obtained with +45/-45° raster angle were more conservative. The nozzle temperature was 370°C, the bed temperature 130°C and the chamber temperature 120°C. The nozzle diameter was 0.6 mm and the layer height was also kept constant at 0.2 mm. Three different printing speeds (20, 40 and 60 mm/s) were studied to analyze the change in the mechanical properties.

Secondly, Com. Reinf. filament made from the composites ULTEM 1010 / 10 % CF was used to print tensile specimens (dogbones) using the same printing directions. The nozzle used was 0.6 mm, the nozzle temperature was 400°C, the bed temperature 130°C and chamber temperature 120°C. The printing speed was initially studied at three different settings: 20, 40 and 60 mm/s as for Com. Pure filaments. Since the mechanical results presented low values compared to the pure ULTEM results, two printing parameters were selected to try to improve them. Different values for the nozzle temperature and extrusion multiplier were tested at the printing speed of 40 mm/s. A higher nozzle temperature of 420°C was tested together with an increase of the extrusion multiplier from 1 to 1.1.

The developed materials used in this project were new printing materials and the printing parameters selected were based on the literature review and recommendations of the NRC team. The CF-reinforced LM2 filaments made of PEI were used to 3D print a 15 mm sided cube on the LM2 customised 3D printer. The printing parameters were 400°C nozzle temperature, 70°C bed temperature (limited by the Rumba board and the printing bed) and printing speed of 20 mm/s. The filaments with 10 wt.% and 20 wt.% of CF were printed with a 0.4 mm nozzle. For higher percentages of CF (30 wt.% and 40 wt.%), a 0.6 mm nozzle was required to prevent blockage and assure a good flow of the material through the nozzle.

The printing parameters used to print the developed NRC filaments made of rCF/TB reinforced advanced composites were printed following the NRC's 3D printing specialist recommendations. Tensile test samples were printed in the AON-M2 with a nozzle temperature of 400°C, a bed temperature of 170°C and the chamber temperature of 120°C. The printing speed was 20 mm/s and the nozzle had a diameter of 0.4 mm. The layer height used in this case was 0.3 mm the raster angles were +45/-45°. Figure 4.4 a) shows the entire dogbones with the top layer at 45° in

the software Simplify3D. In Figure 4.4 b), the raster angles with the addition of 2 external layers bordering the external part of the samples can be observed.

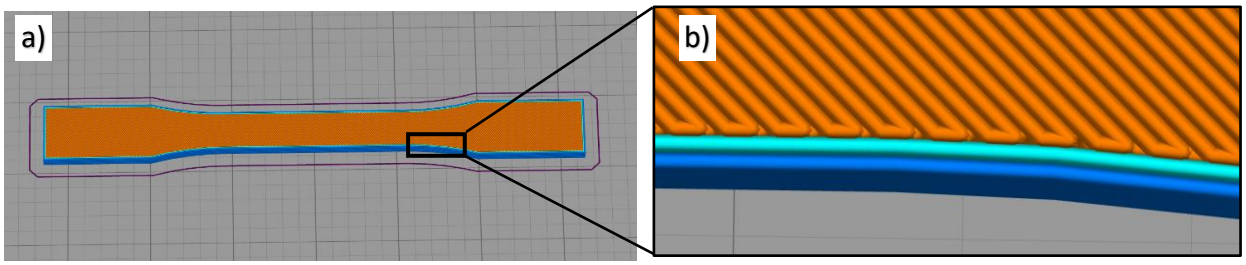

Figure 4.4: a) 3D Model of the ASTM D638 Type 1 dogbone in Simplify3D and b) zoom image of the 2 external layer (blue and green) and the top internal layer (orange) of the dogbone at 45° raster angle.

4.3 Characterization methods

4.3.1 Mechanical tests

The standard used to perform the tensile tests was the ASTM D638 Type 1 for the commercial materials and for the novel advanced composites developed by the NRC. For each selection of parameters, 5 dogbones were tested. For the case of the filaments produced with 20 wt.% TB only 3 samples were tested due to a major problem with the programmable logic controller of the AON-3D during the last printing tests.

The MTS Insight electromechanical testing machine was used to test the samples. Figure 4.5 shows the testing system used for the mechanical tests. The top crosshead was responsible for carrying out the movement at a rate of 5 mm/min as mentioned in the ASTM D638 standard and the load cell measured the force applied in each test until the sample breaks. The load cell used to test the samples was a 50 kN load cell. The specimens were fixed by two grips that are adjustable to the thickness of each sample and to assure the correct grip. The axial extensometer with 50 mm gage length from MTS was used to measure the elongation of the tested samples to obtain the strain/stress curve. The mechanical tests were performed at room temperature. Finally, the machine controller was used to adjust the height of the crosshead for each sample. MTS TWElite software was used to visualize the experiments in the computer and to select the testing parameters.

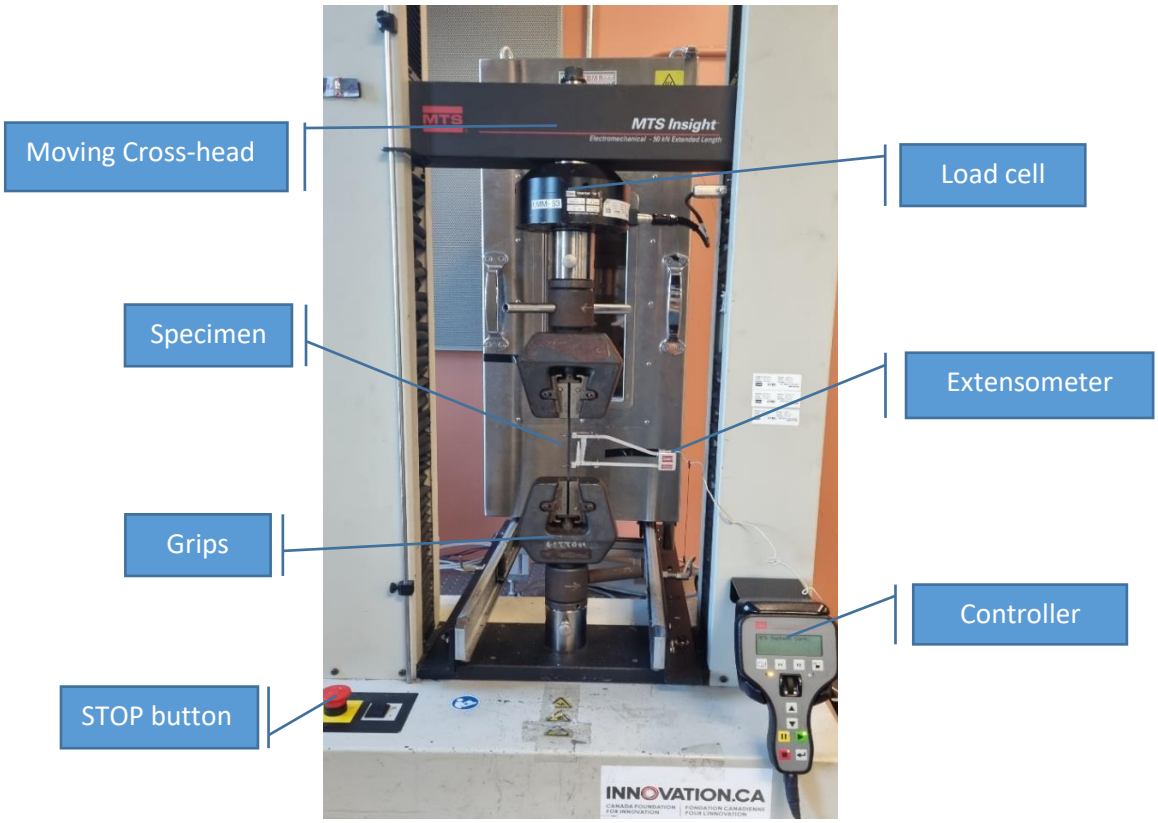

Figure 4.5: Example of a tensile test of PEI reinforced ASTM D638 Type 1 dogbone with 20 wt.% CF with the MTS Insight, the load cell and extensometer measuring the force and the deformation applied on the sample.

4.3.2 Optical microscopy

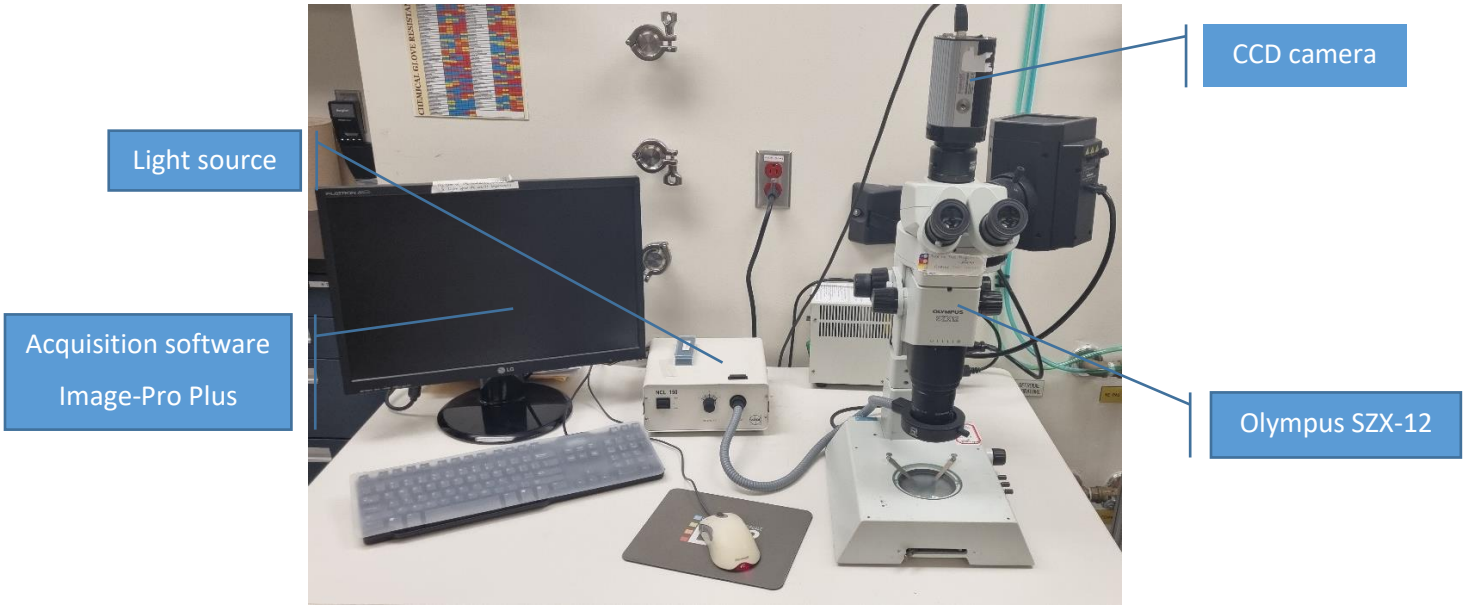

Figure 4.6: Optical microscope system with the Olympus SZX-12, the Evolution VF CCD camera and the external light source.

The printed samples were observed with the optical microscope Olympus SZX-12 showed in Figure 4.6, equipped with an Evolution VF CCD camera. The software ImagePro Plus was used to analyze the digital images of the microscope. An additional light source was used to light the samples during the observations. The optical microscope was mainly used to observe the external surface of the printed cubic samples with custom-made LM2 filaments. The external surface was analyzed using magnifications ranging from 7x to 25x.

4.3.3 Scanning Electron Microscopy (SEM)

SEM analysis was performed with the TM3030 Hitachi with a maximum resolution of 20 nm on several surfaces of the tensile samples printed with different commercial filaments (Com. Pure and Com. Reinf filaments) and developed NRC filaments. The SEM analysis were performed after the tensile tests to observe the fracture surfaces and the external top surfaces of the PEI and the rCF reinforced PEI samples. Figure 4.7 shows the SEM samples of the 4 types of developed NRC filaments (20 wt.% rCF, 15 wt.% rCF – 5 wt.% TB, 10 wt.% CF – 10 wt.% TB and 20 wt.% TB) set in a plate before the SEM analysis. Small portions (~1.5 cm long) were cut from the region of the fracture produced in the neck of the dogbones to study the top printed surface and the fracture surface of the Com. Pure, Com. Reinf. and NRC filaments.

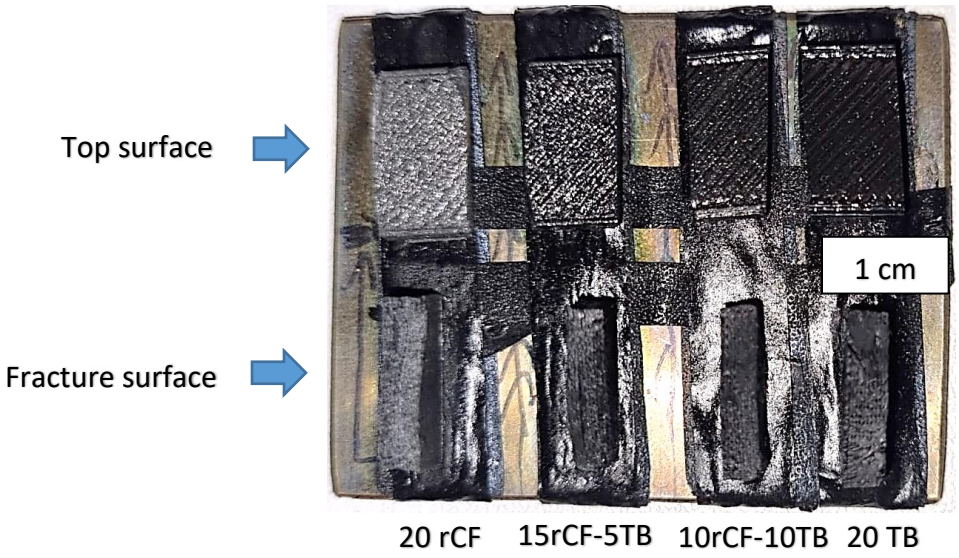

Figure 4.7: SEM samples of 4 different blends from the developed materials by the NRC. The 4 samples on top show the top printed surface and the 4 samples at the bottom show the fracture surface. From left to right : 20 wt.% rCF, 15 wt.% rCF – 5 wt.% TB, 10 wt.% CF – 10 wt.% TB and 20 wt.% TB.

4.3.4 Micro Computed Tomography (micro-CT)

Micro-CT analysis was performed to the tested samples made of Com. Pure, Com. Reinf. and NRC filaments. The micro-CT equipment used in the project was the Zeiss X-Radia Versa 520. Figure 4.8 shows the different components of the micro-CT equipment. An X-ray source of 40kV was used to analyse the samples with 1601 projection planes, thanks to the rotation platform where the specimen was placed. The fluorescent crystal received the X-rays and then the microscope objective produced a high-resolution scan with a pixel size of ~15 µm (lower than SEM). The obtained images allowed observing internal cross-sections of the printed samples to study the printing quality and the porosity. One sample for each of the formulations was studied with micro-CT before the tensile tests, to study the internal structure of the sample after printing and before being deformed during the tensile tests. Quantitative porosity results of the printed samples were obtained from the micro-CT images with the help of the software DragonFly.

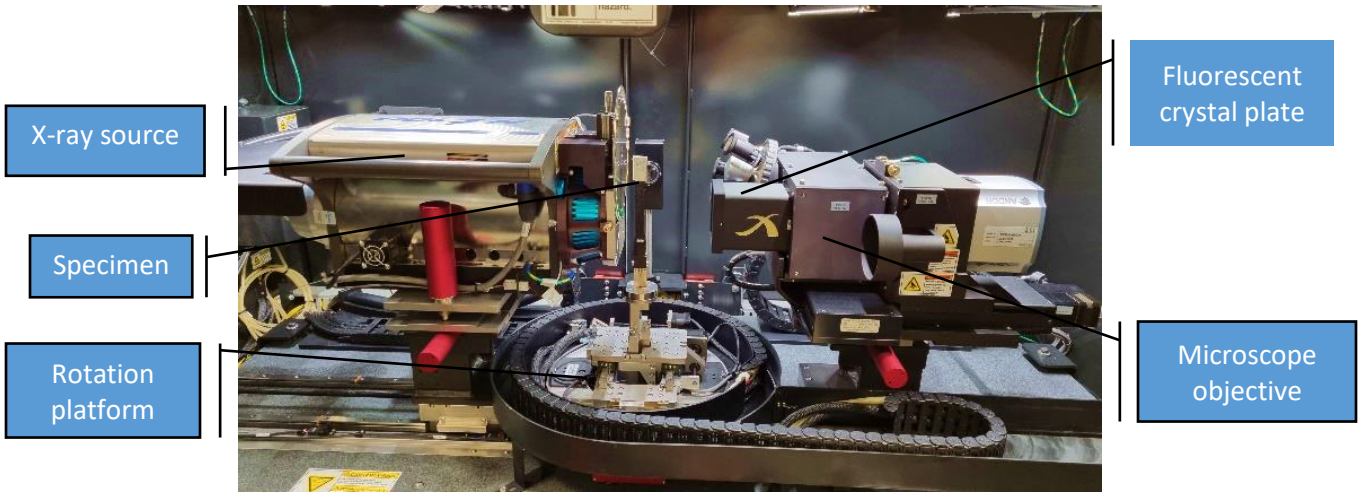

Figure 4.8: Interior of the micro-CT equipment Zeiss X-Radia Versa 520 used to study the printed samples

CHAPTER 5 EXPERIMENTAL RESULTS AND DISCUSSION

The first part of this Chapter 5 shows the results related to the printing tests using Com. Pure and Com. Reinf. filaments. The second part shows the printability results obtained with the LM2 filaments with different grades of ULTEM and percentages of CF. Finally, the results obtained with the 4 developed NRC filaments are shown.

5.1 3D printing of commercial filaments

5.1.1 Characterization results for printed parts made of Com. Pure filaments

Accuracy of the printing speed in the AON-M2

The accuracy of the printing speed was studied in the AON-M2 to analyse the difference between the theoretical printing speed selected in Simplify3D and the real printing speed when printing a dogbone specimen type 1 (ASTM D638). Figure 5.1 a) shows the relation between the calculated speed and the theoretical speed in the AON-M2. The reduction of the real speed (calculated speed) occurred mainly for high printing velocities achieving the maximum of 46% at the highest used printing speed that was tested (120 mm/s). The calculated speed was reduced with a logarithmic trend, which means that the reduction in the real printing speed was mainly related to the acceleration of the gantry system moving the printhead. Figure 5.1 b) shows the planar zig-zag pattern used to print each layer of the part, which caused numerous accelerations and decelerations that reduced the average printing speed in comparison with the theoretical speed. For the three printing speeds studied in the mechanical tests (20, 40 and 60 mm/s), the calculated speed reduction was 2, 7 and 17.2 %, respectively. It is important to consider that the calculated speed reductions depend on the printed shape and dimensions. A larger sample may have longer printing paths and therefore the real printing speed will be more similar to the theoretical speed.

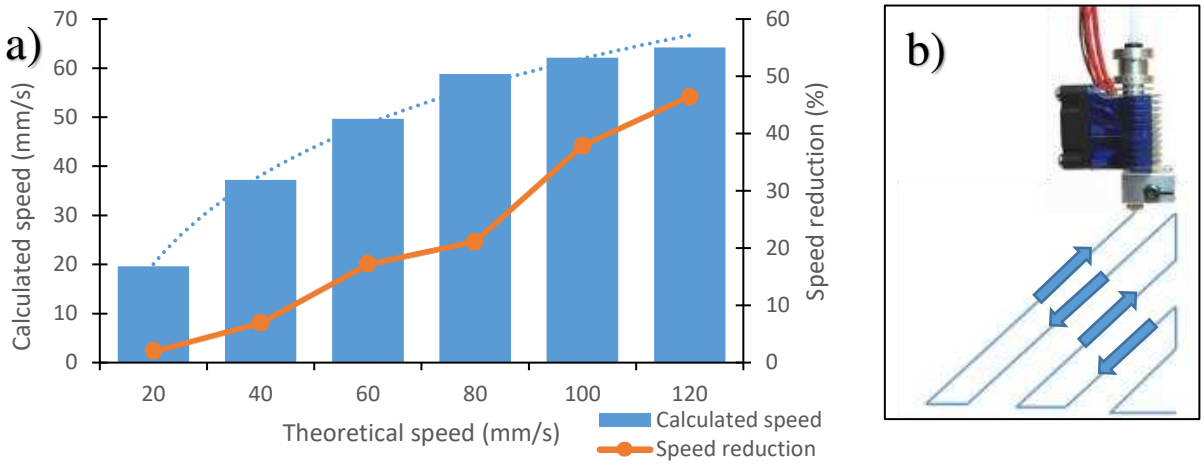

Figure 5.1: a) Plot of the calculated average speed (with logarithmic dotted trend line) and speed reduction percentage with respect to the theoretical printing speed for 1 printed layer of an ASTM D638 dogbone. b) Schematic of the zig-zag printhead movement during the printing process of a dogbone divided by printing linear segments that were printed following the directions of the arrows.

Mechanical tests of specimens printed with Com. Pure filaments

Figure 5.2 shows a representative stress-strain plot obtained for 5 different specimens made of Com. Pure filaments (Commercial pure Ultem 1010) at the printing speed of 20 mm/s. Stresses for the 5 tests show similar curves with a maximum of 67 MPa for test 3. The stress-strain curves for the other 2 printing speeds tested (40 mm/s and 60 mm/s) can be found in Appendix A. Figure 5.3 shows the Young's modulus for samples printed with Com. Pure filaments at three different printing speeds with the 95% confidence interval and the reference value from the Technical Data Sheet (TDS) of the material [62]. The histogram for the UTS at the three different printing speeds and the value from the TDS is shown in Figure 5.4. For the Young's modulus and the UTS, the best values were 2.85 GPa and 63.74 MPa, respectively, both obtained at the lowest printing speed (20 mm/s). The Young's modulus and UTS obtained with the printed samples were above the listed values (Young's modulus and UTS, respectively: 2.5 GPa and 56 MPa) by the commercial filaments manufacturer [62].

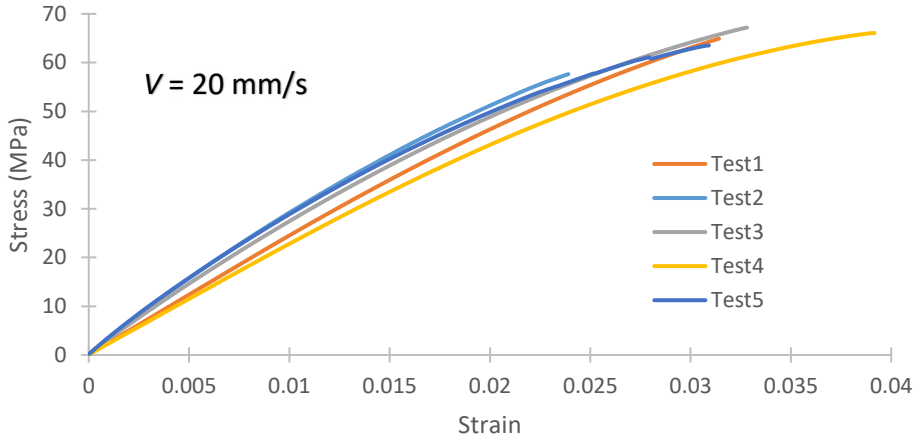

Figure 5.2: Stress-strain graph (ASTM D638) for the lowest printing speed tested (20 mm/s) with Com. Pure filaments printed with a 0.4 mm nozzle and with a nozzle temperature of 370°C.

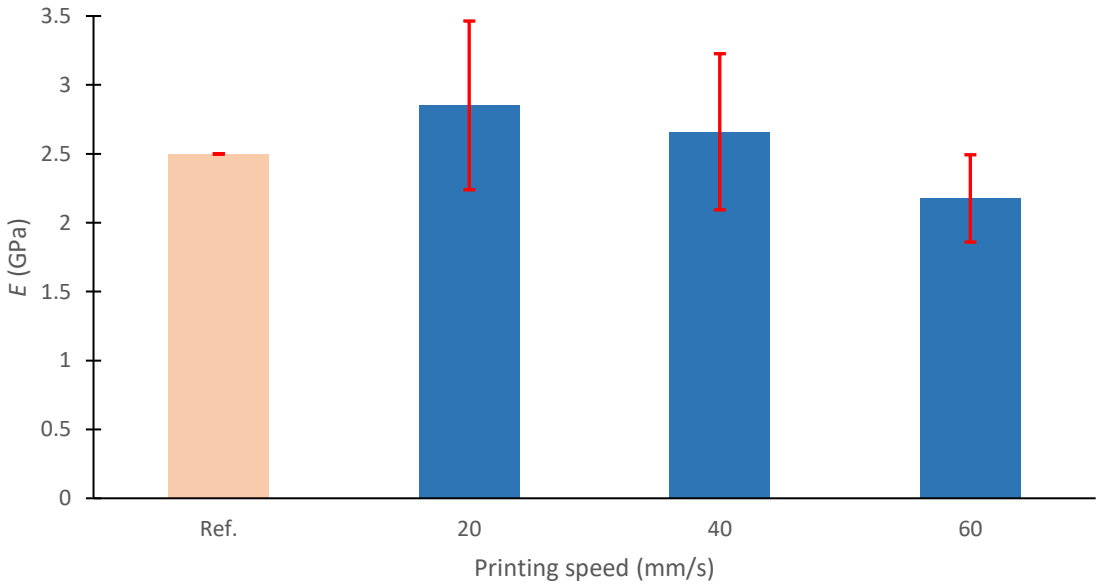

Figure 5.3: Young's modulus results of Com. Pure filaments from the TDS Ref [62] and for three different printing speeds (20, 40 and 60 mm/s) with 95% confidence interval.

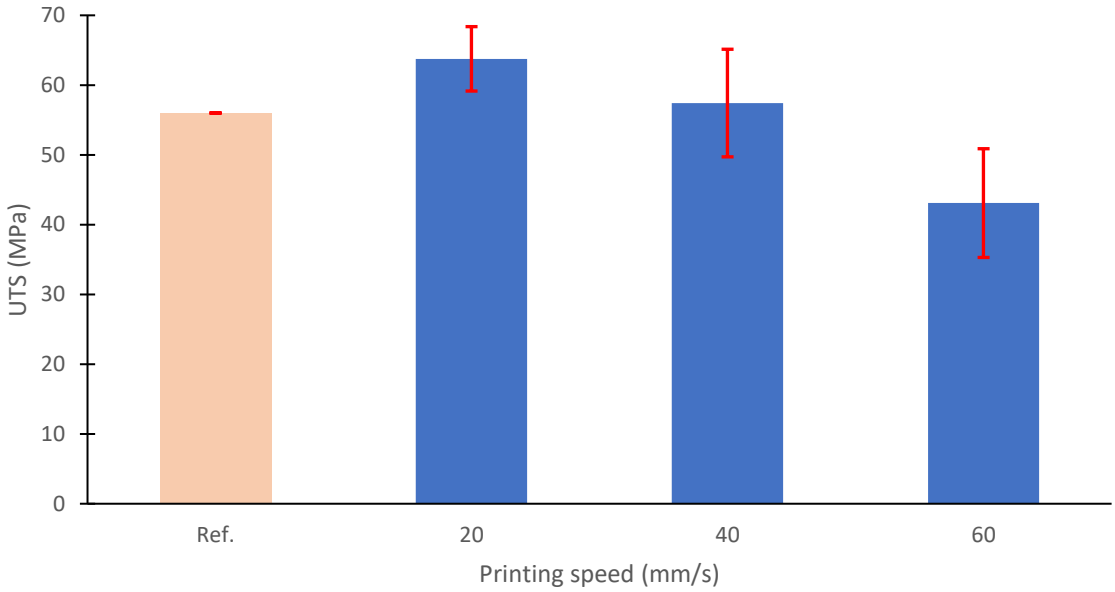

Figure 5.4: UTS values of Com. Pure filaments from the TDS Ref. [62] and for three different printing speeds (20, 40 and 60 mm/s) with 95% confidence interval.

Microstructure characterization of specimens printed with Com. Pure filaments

The dogbones 3D printed with Com. Pure filaments were characterized for their microstructures using SEM and micro-CT done on fractured surfaces resulted after the tensile tests. SEM images of the low, intermediate and high printing speed (20 mm/s, 40 mm/s and 60 mm/s) samples are shown in Figure 5.5. Figure 5.5 a) shows a broken tensile test sample with a black square that frames the region observed by SEM. The SEM images from the top surface of the fractured dogbones for the three printing speeds (Figure 5.5 b), c) and d), respectively) showed a reduction of the surface quality with the increase of the printing speed. The SEM image for samples printed at 20 mm/s showed a clear delimitation of the deposited layers but no large porosities were seen. For the samples printed at 60 mm/s, the SEM image show several 2 mm long porosities. Figure 5.6 a), b) and c) show the fractured surfaces for the specimens printed at 20, 40 and 60 mm/s, respectively. The fracture surface SEM images showed the interior part of the samples and the high degree of porosities. At 60 mm/s, the fracture surface showed larger holes, when compared to lower speeds. The porosities followed a pattern that can be shown clearly in the Figure 5.6 a), b) and c) by yellow circles for the three printing speeds; the rectilinear pattern formed by the

porosities appeared mainly in the crossing points between different layers that were deposited at +45/-45°. The decrease of mechanical properties with increasing speed can be possibly explained by the increase in number and dimensions of the porosities with the printing speed. Figure 5.6 c) show larger holes (~500 µm) compared to the porosities observed in the SEM images for the samples printed at 20 mm/s and 40 mm/s (~100 µm).

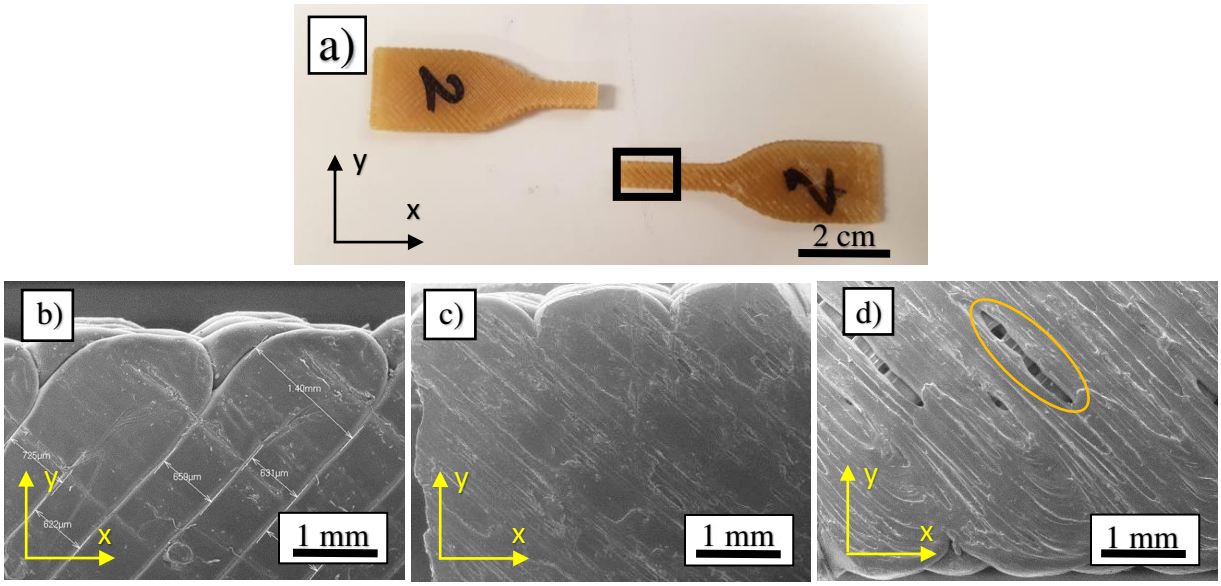

Figure 5.5: SEM images of the top surface of the Com. Pure printed dogbones at different printing speeds. a) example of broken sample showing the studied top region by a black square. SEM images for b)20mm/s, c) 40 mm/s and d) 60 mm/s using the AON-M2 printer.

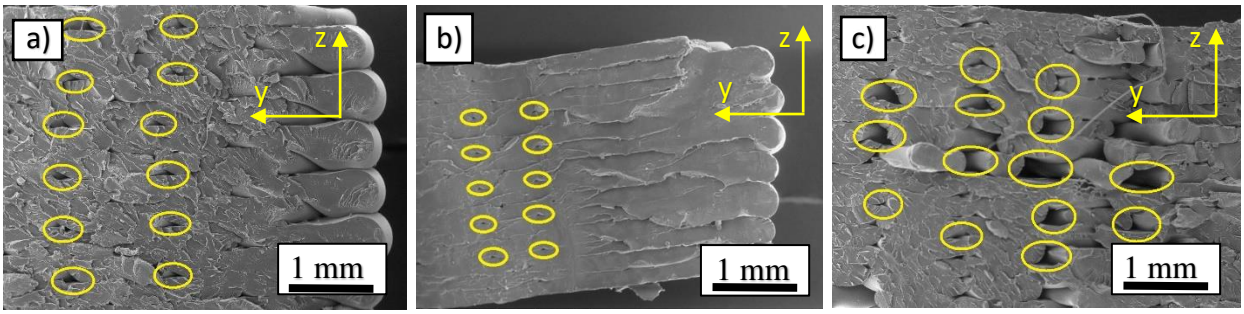

Figure 5.6: SEM images of the fractured surfaces of the Com. Pure printed dogbones at different printing speeds a) 20 mm/s, b) 40 mm/s and c) 60 mm/s. The yellow circles show the periodicity of the holes.

Figure 5.7 a) and b) show the micro-CT images of the cross sections of the central neck region of the printed dogbones at 20 mm/s and 60 mm/s, respectively. The internal cross section for printed sample at 20 mm/s showed porosities (smaller than 100 µm) due to the superposition of

each of the printed layers at raster angle 45/-45°. The percentage of porosities was ~7 %. The cross section for the printed sample at 60 mm/s showed larger porosities (~500 µm) due to the fact that the deposited layers were not touching together at high printing speeds. The percentage of porosity for this second samples was ~18 %. Therefore, the increase of printing speed (from 20 to 60 mm/s) created a 5x increase in the porosities dimensions. In addition, the sample printed at 60 mm/s presented the largest porosities in the central region, however the sides of the sample shown small internal porosities of ~100 µm. Finally, very rough edges were observed on the outer sidewalls of the printed sample at 60 mm/s.

Increasing the speed caused a stretching of the deposited layer that produces different heights along a deposited layer and internal porosities in the printed part. The irregularities caused bad adhesion between layers that reduced the mechanical properties. Furthermore, the increase in printing speeds may result in higher inaccuracy in filament deposition during the printing process.

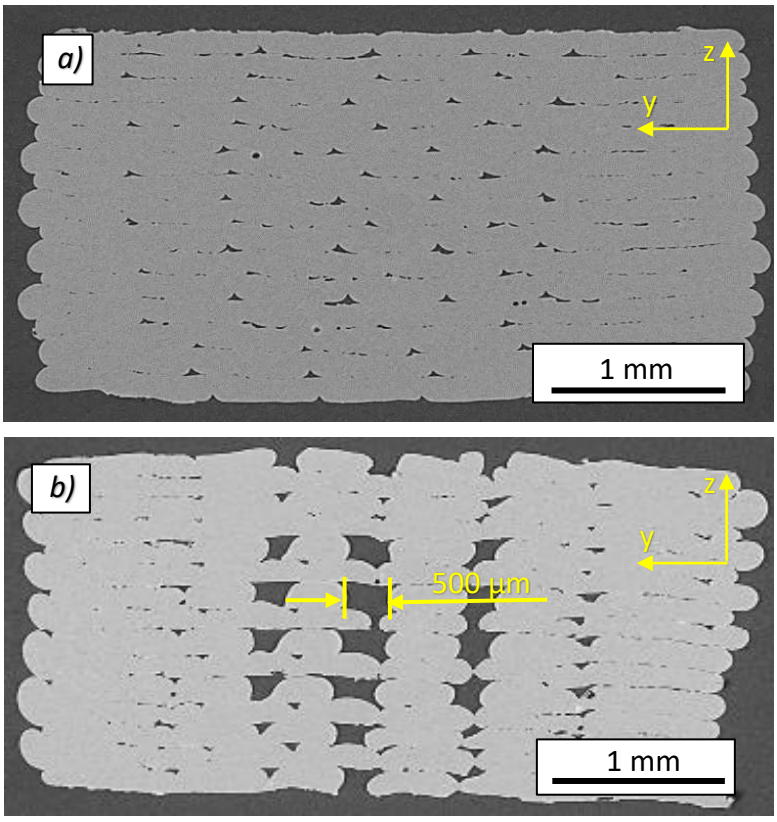

Figure 5.7: Micro-CT images of the neck cross section of the Com. Pure dogbones printed at a) 20 mm/s and b) 60 mm/s.

5.1.2 Characterization results for Com. Reinf. filaments

Mechanical tests of specimens printed with Com. Reinf. filaments

Figure 5.8 shows the stress-strain curve for the lowest printing speed tested (20 mm/s) in the AON-M2 for Com. Reinf. filaments (commercial CF reinforced ULTEM 1010). The curves obtained were similar for the three different printing speeds (20, 40 and 60 mm/s). The stress-strain curves for 40 mm/s and 60 mm/s are shown in the Appendix A. The results show similar curves for each of 5 tested specimens (dogbones). Figure 5.9 a) shows the Young's modulus obtained for the three printing speeds compared to the Ref. value from the TDS [63]. The highest value (1.88 GPa) was obtained for the lowest printing speed but the value obtained for the highest printing speed was the same value considering the 95% confidence interval (1.84 GPa). The mechanical results for Com. Reinf. samples showed low properties compared to the commercial data sheet (7.7 GPa). The UTS results in Figure 5.9 b) also show the lack of improvement in the UTS for all the printing speeds with the TDS Ref. values [63] and the considerable difference between them.

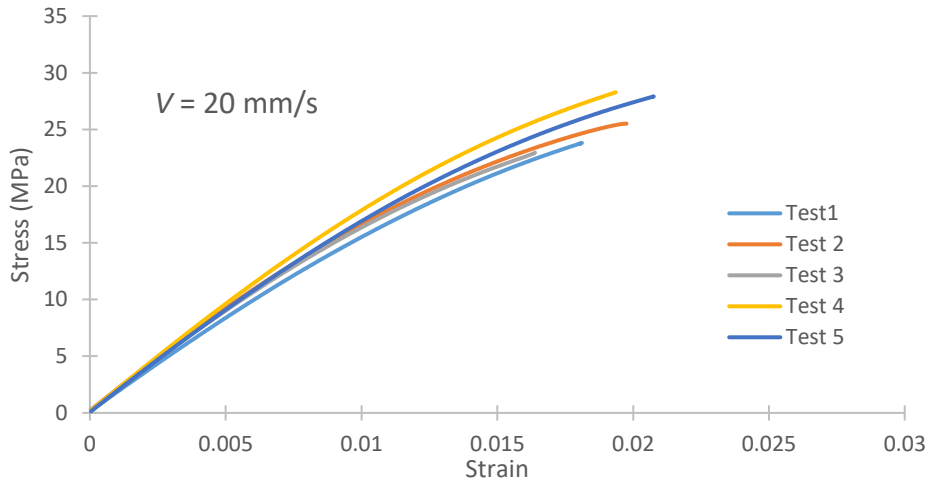

Figure 5.8 : Stress-strain graph (ASTM D638) for the lowest printing speed tested (20 mm/s) with Com. Reinf. filaments printed with a 0.4 mm nozzle and with a nozzle temperature of 400°C.

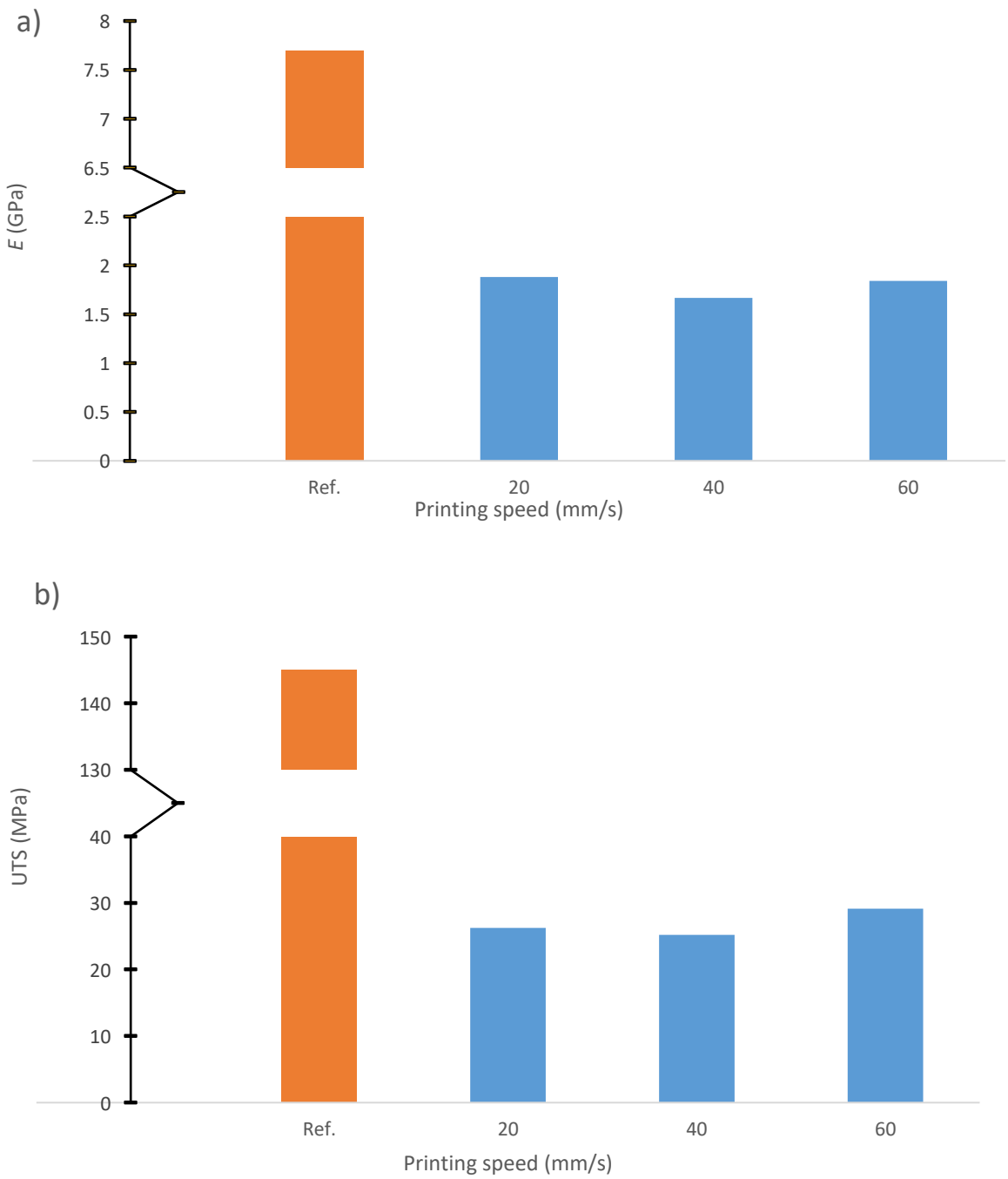

Figure 5.9: a) Young's modulus and b) UTS results of commercial Com. Reinf. filaments for three different printing speeds (20, 40 and 60 mm/s) with 95% confidence interval and the TDS Ref. values [63].

The tensile properties (Young's modulus and UTS) obtained with Com. Reinf. filaments shown weak properties compared to the material technical data sheet and to Com. Pure filaments. Therefore, an optimization of the printing parameters was required. The nozzle temperature and the extrusion multiplier were considered to try to optimize the weak mechanical properties. Figure 5.10 shows the stress-strain graph with the highest nozzle temperature (420°C) and highest extrusion multiplier (1.1) tested. The properties achieved for Com. Reinf. Filaments with the new printing parameters were a Young's modulus of 2.2 GPa and a UTS of 42 MPa. Increasing the nozzle temperature from 370°C to 420°C and the extrusion multiplier from 1.0 to 1.1 produced the best results so far. The increase of the flow rate of the printing material due to a larger extrusion multiplier and higher nozzle temperature may reduce the porosities and improve the adhesion between printed filaments.

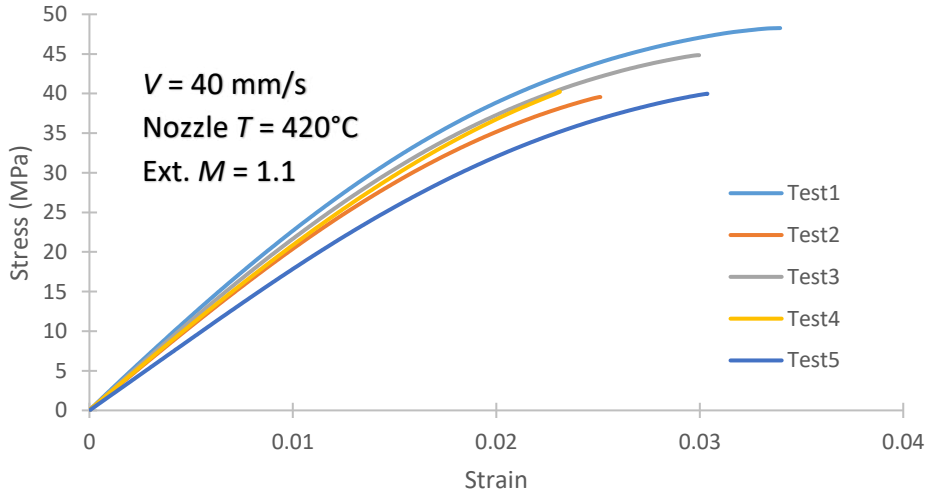

Figure 5.10: Tensile test (ASTM D638) results for Com. Reinf. Filaments with a nozzle temperature of 420°C and an extrusion multiplier of 1.1.

Microstructure characterization of specimens printed with Com. Reinf. filaments

The SEM images of the fractured surfaces and top surfaces were obtained for specimens printed with Com. Reinf. filaments (with an extrusion multiplier of 1 and a nozzle temperature of 400°C). Figure 5.11 a), b) and c) show that the large percentage of porosities appeared in the top surface

of the dogbones printed at 20 mm/s, 40 mm/s and 60 mm/s, respectively. However the deposited layers were not clearly delimited, which would be the sign of the bonding and adhesion between layers. The SEM images of the fractured surfaces are shown in Figure 5.11 d), e) and f) respectively, at increasing the printing speed. These images also show the large quantity of porosities in the 3D printed parts for the three printing speeds tested. Figure 5.12 presents the internal cross section of a sample printed at 40 mm/s (nozzle temperature and extrusion multiplier: 400°C and 1) obtained by micro-CT analysis. The micro-CT image of the cross section also showed high level of porosity (~25 %) of the 3D printed specimens. In addition, the external sidewalls presented very rough edges.

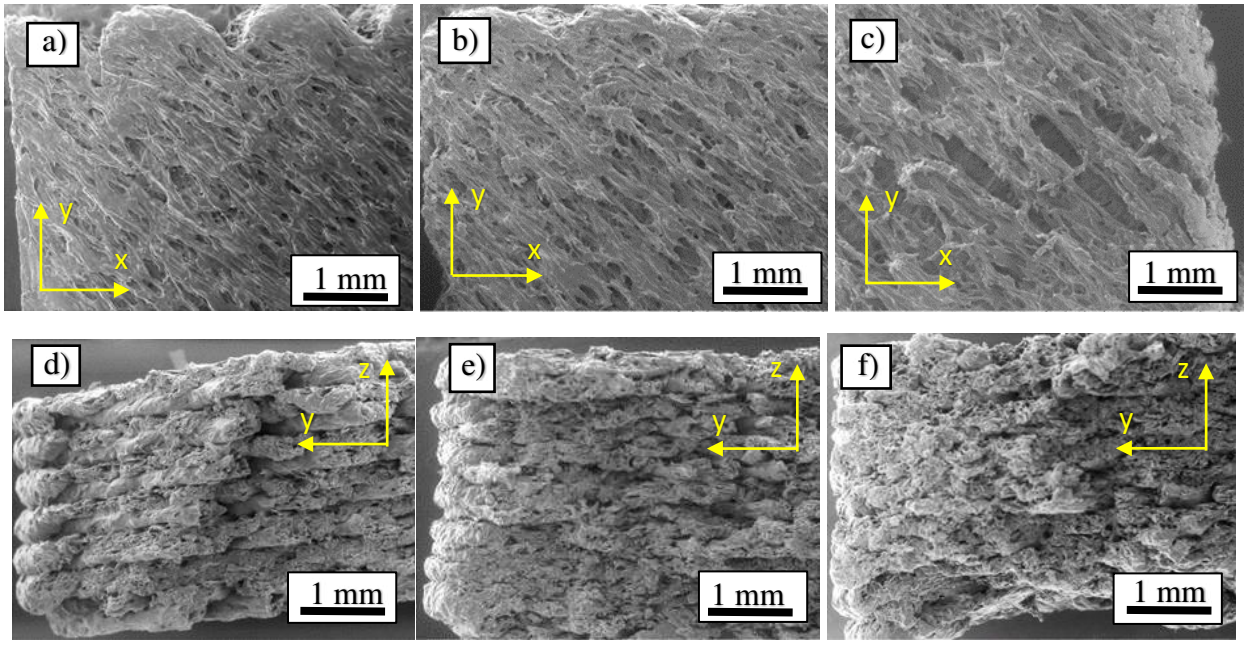

Figure 5.11: SEM image of the upper surface for the printed Com. Reinf. dogbones at a) 20 mm/s, b) 40mm/s and c) 60 mm/s. SEM images of the fractured surface of the of the printed Com. Reinf. dogbones at d) 20 mm/s, e) 40mm/s and f) 60 mm/s.

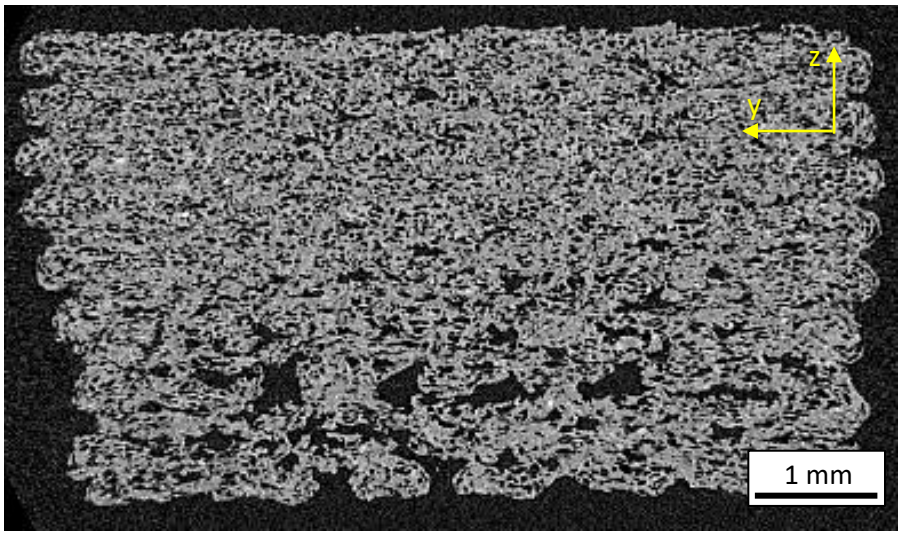

Figure 5.12: Micro-CT images showing the high degree of porosity for Com. Reinf. printed sample at 40 mm/s

5.1.3 Discussion of results obtained with Com. Pure and Com. Reinf. filaments

The mechanical results obtained for the 3D printed samples made of Com. Pure filaments present similar tensile properties to the technical data sheet provided by the manufacturer for this filament [62]. This similarity could be translated in an appropriate tailoring of the 3D printing parameters. In the case of Com. Pure filaments, the 3D printing tests were performed at three different printing speeds (i.e. 20, 40 and 60 mm/s) and clearly showed a reduction of the mechanical properties with the increase of the printing speed. For the lowest printing speed (20 mm/s) the Young's modulus was 2.85 GPa and the UTS was 63.74 MPa. For 40 mm/s and 60 mm/s, the reduction of the Young's modulus was of 7 % and 24 %, respectively. In the case of the UTS, a reduction of 33 % was obtained for the highest printing speed investigated of 60 mm/s. The SEM and micro-CT images were in accordance with the tensile results for Com. Pure printed dogbones because the level of porosity for the samples printed at 20 mm/s seemed to be significantly smaller (~7 %) compared to the samples 3D printed at 60 mm/s (~18 %).

In the case of the samples printed with the Com. Reinf. filaments, a clear need of optimization of the 3D printing parameters can be concluded because of the low tensile performance that was observed compared to the Ref. values of the TDS. When the 3D printed samples were studied

with SEM and micro-CT, the very high level of porosities (~25 %) that were observed seemed to be the cause for the low tensile performance for the three printing speeds tested (20, 40 and 60 mm/s). The technical problems with the AON-M2 during the 3D printing process together with the selection of some of the printing parameters (nozzle temperature and extrusion multiplier) were potentially related to the generation of porosities in the samples. The increase in nozzle temperature (420°C) and in extrusion multiplier (1.1) for the Com. Reinf. filaments helped to improve the mechanical properties with an increase of the Young's modulus of 14.5 %, achieving the maximum value of 2.2 GPa and a UTS of 42 MPa.

5.2 3D printing of developed materials

5.2.1 3D printing of LM2 filaments

Table 5.1 shows the different grades of PEI with different contents of CF that were used to 3D print the 15 x 15 x 15 mm^3 cube with the LM2 customised 3D printer. For the low percentages of CF (10 wt.% and 20 wt.%) a 0.4 mm nozzle was used to 3D print the samples and the print was performed successfully for all the ULTEM grades. However, when adding 30 wt.% and 40 wt.% of CF, a 0.6 mm nozzle was required to avoid clogging the nozzle. In addition, ULTEM 1040 was the only ULTEM grade able to print the cubes with 30 wt.% and 40 wt.% of CF. An attempt was made to print filaments made of pure PEI, but the lack of the printing chamber and the low bed temperature led to severe warping effects. Furthermore, an ULTEM composite with 10 wt.% of polycarbonate (PC) and 30 wt.% of CF was printed using a 0.6 mm nozzle. The flow through the nozzle increased and therefore the samples were easily printed, despite the high percentage of fibres.

*Table 5.1 : Printing tests (15 x 15 x 15 mm3 cube) performed with the LM2 filaments made of different ULTEM grades and wt.% of CF on the LM2 customised 3D printer. (*unfinished printed cube due to blockage of the nozzle)*

		CF wt.%			
		10	20	30	40
Polymer	ULTEM 1040	✓	✓	✓	✓*
	ULTEM 1010	✓	✓	✓*	-
	ULTEM 1000	✓*	✓	-	-
	ULTEM 1040 + 10 wt.% PC	-	-	✓	-
	ULTEM 1010 + 10 wt.% PC	-	-	✓	-
	ULTEM 1000 + 10 wt.% PC	-	-	✓	-

3D printed cubes and the respective optical microscope images for cubes' side surfaces for selected printing tests are shown in Figure 5.13. The roughness of the printed samples increased with the CF wt.%. For 10 wt.% CF (Figure 5.13 a) and Figure 5.13 b)) the surfaces presented good external quality. For 20 wt.% CF (Figure 5.13 c) and Figure 5.13 d)) the surfaces presented some small irregularities. At 30 wt.% CF, Figure 5.13 e) and Figure 5.13 f) show a clear increase in the surface roughness with gaps of ~1 mm. At 40 wt.% CF, Figure 5.13 g) and Figure 5.13 h), the irregular flow of the melted material through the nozzle (due to a clogging phenomenon) did not allow the 3D printing of the whole cube.

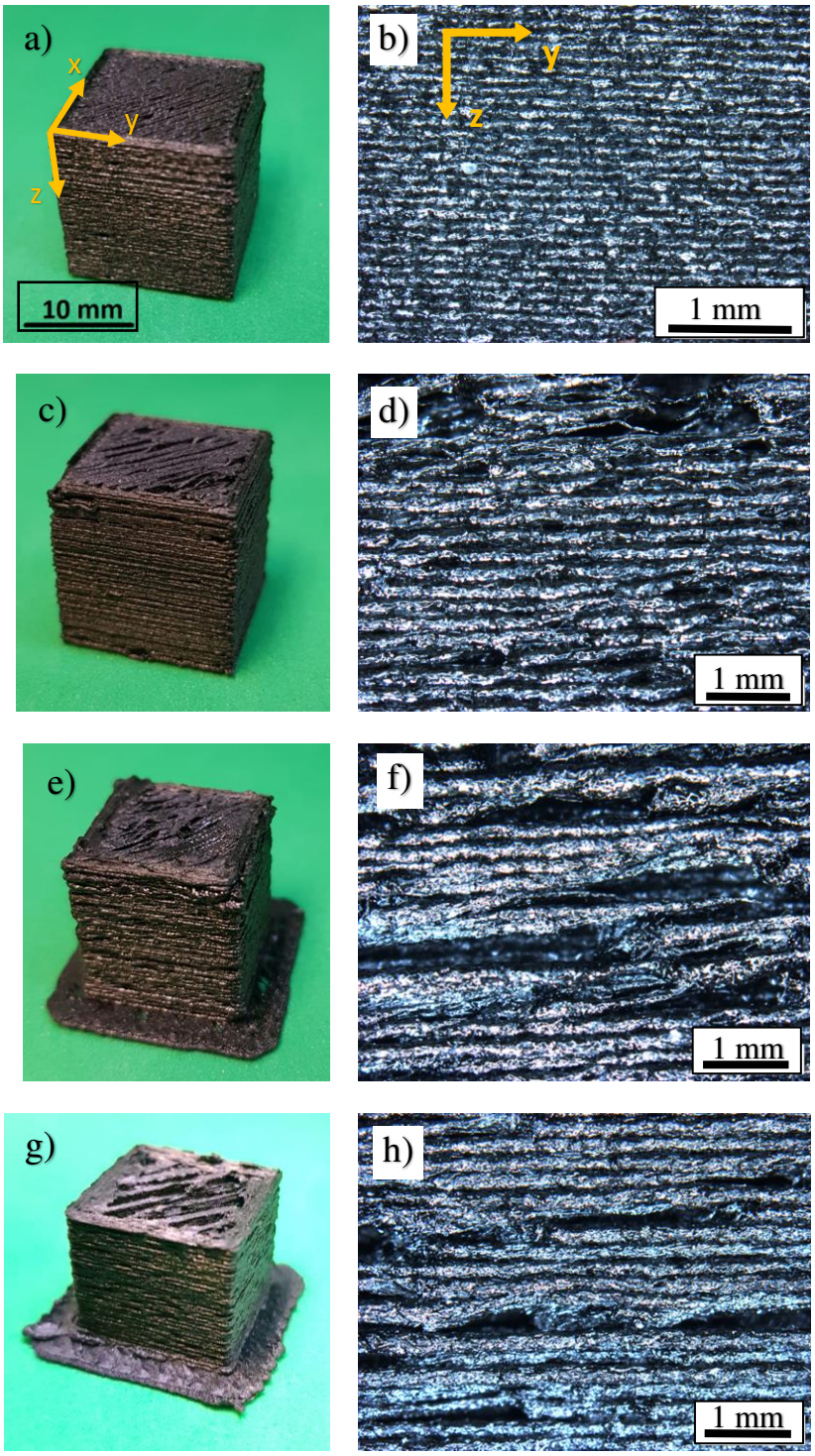

Figure 5.13: Printed 15 x 15 x 15 mm^3 cubes (theoretical size values) with LM2 filaments made of ULTEM 1040 and their optical microscope image from the lateral face respectively with: a) and b) 10 wt.% CF, c) and d) 20 wt.% CF, e) and f) 30 wt.% CF and, g) and h) 40 wt.% CF.

There is a clear improvement in material flow through the nozzle for composites containing lower concentrations of CF (10 wt.% and 20 wt.%) which results in better surface quality compared to higher concentrations of CF (30 wt.% and 40 wt.%). Furthermore, the addition of 10 wt.% of PC seemed to improve the printability of the materials at higher contents of CF (30 wt. %). The increase in printability could be related to the reduction of viscosity due to the high nozzle temperature (400°C), since PC is a material with a melting point of 288 – 316°C. However, another possible effect could occur is the partial degradation of PC at the high printing temperature.

The ULTEM 1040 grade appears to have the highest printability, as it was the only one that allowed printing all reinforced filaments with different percentages of CF. The 20 wt.% of reinforcements seemed to be the highest percentage that allowed printing samples with a 0.4 mm nozzle with a good external quality. Furthermore, the addition of PC or other fillers may help maintain good flow through the nozzle. Therefore, the next step in the project was to print in the AON-M2 3D printer the spools of developed NRC filaments, made of ULTEM 1040 and with a 20 wt.% of reinforcements.

5.2.2 3D printing of NRC filaments

The four different NRC filaments developed by the NRC's 3DREAM-team made of reinforced ULTEM 1040 were printed in the AON-M2 to build ASTM D638 Type 1 tensile test specimens. The printability and flow through the nozzle varies among the different formulations, however a common problem was that warping sometimes occurred when the last few layers were being printed. Figure 5.14 shows this warping phenomenon produced during the 3D printing of a dogbone with 20 wt.% rCF. The image shows how the right part of the sample detached from the printing surface.

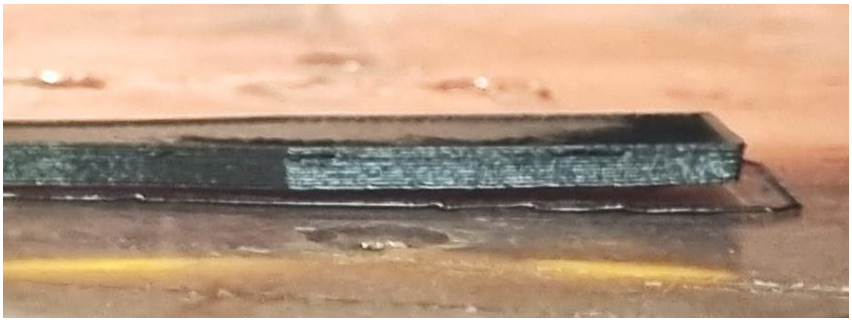

Figure 5.14: Warping phenomenon occurring during the 3D printing of a dogbone using the NRC filament reinforced with 20 wt.% rCF.

Figure 5.15 a) shows the 5 printed dogbones with 20 wt.% rCF, which is the formulation with the highest percentage of rCF. This first formulation presented a continuous flow through the nozzle with no blocking problems and the specimens presented homogeneous external surfaces. Figure 5.15 b) shows the printed specimens with 15 wt.% of rCF – 5 wt.% TB which presented a similar printing behaviour as for the first filaments with 20 wt.% of rCF. Figure 5.15 c) shows the printed samples with 10 wt.% of rCF – 10 wt.% TB. The warping effect produced for these samples was quite important and in order to avoid it the nozzle was moved 0.05 mm closer to the printing bed, using the AON-M2's touch screen, so the first layer of printed material was spread against the printing surface and the material adhered better. Finally, Figure 5.15 d) shows the printed specimens containing 20 wt.% TB. With this last formulation, the filament used to break during the 3D printing of the samples. Therefore, the printing process was paused every time it was necessary to change the filament.

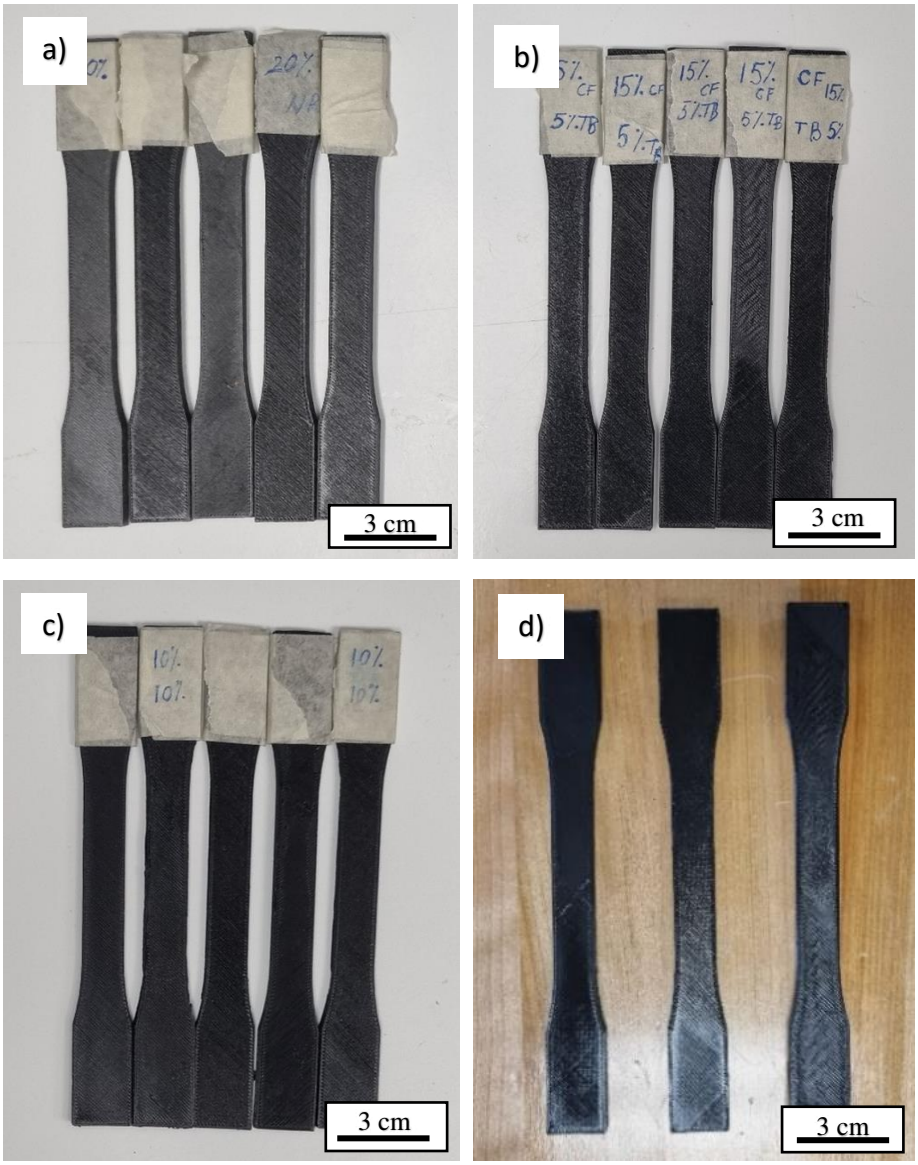

Figure 5.15: Tensile tests specimens (before testing) printed in the AON-M2 with the NRC filaments made of ULTEM 1040 with 4 different formulations: a) 20 wt.% rCF, b) 15 wt.% rCF – 5 wt.% TB, c) 10 wt.% rCF – 10 wt.% TB and d) 20 wt.% TB.

Mechanical tests of specimens printed with NRC filaments

Figure 5.16 shows the broken 3D printed specimens made of the NRC filaments after the tensile tests. Some of the printed dogbones broke in the middle of the neck. As mentioned by the ASTM D638 standard, the location of a fracture was a good indicator for the quality of the sample. The samples that broke on the middle of the neck had probably a more uniform internal structure than the ones that presented tensile ruptures at different places (possibly due to presences of

weak points). Figure 5.16 a) shows the samples printed with 20 wt.% rCF reinforcement which obtained 2 fractures in the middle of the neck, which is a good indicator. For the case of 15 wt.% rCF – 5 wt.% TB and 10 wt.% rCF – 10 wt.% TB, Figure 5.16 b) and Figure 5.16 c), respectively, show at least one clear fracture in the middle region of the dogbones. Finally, Figure 5.16 d) shows that the 3 samples printed with 20 wt.% TB reinforcement broke in the middle of the dogbone and one also in the grips.

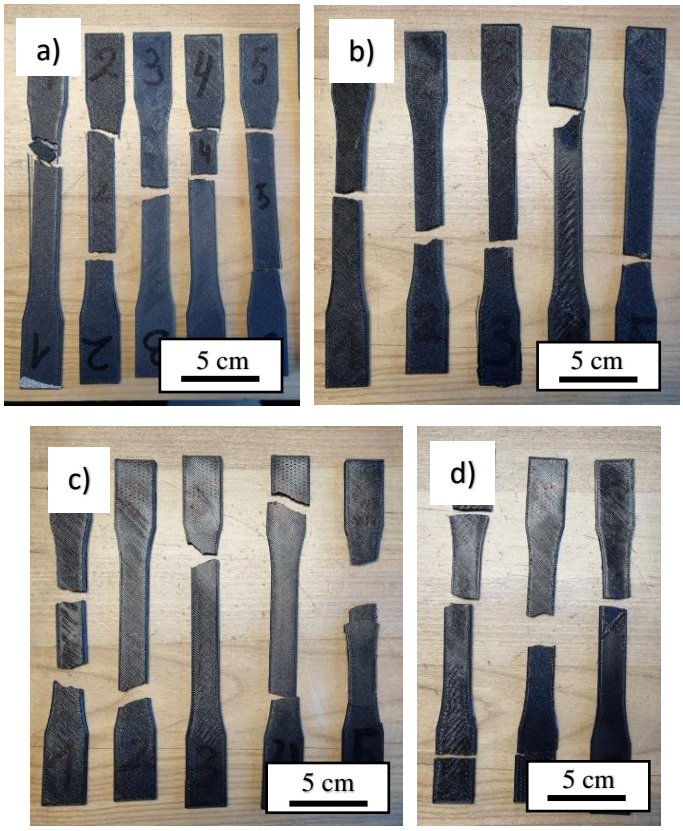

Figure 5.16: Tensile tests specimens (after testing) printed in the AON-M2 with the NRC filaments made of ULTEM 1040 with 4 different formulations: a) 20 wt.% rCF, b) 15 wt.% rCF – 5 wt.% TB, c) 10 wt.% rCF – 10 wt.% TB and d) 20 wt.% TB.

The strain/stress results obtained for each of the formulations are presented in Figure 5.17. Figure 5.17 a) shows the graph for the samples printed with 20 wt.% rCF which presents an initial linear range with some variations of the slope until the strain of 0.01 and a uniform elongation at break (~0.023). However, Figure 5.17 a) shows a considerable variation of the ultimate stress at break among the 5 specimens. Figure 5.17 b) shows the graph for the formulations with 15 wt.% rCF - 5 wt.% TB.

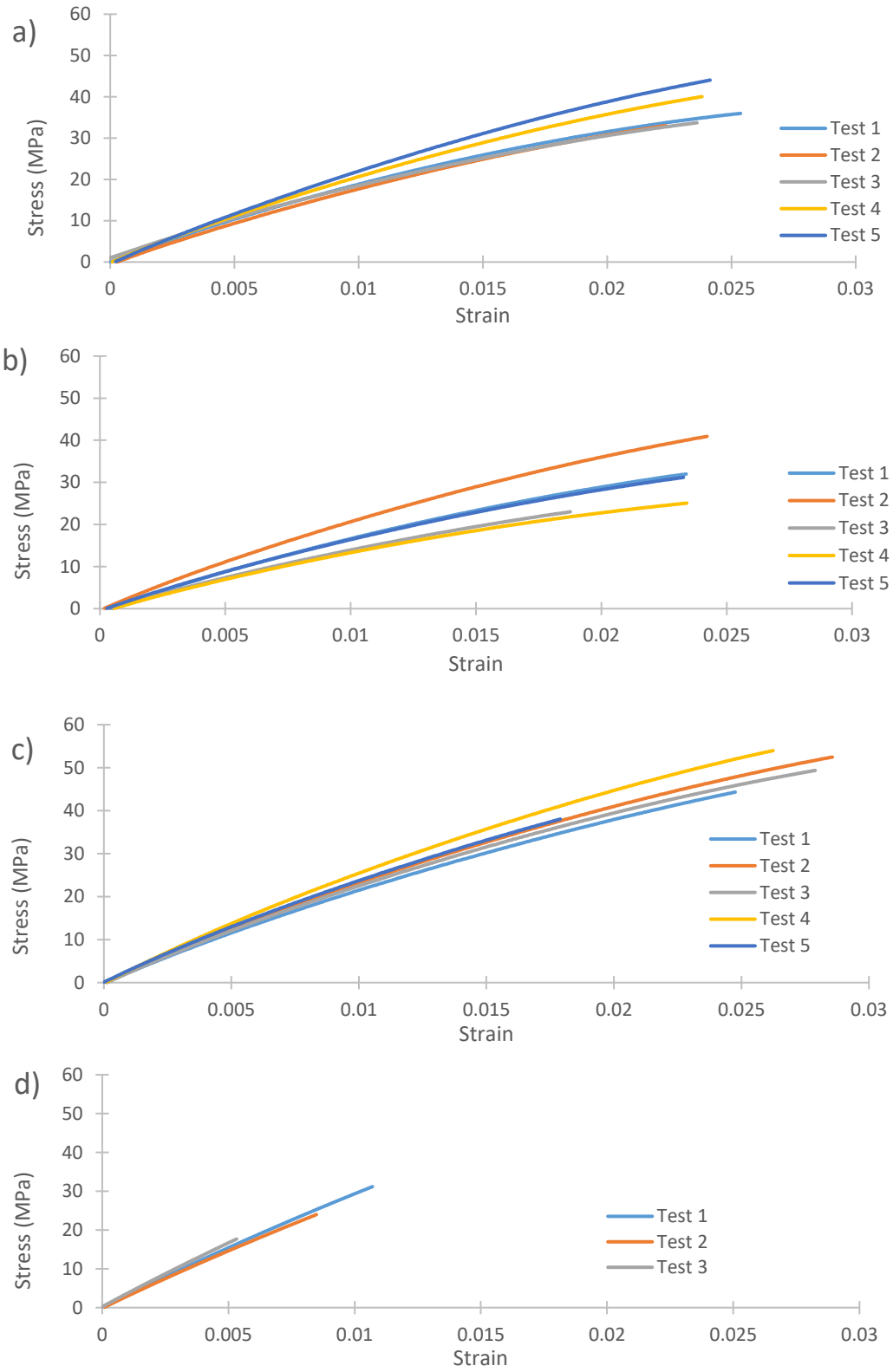

Figure 5.17: Stress-strain graphs (ASTM D638) for the four NRC filaments printed with a 0.4 mm nozzle and with a nozzle temperature of 400°C: a) 20 wt.% rCF, b) 15 wt.% rCF - 5 wt.% TB, c) 10 wt.% rCF – 10 wt.% TB and d) 20 wt.% TB.

The ultimate stress at break also presented important variations and in particular test 3 and test 4 presented lower stress values compared to the other 3 specimens. Figure 5.17 c) shows the graph for the formulations with 10 wt.% rCF – 10 wt.% TB, which presented a very consistent elastic regime before the strain of 0.01 and the early failure of test 5. In addition, three tests presented values for ultimate stress at break above 40 MPa (with a strain above 0.025), which seem to be the best results. Finally, Figure 5.17 d) represents the graph for the blend with 20 wt.% TB which shows early failure for the three tested specimens with a low elongation at break before 0.012, however the three specimens presented fairly the same slope in the elastic regime.

From the stress-strain curves, the Young's modulus and the UTS data was obtained. Figure 5.18 shows the Young's modulus for the 4 tested composites. The highest Young's modulus was obtained for the blend with the 20 wt.% TB (3.3 GPa with a standard deviation of 0.16 GPa) followed by the 10 wt.% rCF – 10 wt.% TB formulation (2.7 GPa with a standard deviation of 0.17 GPa), which show small variations. The lowest Young's modulus was obtained for the blend with 15 wt.% rCF – 5 wt.% TB (2.0 GPa with a standard deviation of 0.31 GPa). These are unexpected results, since the blend with the highest wt.% of rCF should be the one with the best tensile results. However, do to a lack of improvement of the 3D printing parameters (nozzle temperature, extrusion multiplier, etc.) the highest results were obtained for the blend with the largest content of TB. Figure 5.19 shows the values obtained for the UTS. The highest UTS was obtained for the reinforcement with 10 wt.% rCF – 10 wt.% TB (47 MPa with a standard deviation of 6.5 MPa), which seems to be the best results so far of the NRC filament. The lowest UTS was obtained for the blend with 20 wt.% TB (23 MPa with a standard deviation of 6.8 MPa) which seems to be in accordance with the composition of the reinforcements.

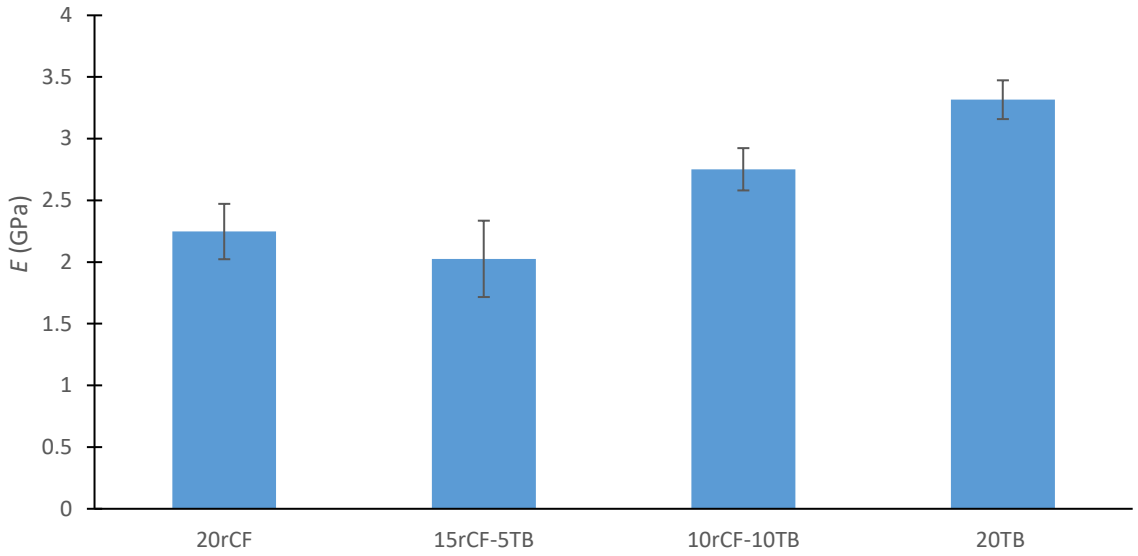

Figure 5.18: Young's modulus results for the samples 3D printed with the four formulations of NRC filaments: 20 wt.% rCF, 15 wt.% rCF – 5 wt.% TB, 10 wt.% rCF – 10 wt.% TB and 20 wt.% TB.

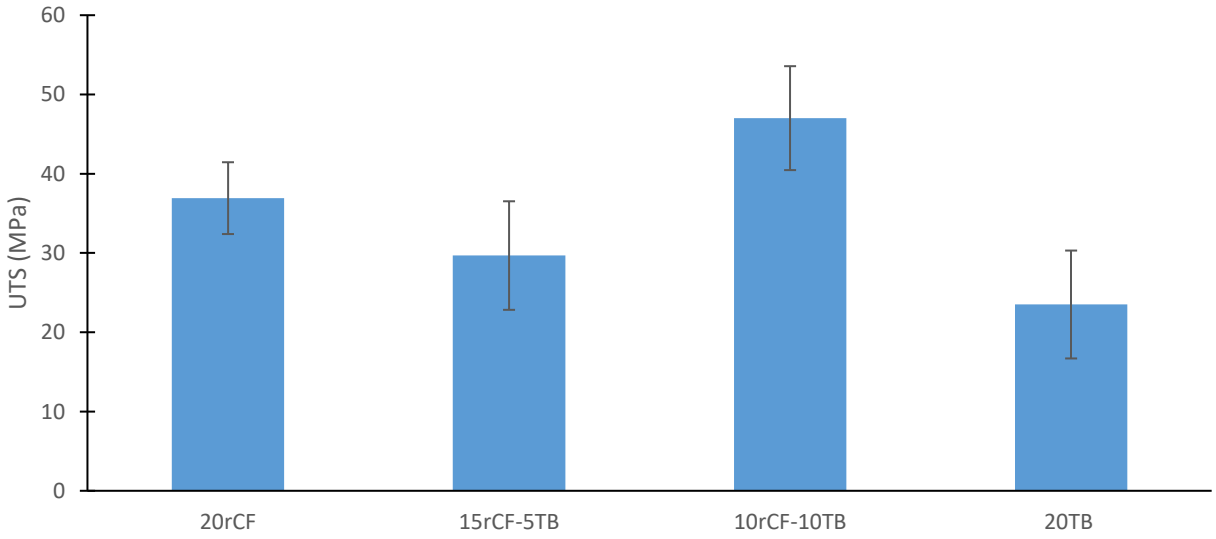

Figure 5.19: UTS results for the samples 3D printed with the four formulations of NRC filaments: 20 wt.% rCF, 15 wt.% rCF – 5 wt.% TB, 10 wt.% rCF – 10 wt.% TB and 20 wt.% TB.

Microstructure characterization of specimens printed with NRC filaments

Figure 5.20 shows the micro-CT images for the internal cross section of the central part of the neck of the dogbones before the tensile tests. Figure 5.20 a) corresponds to the dogbone made of 20 wt.% of rCF and shows a smoother top surface, however important under extrusion is also observed. Figure 5.20 b) shows the image for 20 wt.% TB with a very rough top surface, under extrusion and large defects on the sides of the samples. In both images, the two external 3D printed layers can be clearly identified in the sides of the samples. The images show two different scales of porosity, the first one is interlayer porosity and was appreciated between the printed filaments at 45/-45° raster angle. Interlayer porosity also appeared between the external layers and the internal printed filaments where holes with a maximum length of ~400 µm appeared for the dogbones made of 20 wt.% TB. The second scale of porosity is intralayer porosity and appeared in each of the printed layers (for all the samples printed with NRC filaments) as black dots smaller than 100 µm. The total porosity for the samples printed with NRC filaments was ~16 %.

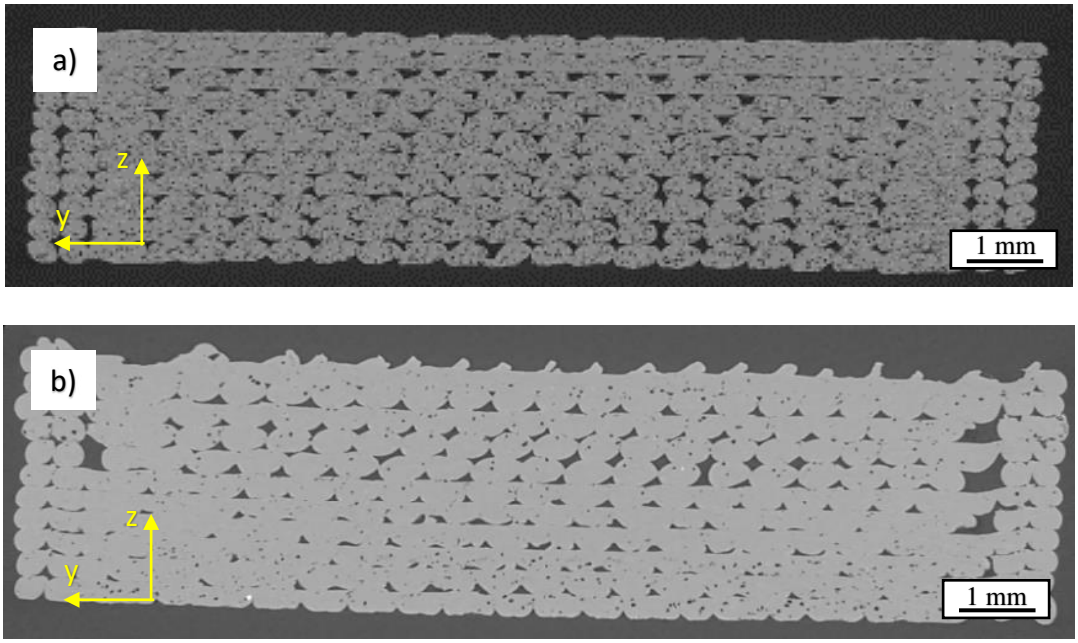

Figure 5.20: Micro-CT images showing the internal porosity of specimens printed with NRC filaments before testing with a) 20 wt.% rCF and b) 20 wt.% TB.

SEM analysis were performed on the central region of the dogbones for the top and fractured surfaces of each formulation, after the tensile tests. Figure 5.21 shows the SEM images obtained for the tested samples. The SEM images from the top surface are Figure 5.21 a), c), e) and g) for 20 wt.% rCF, 15 wt.% rCF - 5 wt.% TB, 10 wt.% rCF - 10 wt.% TB and 20 wt.% TB, respectively. The top surface images also show the porosities with maximum dimension of 400 µm in the interlayer between the two external layers and the internal ones printed at -45/45°. These porosities are more visible in the top surface of the samples printed with 10 wt.% rCF - 10 wt.% TB and 20 wt.% TB. For all the composites, porosities can be observed on the fractured surfaces as shown in Figure 5.21 b), d), f) and h), respectively, for the different formulations, respectively. Porosities appear in the interlayer between the two external layers and the internal layers with 45/-45°. Furthermore, the porosities seem to be more predominant in the right part of the fracture images, where the two external printed layers are located.

In addition, the images of the fractured surfaces with higher wt.% of rCF (20 wt.% and 15 wt.%), Figure 5.21 b) and d), show intralayers porosities smaller than 100 µm. The intralayers porosities appear in each of the printed deposited layers and were not related to the printing process but certainly to the printing material itself.

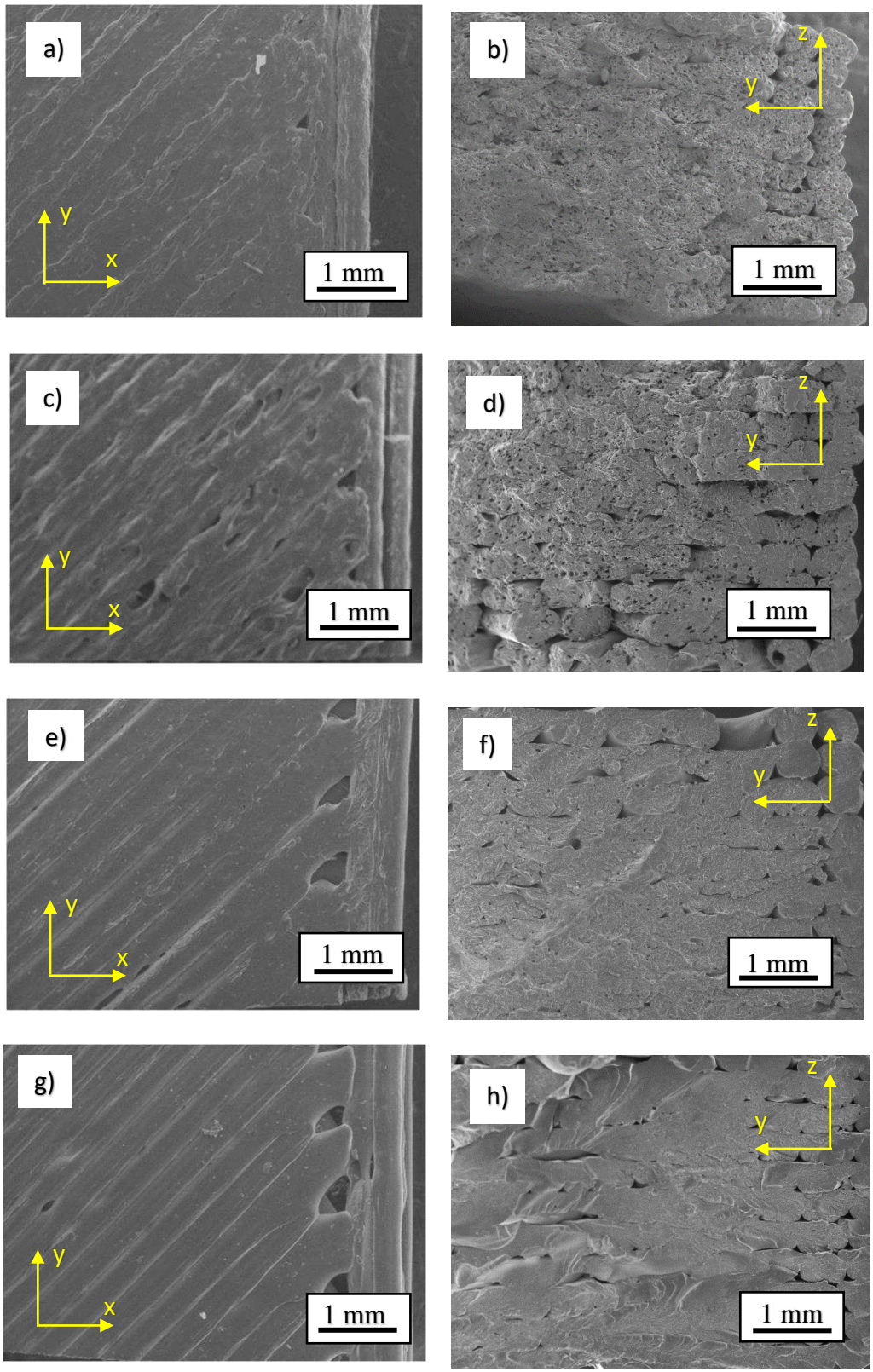

Figure 5.21: SEM images done after tensile test for the 4 different formulations of NRC filaments for the top and fracture regions respectively: a) and b) 20 wt.% rCF, c) and d) 15 wt.% rCF - 5 wt.% TB, e) and f) 10 wt.% rCF - 10 wt.% TB, g) and h) 20 wt.% TB.

Figure 5.22 is the SEM image of the cross section of a printing filament (diameter: 1.75 mm) with 20 wt.% rCF that shows by the yellow circles one of the possible origin of the intralayer porosity (<100 μm) of the printed samples. The other possible origin is the degradation of the material that creates small voids. The reduction of the intralayer porosities for the printed samples with 20 wt.% TB and 10 wt.% rCF - 10 wt.% TB could be the explanation of why the obtained Young's modulus is higher for these blends.

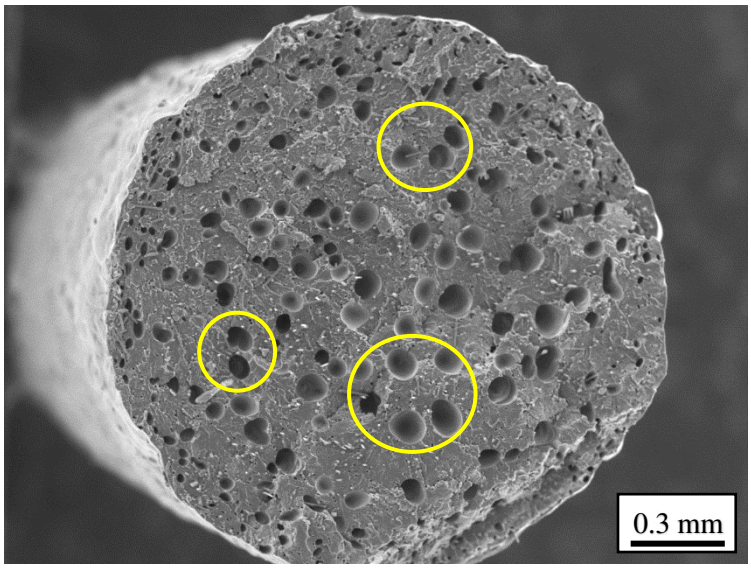

Figure 5.22: SEM image of the cross section of an NRC filament made of ULTEM 1040 with 20 wt.% rCF where porosities smaller than 100 μm are observed (yellow circles).

5.2.3 Discussion of results obtained with developed filaments

The printing tests with LM2 filaments demonstrated the feasibility to print custom-made filaments with different percentages of CF reinforcement, with a maximum of 40 wt.%. The use of a 0.4 mm nozzle was optimal to print a CF percentage of reinforcement up to 20 wt.% with the different ULTEM grades. Above that percentage, a 0.6 nozzle was required to avoid clogging the nozzle. ULTEM 1040 was the grade that allowed the maximum percentage of reinforcements to be printed, up to 40 wt.% of CF reinforcements.

3D printing of the NRC filaments allowed mechanical testing with four different formulations and study of the samples with micro-CT and SEM. One of the printing parameters that may have an important difference is the addition of the two external layers printed around the samples to avoid edges with the printed layers that could facilitate the initiation of fracture during mechanical testing. In addition, a good qualitative measurement of the printing quality of the samples is the location of the fracture during the tensile tests. For all the formulations, there was at least one printed sample with the fracture in the middle of the dogbone's neck. In the case of the 20 wt.% TB, all the samples tested broke in the middle of the neck which could be an indicator of a good internal structure since the thinnest region of the sample is the middle one. Therefore, it could be related to the highest Young's modulus (3.3 GPa) achieved for this formulation. However, it could also mean that the samples were fragile and which may explain low UTS (23.5 MPa) for 20 wt.% TB. The formulation with 10 wt.% rCF - 10 wt.% TB obtained the best results and the highest UTS with a value of 47 MPa and a consistent elastic regime in all the tested samples. The mechanical results showed an improvement in the Young's modulus (34.4 %) and UTS (9.8 %) compared to the Com. Reinf. filaments with 10 wt.% of CF. The micro-CT analysis showed two types of porosities. The first one, inter-layers porosity can be explained by the performance of the FFF process and the selection of the printing parameters (nozzle temperature and extrusion multiplier). The second type of porosity, the intra-layers one, was probably due to the innate nature of the material. The high degree of porosity of ~16 % for the different formulations would be possibly an explanation for the relatively low mechanical results obtained.

CHAPTER 6 CONCLUSIONS

6.1 Summary of works

Commercial and developed 3D printing filaments were printed with two different FFF 3D printers. The initial use of commercial HTPs and HTRPs materials to test the influence of some parameters served as further training for, later on, printing custom-made HTPs and HTRPs. The use of AON3D's open-source technology together with the slicer Simplify3D allowed great freedom in the selection of printing parameters and printing materials.

Different printing speeds were tested for the Com. Pure filaments (commercial ULTEM 1010) to study the reduction on the printing time. However, the increase in the printing speed from 20 mm/s to 60 mm/s produced a clear decrease in the mechanical properties such as the Young's modulus that exhibited a 24 % reduction between the two speeds studied. The use of high temperature developed filaments for 3D printing demonstrated the feasibility of using non-commercial materials with reduced printing costs that even improves the mechanical properties. During the different stages of the project, mechanical properties as well as defects on the surface or in the internal structure of the printed parts were analyzed with different techniques such as SEM and micro-CT, showing the interlayer porosity related to the printing process and the intralayer porosity originated from the printing material itself. The porosity obtained was ~16 % for the samples printed with the NRC filaments.

In conclusion, this project studied the printing process for HTPs and HTRPs together with open-source FFF technology and contributed on the process for 3D printing of structural parts for aerospace applications such as aircraft interiors or small satellites with new developed filaments.

Moreover, the scientific developments performed in this project were done in collaboration and with the help of the scientifics from National Research Council of Canada and the continuation of the 3DREAM project will further benefit the 13 industrial partners participating in this industrial R&D group with an optimized 3D printing technology using advanced composites.

6.2 Recommendations for future research

- Further optimize the printing parameters of the developed filaments to improve the mechanical properties of the printed parts and to reduce the two types of porosities (interlayer and intralayer) shown in the SEM and micro-CT images. In addition to the tensile properties, other types of mechanical tests like bending and impact should be done with sandwich panels to study the feasibility of these materials for future applications.
- Optimize the printing parameters for the developed filaments using Design of Experiments (DoE). Some of the printing parameters that could be investigated are: layer height, nozzle temperature, bed temperature, chamber temperature or extrusion multiplier. In addition, consider the elevated T_g of PEI (217°C) when selecting the chamber temperature to improve the adhesion between printed layers.
- Study the use of high-flow extruders that may be able to print large sandwich panels with an optimal accuracy in a reduced amount of time for large scale and industrial applications.
- Perform non-planar 3D printing with the developed filaments to increase the achieved mechanical properties and improve the printing process adapting it to the shape of the built part.
- Study the recyclability of PEI blends to reuse 3D printed material to produce recycled filaments ready to be 3D printed another time and to study the mechanical properties of the samples printed with these filaments.
- Develop in-situ monitoring methods for the 3D printing process seems to be an important research field to work in the following years to assure quality and repeatability of the printed parts in a large scale production. OCT represents a possible option to perform in-situ monitoring but there is still a lot of research work to be done to prove the validity of this technique with different materials and printed parts.

REFERENCES

[1] K.W. Chun, H. Kim, K. Lee, A Study on Research Trends of Technologies for Industry 4.0; 3D Printing, Artificial Intelligence, Big Data, Cloud Computing, and Internet of Things, in: J.J. Park, V. Loia, K.-K.R. Choo, G. Yi (Eds.), Adv. Multimed. Ubiquitous Eng., Springer Singapore, Singapore, 2019: pp. 397–403. https://doi.org/10.1007/978-981-13-1328-8_51.

[2] K. Schwab, The Fourth Industrial Revolution, (n.d.) 172.

[3] M.A. Kaleem, M. Khan, Significance of Additive Manufacturingfor Industry 4.0With Introduction of Artificial Intelligence in Additive Manufacturing Regimes, in: 2020 17th Int. Bhurban Conf. Appl. Sci. Technol. IBCAST, IEEE, Islamabad, Pakistan, 2020: pp. 152–156. https://doi.org/10.1109/IBCAST47879.2020.9044574.

[4] T.D. Ngo, A. Kashani, G. Imbalzano, K.T.Q. Nguyen, D. Hui, Additive manufacturing (3D printing): A review of materials, methods, applications and challenges, Compos. Part B Eng. 143 (2018) 172–196. https://doi.org/10.1016/j.compositesb.2018.02.012.

[5] A. Yadav, P. Rohru, A. Babbar, R. Kumar, N. Ranjan, J.S. Chohan, R. Kumar, M. Gupta, Fused filament fabrication: A state-of-the-art review of the technology, materials, properties and defects, Int. J. Interact. Des. Manuf. IJIDeM. (2022). https://doi.org/10.1007/s12008-022-01026-5.

[6] W. Gao, Y. Zhang, D. Ramanujan, K. Ramani, Y. Chen, C.B. Williams, C.C.L. Wang, Y.C. Shin, S. Zhang, P.D. Zavattieri, The status, challenges, and future of additive manufacturing in engineering, Comput.-Aided Des. 69 (2015) 65–89. https://doi.org/10.1016/j.cad.2015.04.001.

[7] M. Khalid, Q. Peng, Investigation of Printing Parameters of Additive Manufacturing Process for Sustainability Using Design of Experiments, J. Mech. Des. 143 (2021) 032001. https://doi.org/10.1115/1.4049521.

[8] J. Saroia, Y. Wang, Q. Wei, M. Lei, X. Li, Y. Guo, K. Zhang, A review on 3D printed matrix polymer composites: its potential and future challenges, Int. J. Adv. Manuf. Technol. 106 (2020) 1695–1721. https://doi.org/10.1007/s00170-019-04534-z.

[9] M. Pérez-Pérez, E. Gómez, M. Sebastián, Delphi Prospection on Additive Manufacturing in 2030: Implications for Education and Employment in Spain, Materials. 11 (2018) 1500. https://doi.org/10.3390/ma1109150.

[10] J. Andrzejewski, L. Marciniak-Podsadna, Development of Thermal Resistant FDM Printed Blends. The Preparation of GPET/PC Blends and Evaluation of Material Performance, Materials. 13 (2020) 2057. https://doi.org/10.3390/ma13092057.

[11] PEEK 3D Printing Filament from 3DXTECH | Made in the USA, (n.d.). https://www.3dxtech.com/product/thermax-peek/ (accessed October 14, 2021).

[12] S. Ding, B. Zou, P. Wang, H. Ding, Effects of nozzle temperature and building orientation on mechanical properties and microstructure of PEEK and PEI printed by 3D-FDM, Polym. Test. 78 (2019) 105948. https://doi.org/10.1016/j.polymertesting.2019.105948.

[13] H.F. Mark, Encyclopedia of Polymer Science and Technology, Concise, John Wiley & Sons, 2013.

[14] K.C. Chuang, J.E. Grady, R.D. Draper, E.-S.E. Shin, C. Patterson, T.D. Santelle, ADDITIVE MANUFACTURING AND CHARACTERIZATION OF ULTEM POLYMERS AND COMPOSITES, (n.d.) 15. https://ntrs.nasa.gov/citations/20160001352.

[15] Ultem 1010 3D Printing Filament | High Performance Materials | Made in the USA, (n.d.). https://www.3dxtech.com/product/thermax-pei-using-ultem-1010/ (accessed October 14, 2022).

[16] Ultem 9085 3D Printing Filament | High Performance Materials | Made in the USA, (n.d.). https://www.3dxtech.com/product/thermax-pei-using-ultem-9085/ (accessed October 14, 2022).

[17] An investigation into 3D printing of fibre reinforced thermoplastic composites | Elsevier Enhanced Reader, (n.d.). https://doi.org/10.1016/j.addma.2018.04.039.

[18] A process-structure-performance modeling for thermoplastic polymers via material extrusion additive manufacturing | Elsevier Enhanced Reader, (n.d.). https://doi.org/10.1016/j.addma.2021.101857.
[19] S. Jiang, G. Liao, D. Xu, F. Liu, W. Li, Y. Cheng, Z. Li, G. Xu, Mechanical properties analysis of polyetherimide parts fabricated by fused deposition modeling, High Perform. Polym. 31 (2019) 97–106. https://doi.org/10.1177/0954008317752822.
[20] R.J. Zaldivar, D.B. Witkin, T. McLouth, D.N. Patel, K. Schmitt, J.P. Nokes, Influence of processing and orientation print effects on the mechanical and thermal behavior of 3D-Printed ULTEM® 9085 Material, Addit. Manuf. 13 (2017) 71–80. https://doi.org/10.1016/j.addma.2016.11.007.
[21] M. Fischer, V. Schöppner, Fatigue Behavior of FDM Parts Manufactured with Ultem 9085, JOM. 69 (2017) 563–568. https://doi.org/10.1007/s11837-016-2197-2.
[22] A. Arivazhagan, A. Saleem, S.H. Masood, M. Nikzad, K.A. Jagadeesh, STUDY OF DYNAMIC MECHANICAL PROPERTIES OF FUSED DEPOSITION MODELLING PROCESSED ULTEM MATERIAL, Am. J. Eng. Appl. Sci. 7 (2014) 307–315. https://doi.org/10.3844/ajeassp.2014.307.315.
[23] Stratasys F900 3D Printer In-Depth Review, Pick 3D Print. (2021). https://pick3dprinter.com/stratasys-f900-review/ (accessed October 14, 2021).
[24] AON3D launches AON-M2 2020 3D printer - Technical specifications and pricing, 3D Print. Ind. (2020). https://3dprintingindustry.com/news/aon3d-launches-aon-m2-2020-3d-printer-technical-specifications-and-pricing-168378/ (accessed October 14, 2021).
[25] Tungsten Carbide Nozzle: Ultimate durability and performance nozzle, DYZE Des. (n.d.). https://dyzedesign.com/tungsten-carbide-nozzle/ (accessed October 10, 2021).
[26] D. Brzeski, I.L. Hia, J.-F. Chauvette, R.D. Farahani, N. Piccirelli, A. Ross, D. Therriault, Design of thermoset composites for high-speed additive manufacturing of lightweight sound absorbing micro-scaffolds, Addit. Manuf. 47 (2021) 102245. https://doi.org/10.1016/j.addma.2021.102245.
[27] J.-F. Chauvette, D. Brzeski, I.L. Hia, R.D. Farahani, N. Piccirelli, D. Therriault, High-speed multinozzle additive manufacturing and extrusion modeling of large-scale microscaffold networks, Addit. Manuf. 47 (2021) 102294. https://doi.org/10.1016/j.addma.2021.102294.
[28] J. Go, S.N. Schiffres, A.G. Stevens, A.J. Hart, Rate limits of additive manufacturing by fused filament fabrication and guidelines for high-throughput system design, Addit. Manuf. 16 (2017) 1–11. https://doi.org/10.1016/j.addma.2017.03.007.
[29] S. Wang, L. Capoen, D.R. D'hooge, L. Cardon, Can the melt flow index be used to predict the success of fused deposition modelling of commercial poly(lactic acid) filaments into 3D printed materials?, Plast. Rubber Compos. 47 (2018) 9–16. https://doi.org/10.1080/14658011.2017.1397308.
[30] Typhoon™ Fast Print & High Flow Rate 3D Printer Extruder, DYZE Des. (n.d.). https://dyzedesign.com/typhoon-extruder/ (accessed December 18, 2022).
[31] Pulsar™ Pellet Extruder: Industrial High Flow Extruder, DYZE Des. (n.d.). https://dyzedesign.com/pulsar-pellet-extruder/ (accessed October 10, 2021).
[32] P. Wang, B. Zou, H. Xiao, S. Ding, C. Huang, Effects of printing parameters of fused deposition modeling on mechanical properties, surface quality, and microstructure of PEEK, J. Mater. Process. Technol. 271 (2019) 62–74. https://doi.org/10.1016/j.jmatprotec.2019.03.016.
[33] P. Wang, B. Zou, S. Ding, L. Li, C. Huang, Effects of FDM-3D printing parameters on mechanical properties and microstructure of CF/PEEK and GF/PEEK, Chin. J. Aeronaut. 34 (2021) 236–246. https://doi.org/10.1016/j.cja.2020.05.040.
[34] BAAM - Big Area Additive Manufacturing, Cincinnati Inc. (n.d.). https://www.e-ci.com/baam (accessed October 14, 2021).
[35] C. Ajinjeru, V. Kishore, J. Lindahl, Z. Sudbury, A.A. Hassen, B. Post, L. Love, V. Kunc, C. Duty, The influence of dynamic rheological properties on carbon fiber-reinforced polyetherimide for large-

scale extrusion-based additive manufacturing, Int. J. Adv. Manuf. Technol. 99 (2018) 411–418. https://doi.org/10.1007/s00170-018-2510-z.
[36] C.E. Duty, V. Kunc, B. Compton, B. Post, D. Erdman, R. Smith, R. Lind, P. Lloyd, L. Love, Structure and mechanical behavior of Big Area Additive Manufacturing (BAAM) materials, Rapid Prototyp. J. 23 (2017) 181–189. https://doi.org/10.1108/RPJ-12-2015-0183.
[37] P. Chesser, B. Post, A. Roschli, C. Carnal, R. Lind, M. Borish, L. Love, Extrusion control for high quality printing on Big Area Additive Manufacturing (BAAM) systems, Addit. Manuf. 28 (2019) 445–455. https://doi.org/10.1016/j.addma.2019.05.020.
[38] T. D'Amico, A.M. Peterson, Bead parameterization of desktop and room-scale material extrusion additive manufacturing: How print speed and thermal properties affect heat transfer, Addit. Manuf. 34 (2020) 101239. https://doi.org/10.1016/j.addma.2020.101239.
[39] B. Heller, D.E. Smith, D. Jack, Effect of Extrudate Swell , Nozzle Shape , and Convergence Zone on Fiber Orientation in Fused Deposition Modeling Nozzle Flow, (2015). https://www.semanticscholar.org/paper/Effect-of-Extrudate-Swell-%2C-Nozzle-Shape-%2C-and-Zone-Heller-Smith/7dabaac6117cc36d7f0bcb5c614a51a24b2ad848 (accessed October 14, 2021).
[40] M.E.A. Papon, A. Haque, M.A.R. Sharif, Effect of Nozzle Geometry on Melt Flow Simulation and Structural Property of Thermoplastic Nanocomposites in Fused Deposition Modeling, in: Am. Soc. Compos. 2017, DEStech Publications, Inc., 2017. https://doi.org/10.12783/asc2017/15339.
[41] Die swell, Wikipedia. (2021). https://en.wikipedia.org/w/index.php?title=Die_swell&oldid=1034208279 (accessed October 14, 2021).
[42] W. Lao, D.Y.W. Tay, D. Quirin, M.J. Tan, The effect of nozzle shapes on the compactness and strength of structures printed by additive manufacturing of concrete, in: 2018. https://doi.org/10.25341/D4V01X.
[43] A. Matschinski, P. Ziegler, T. Abstreiter, T. Wolf, K. Drechsler, Fiber Formation of Printed Carbon Fiber/Poly (Ether Ether Ketone) with Different Nozzle Shapes, Polym. Int. 70 (2021) 1109–1117. https://doi.org/10.1002/pi.6196.
[44] B. Graver, CO2 emissions from commercial aviation, 2018, (2018) 13.
[45] M. Pant, P. Pidge, L. Nagdeve, H. Kumar, A Review of Additive Manufacturing in Aerospace Application, Rev. Compos. Matér. Avancés. 31 (2021) 109–115. https://doi.org/10.18280/rcma.310206.
[46] A. Ampatzoglou, S. Tsantzalis, D. Mazarakos, V. Kostopoulos, 3D printed frame for CubeSat applications for low-Earth orbit mission, Int. J. Comput. Aided Eng. Technol. 9 (2017) 434. https://doi.org/10.1504/IJCAET.2017.086923.
[47] A. Kafi, H. Wu, J. Langston, O. Atak, H. Kim, S. Kim, W.P. Fahy, R. Reber, J. Misasi, S. Bateman, J.H. Koo, Evaluation of additively manufactured ultraperformance polymers to use as thermal protection systems for spacecraft, J. Appl. Polym. Sci. 137 (2020) 49117. https://doi.org/10.1002/app.49117.
[48] L. Griffiths, Additive manufacturing in the aircraft cabin, TCT Mag. (2020). https://www.tctmagazine.com/api/content/8d059cb6-e142-11ea-b724-1244d5f7c7c6/ (accessed December 18, 2022).
[49] A. Bagsik, S. Josupeit, V. Schoeppner, E. Klemp, Mechanical analysis of lightweight constructions manufactured with fused deposition modeling, in: Nuremberg, Germany, 2014: pp. 696–701. https://doi.org/10.1063/1.4873874.
[50] S. Antony, A. Cherouat, G. Montay, Fabrication and Characterization of Hemp Fibre Based 3D Printed Honeycomb Sandwich Structure by FDM Process, Appl. Compos. Mater. 27 (2020) 935–953. https://doi.org/10.1007/s10443-020-09837-z.

[51] S. Gohar, G. Hussain, A. Ali, H. Ahmad, Mechanical performance of honeycomb sandwich structures built by FDM printing technique, J. Thermoplast. Compos. Mater. (2021) 089270572199789. https://doi.org/10.1177/0892705721997892.
[52] W. Zhai, B. Hu, M. Li, J. Jiang, M. Zhou, Dimensional Accuracy Control and Compressive Property of Microcellular Polyetherimide Honeycomb Foams Manufactured by an In Situ Foaming Fused Deposition Modeling Technology, Adv. Eng. Mater. 23 (2021) 2001449. https://doi.org/10.1002/adem.202001449.
[53] M. Hirsch, R. Patel, W. Li, G. Guan, R.K. Leach, S.D. Sharples, A.T. Clare, Assessing the capability of in-situ nondestructive analysis during layer based additive manufacture, Addit. Manuf. 13 (2017) 135–142. https://doi.org/10.1016/j.addma.2016.10.004.
[54] I. Blanco, G. Cicala, G. Ognibene, M. Rapisarda, A. Recca, Thermal properties of polyetherimide/polycarbonate blends for advanced applications, Polym. Degrad. Stab. 154 (2018) 234–238. https://doi.org/10.1016/j.polymdegradstab.2018.06.011.
[55] S. Sommacal, A. Matschinski, K. Drechsler, P. Compston, Characterisation of void and fiber distribution in 3D printed carbon-fiber/PEEK using X-ray computed tomography, Compos. Part Appl. Sci. Manuf. 149 (2021) 106487. https://doi.org/10.1016/j.compositesa.2021.106487.
[56] B. Gapinski, M. Wieczorowski, M. Grzelka, P. Arroyo Alonso, A. Bermudez Tome, The application of micro computed tomography to assess quality of parts manufactured by means of rapid prototyping, Polimery. 62 (2017) 53–59. https://doi.org/10.14314/polimery.2017.053.
[57] T.T. Mekonnen, A. Kourmatzis, S. Cheng, Wavelength-encoded multi-channel spectral-domain optical coherence tomography (SD-OCT) for spatiotemporally resolved imaging, Meas. Sci. Technol. (Accepted) (2020). https://doi.org/10.1088/1361-6501/ab85d6.
[58] W. Drexler, J.G. Fujimoto, Optical Coherence Tomography: Technology and Applications, Springer Berlin Heidelberg, 2008. https://books.google.ca/books?id=q3q1RI-VdPYC.
[59] Z. Hu, B. Hao, W. Liu, B. Hong, J. Li, Test target for characterizing 3D resolution of optical coherence tomography, in: J. Czarske, S. Zhang, D. Sampson, W. Wang, Y. Liao (Eds.), Beijing, China, 2014: p. 92971S. https://doi.org/10.1117/12.2073062.
[60] J. Lee, S.A. Saleah, B. Jeon, R.E. Wijesinghe, D.-E. Lee, M. Jeon, J. Kim, Assessment of the Inner Surface Roughness of 3D Printed Dental Crowns via Optical Coherence Tomography Using a Roughness Quantification Algorithm, IEEE Access. 8 (2020) 133854–133864. https://doi.org/10.1109/ACCESS.2020.3011136.
[61] L.R. De Pretto, M.M. Amaral, A.Z. de Freitas, M.P. Raele, Nondestructive evaluation of fused filament fabrication 3D printed structures using optical coherence tomography, Rapid Prototyp. J. 26 (2020) 1853–1860. https://doi.org/10.1108/RPJ-12-2019-0314.
[62] 3DXTech, Ultem 1010 Technical Data Sheet, (n.d.). https://www.3dxtech.com/wp-content/uploads/2021/03/PEI_1010-TDS-v04.pdf (accessed October 8, 2021).
[63] 3DXTech, Carbon Fiber Reinforced Ultem 1010 Technical Data Sheet, (n.d.). https://www.3dxtech.com/wp-content/uploads/2021/03/PEI_CF-TDS-v03.pdf (accessed October 8, 2021).

APPENDIX A: STRESS-STRAIN CURVES FOR COM. PURE AND COM. REINF. FILAMENTS

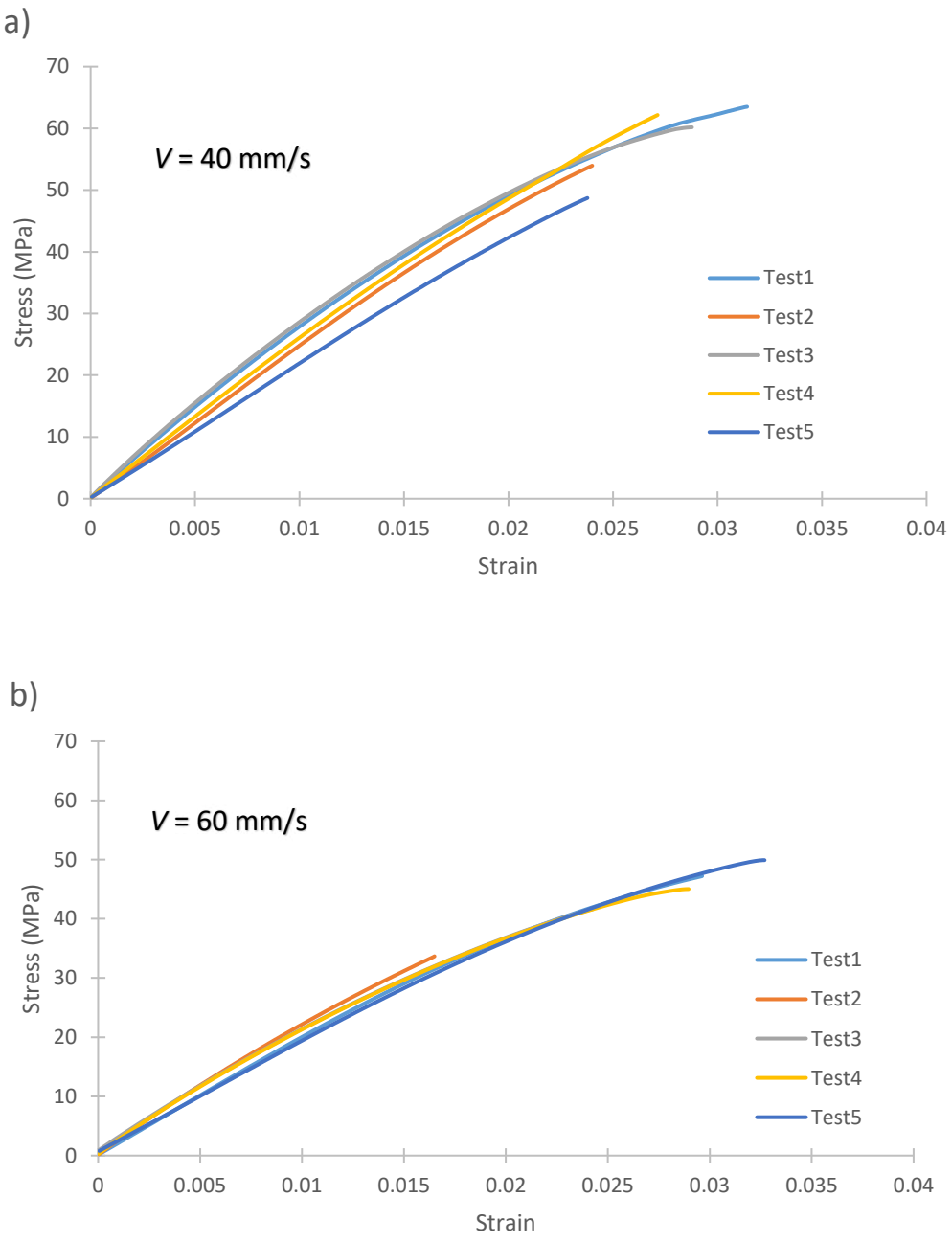

Figure A.1: Stress-strain graphs for ASTM D638 specimens printed with Com. Pure filaments with a 0.4 mm nozzle and with a nozzle temperature of 370°C at 2 printing speeds : a) 40 mm/s and b) 60 mm/s.

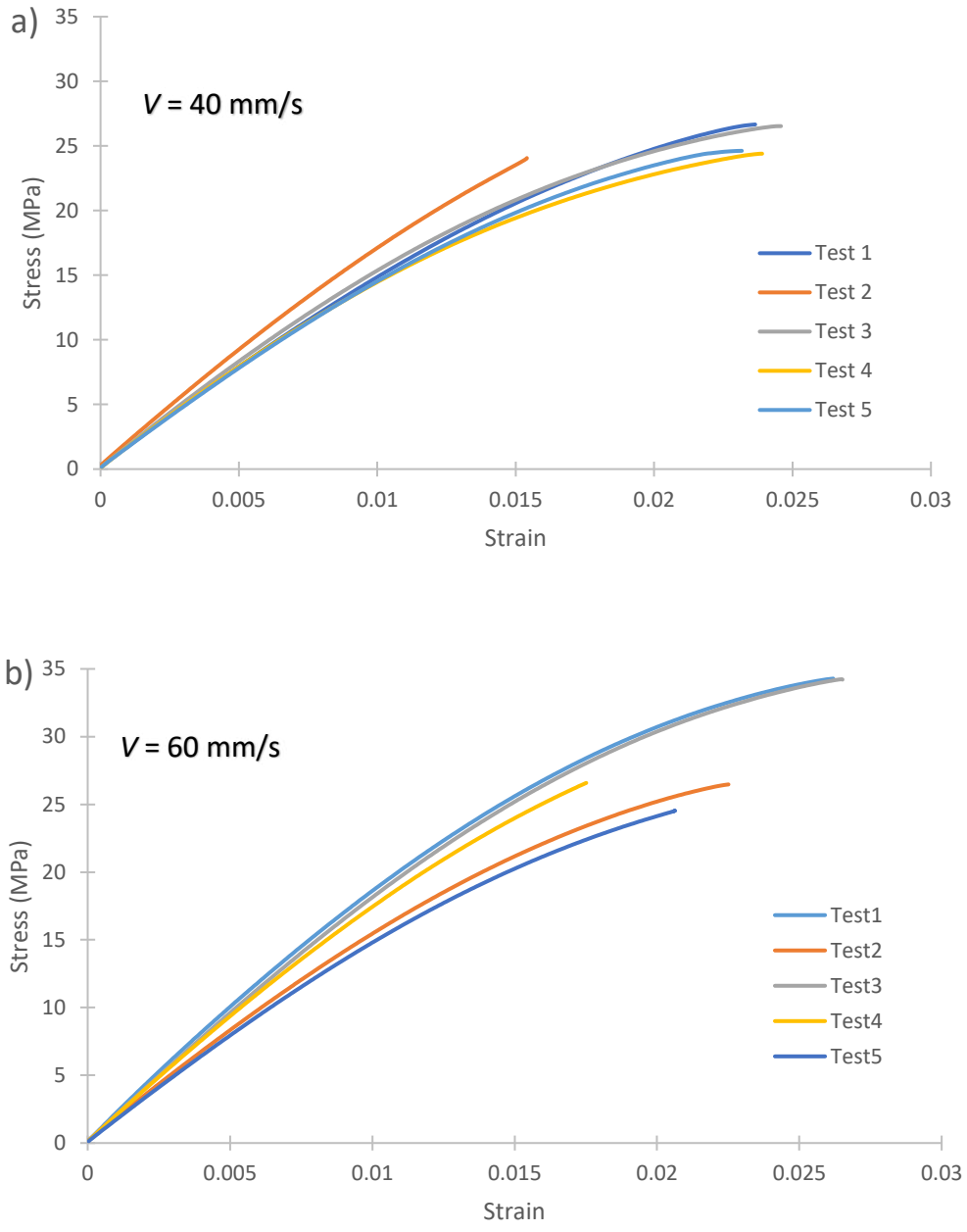

Figure A.2: Stress-strain graphs for ASTM D638 specimens printed with Com. Reinf. filaments with a 0.4 mm nozzle and with a nozzle temperature of 400°C at 2 printing speeds: a) 40 mm/s and b) 60 mm/s.